Universitat d'Alacant
Universidad de Alicante

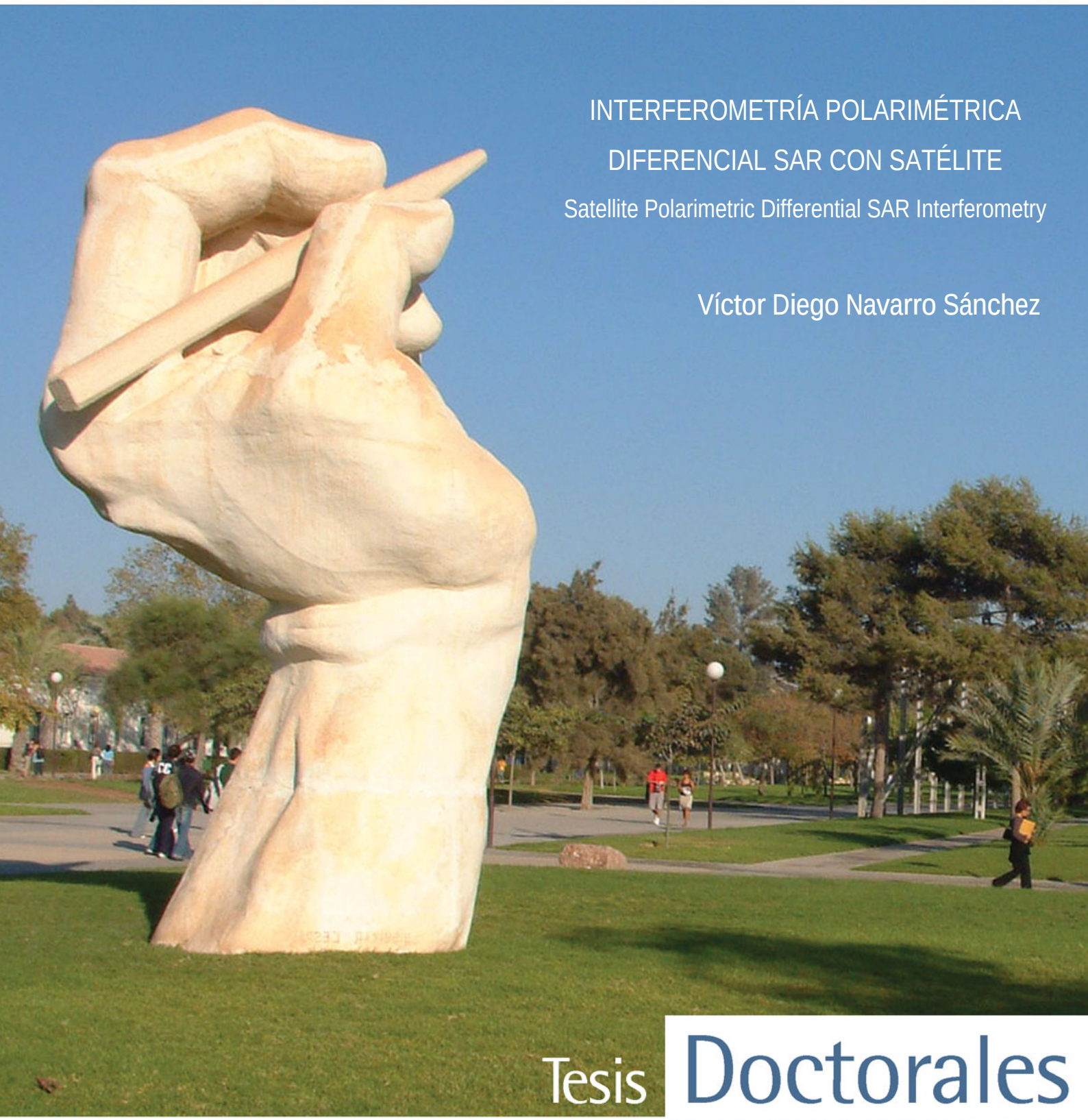

INTERFEROMETRÍA POLARIMÉTRICA DIFERENCIAL SAR CON SATÉLITE

Satellite Polarimetric Differential SAR Interferometry

Víctor Diego Navarro Sánchez

Tesis Doctorales

www.eltallerdigital.com

UNIVERSIDAD de ALICANTE

Universitat d'Alacant
Universidad de Alicante

INTERFEROMETRÍA POLARIMÉTRICA DIFERENCIAL SAR CON SATÉLITE

Satellite Polarimetric Differential SAR Interferometry

Víctor Diego Navarro Sánchez

Directores: Dr. Juan Manuel López Sánchez y Dr. Josep Arnal García

A Sofía

Acknowledgements

This thesis is the result of the research work carried out during the last four years, supported by the Spanish Ministerio de Educación y Competitividad (MINECO) and European Union FEDER funds under projects TEC2008-06764-C02-02, TEC2011-28201-C02-02 and the associated predoctoral grant BES-2009-017479, as well as the Generalitat Valenciana under ACOMP07-087 funds.

This work would not have been possible without the invaluable satellite data, so I would like to acknowledge the data suppliers. The TerraSAR-X images have been provided by the German Aerospace Center (DLR) in the framework of project GEO0389 of the TerraSAR-X scientific program. RADARSAT-2 Data and Products ©MacDonald, Dettwiler and Associates Ltd. (2010–12) – All Rights Reserved. RADARSAT is an official trademark of the Canadian Space Agency. I would like to thank Prof. Jordi Mallorquí (Universitat Politécnica de Catalunya) for providing access to the RADARSAT-2 data, which were provided by MDA and CSA in the framework of the scientific project SOAR-EU 6779. Ortophotos have been provided by PNOA – ©Instituto Geográfico Nacional de España.

I would like to take this few lines to express my most sincere gratitude to all that make this work possible, either by providing me with scientific guidance, by supporting me with their love and friendship or, in most cases, both.

I want to acknowledge my thesis advisors, Juan Manuel López and Josep Arnal, for paving the way with their deep understanding, professionalism, and always wise advices. Their support has transcended the academical plane, always concerned about my well being and always ready to lend me a hand, whatever the matter. For sure, I know I can count them among my friends. I am also grateful to the rest of the crew on the University of Alicante, on the one hand for supporting my work, but specially for the uncountable hours of fun spent with them. I don't know how Fernando Vicente remains sane after spending so many hours working by my side... I will always remember the times spent together and hope that some part of me remains within you all.

I would also like to thank the people of the Université de Rennes, specially Laurent Ferro-Famil for his guidance during my short stage there. Being there was one of the most enriching experiences of my life, I felt really welcomed and discovered some skills I didn't even know I had (not sure if I can count climbing among them, yet...).

Of course, I must also thank my friends back in Benidorm, always ready to cheer me up when overwhelmed by work, so that I will retake it with renewed energies. There is no easy way to repay you for all the good moments you gave me.

I want to thank my parents for always backing me up, with their affection and their confidence in me. Your unconditional support has been essential to achieving each of my small successes.

Finally, my greatest thanks to Mariví, whose love, understanding and motivation has always pushed me forward, far beyond the limits sometimes I set to myself unconsciously. I will do my best to be as caring as you are to me, for the rest of times.

Contents

CAPÍTULO 1

Síntesis

1.1 Introducción

LA monitorización de deformaciones de la superficie terrestre ha sido siempre una cuestión tan importante como problemática. Fenómenos como el levantamiento o la subsidencia (hundimiento) de una zona pueden evolucionar a lo largo de años o décadas, y el orden de magnitud de la velocidad de deformación es habitualmente inferior a la precisión de los sistemas de medida convencionales. Tanto subsidencia como levantamiento son procesos geológicos de gran impacto en zonas urbanas, donde deformaciones de escasos centímetros pueden deteriorar estructuras o incluso desestabilizarlas, con el consiguiente riesgo material y humano.

Los métodos tradicionales para el estudio de deformaciones, basados en el despliegue de instrumentación *in situ* (por ejemplo extensómetros o redes GPS), resultan costosos y difíciles de mantener, con el inconveniente añadido de proporcionar únicamente medidas puntuales para ubicaciones determinadas. En los últimos años, las técnicas basadas en interferometría diferencial SAR[1] (DInSAR) se han establecido como la herramienta más adecuada para la monitorización de áreas extensas durante periodos temporales largos. Estas técnicas son capaces de obtener mapas de deformación, con precisión milimétrica y coberturas kilométricas, a partir del análisis de series de imágenes de reflectividad electromagnética adquiridas por sensores SAR embarcados en satélites (ERS-1, ERS-2, Envisat, Radarsat, TerraSAR-X, etc.) sobre la zona de estudio. Aunque las políticas de adquisición de datos pueden variar para distintos sensores, para muchas zonas es posible encontrar un histórico de imágenes SAR adquiridas por estos sensores, permitiendo así estudiar también la evolución de la superficie terrestre en los instantes previos a un determinado evento (por ejemplo, un terremoto o un deslizamiento de tierra). Esto supone otra ventaja frente a las técnicas basadas en instrumentación *in situ*, ya que ésta se instala generalmente después del evento en cuestión, lo que dificulta el estudio de los factores desencadenantes.

[1] *Synthetic Aperture Radar*. Radar de Apertura Sintética

Existen, no obstante, diversos factores que limitan la aplicabilidad de las técnicas de interferometría diferencial SAR, como los cambios en las condiciones atmosféricas en los distintos momentos de adquisición, la decorrelación espacial, debida a los cambios en la geometría de adquisición de las imágenes, o la decorrelación temporal, debida a los cambios experimentados por la escena entre adquisiciones. Con el objetivo de minimizar el impacto de éstos y otros factores, a finales de los 90 comenzaron a aparecer una serie de técnicas que se engloban bajo la terminología *Persistent Scatterers Interferometry* (PSI, interferometría de dispersores persistentes). En lugar de procesar todos los píxeles de una escena, este tipo de técnicas construyen una red de píxeles cuya respuesta es considerada fiable *a priori* según ciertos criterios de calidad (píxeles candidatos, PC).

Las técnicas PSI han experimentado un desarrollo significativo desde sus primeras versiones, y han sido probadas con éxito en una gran variedad de escenarios. No obstante, su desempeño está condicionado en gran medida por la densidad de píxeles estables encontrados en la zona de estudio. Estos píxeles suelen estar asociados a estructuras construídas por el hombre, como pueden ser edificios, vallas metálicas, etc. Hay que tener en cuenta que la señal de retorno medida por el sistema SAR dependerá en gran medida del canal polarimétrico con el que trabaje. Por tanto, estructuras cuya respuesta electromagnética se consideraría de calidad para un determinado canal pueden presentar una respuesta inestable, muy atenuada o incluso resultar invisibles para otros canales, en función de su orientación y sus propiedades físicas. Sin embargo, las técnicas PSI han sido formuladas y aplicadas tradicionalmente a datos adquiridos en una única polarización (generalmente horizontal o vertical), principalmente debido a la carencia de satélites SAR operando en múltiples polarizaciones y adquiriendo imágenes de una misma zona a intervalos regulares.

Por su parte, la polarimetría SAR cuenta con una larga trayectoria en el ámbito de la clasificación y segmentación de imágenes (discriminación de áreas urbanas y rurales, clasificación de cultivos, etc.) así como en la inversión de parámetros físicos (estimación de la altura de bosques y biomasa, humedad del suelo, grosor de hielo, etc.). Una vez más, debido a la ausencia de satélites SAR polarimétricos, el uso de series temporales polarimétricas había estado limitado a algunas campañas con cobertura limitada, haciendo uso de SAR aerotransportados o sistemas SAR con base en tierra. Afortunadamente, este escenario ha cambiado en los últimos años con el lanzamiento de nuevos y modernos satélites SAR habilitados con distintos modos de operación polarimétricos y capaces de adquirir imágenes de una misma zona con un tiempo de revisita (tiempo entre adquisiciones) razonablemente reducido, como son TerraSAR-X (DLR, Centro Aeroespacial Alemán), ALOS-PALSAR (JAXA, Agencia Japonesa de Exploración Aerospacial), Radarsat-2 (CSA, Agencia Espacial Canadiense) o los futuros Sentinel-1 (ESA, Agencia Espacial Europea) y RCM, Radarsat Constellation Mission (CSA).

Esta tesis parte motivada por la posibilidad de encontrar nuevas formas de explotar la diversidad polarimétrica ofrecida por los nuevos sensores SAR satélite de manera eficaz. En particular, partimos de la hipótesis de que la polarimetría puede contribuir a mejorar el desempeño de las técnicas de interferometría diferencial SAR convencionales, y en especial de las técnicas PSI, permitiendo detectar un mayor número de píxeles estables o aumentado la calidad de los píxeles previamente localizados.

Una vez planteado el objetivo global, a continuación se detallan los objetivos concretos de esta tesis:

1. Propuesta e implementación de algoritmos DInSAR que aprovechen de manera óptima los datos adquiridos por sensores SAR polarimétricos, prestando especial atención a los datos proporcionados por sensores satelitales, dado su potencial en términos de cobertura y operatividad.
2. Evaluación de los algoritmos propuestos empleando imágenes SAR adquiridas usando diferentes modos polarimétricos, y comparación de los resultados con los conseguidos usando datos no polarimétricos. En especial, se estudiará el aumento de densidad de los mapas obtenidos empleando técnicas PSI.
3. Determinación de la configuración polarimétrica ideal para el estudio de zonas urbanas, de interés prioritario por los mencionados riesgos económicos y humanos asociados al deterioro de estructuras por deformaciones del terreno.

En el presente documento se recopilan las publicaciones más significativas fruto de esta tesis, así como una síntesis de los resultados y conclusiones alcanzadas. El texto se ha organizado en cuatro apartados, más publicaciones y apéndices, constituyendo esta sección de **Introducción** una presentación general de la motivación, objetivos y estructura de este trabajo.

En el apartado **Estado del arte**, con el objetivo de que esta tesis sea autocontenida, se ofrece un resumen del estado del arte y una introducción muy concisa de los principales conceptos y tecnologías implicadas.

En la sección **Resultados** se recopilan y comentan los resultados más significativos alcanzados en esta tesis.

Finalmente, en la sección **Conclusiones** se discuten las principales conclusiones alcanzadas en esta tesis y las futuras líneas de investigación abiertas.

El texto de este documento está sustentado por los artículos anexos, publicados en dos de las revistas de más impacto del sector: *IEEE Geoscience and Remote Sensing Letters*, e *IEEE Transactions on Geoscience and Remote Sensing*. Asimismo, se incluye un listado completo de publicaciones en revistas y congresos internacionales generados durante el desarrollo de esta tesis.

1.2 Estado del arte

COMO se indica en la introducción, la meta principal de este trabajo ha sido mejorar las técnicas modernas para el estudio de deformaciones de la superficie terrestre basadas en teledetección, en particular las técnicas PSI, dada su probada eficacia en escenarios urbanos.

Esta sección está diseñada para servir como introducción a las tecnologías relacionadas con el tema de esta tesis, así como para ayudar a describir el estado del arte al inicio de este trabajo de investigación.

1.2.1 Teledetección SAR

El término teledetección hace referencia a la medición de propiedades físicas de un objeto sin que exista contacto directo entre el objeto y el sensor. Dependiendo de la fuente de la energía medida, los sensores pueden ser clasificados como sensores pasivos, que registran la energía procedente de una fuente externa (cámaras fotográficas, radiómetros, etc.) o bien sensores activos, cuando emiten energía sobre el objeto y capturan la señal reflejada, como es el caso de los sistemas RADAR (*Radio Detection And Ranging*, detección y medición de distancias por radio). Los sensores radar emiten pulsos electromagnéticos (EM) y procesan los ecos devueltos por el blanco o escena para medir distancias, altitudes, velocidades, etc. Dadas su cobertura y práctica inmunidad a las condiciones climáticas y de iluminación, las técnicas basadas en sistemas SAR (*Synthetic Aperture Radar*, Radar de Apertura Sintética) son la opción habitual para la monitorización de deformaciones terrestres.

Los sistemas SAR son sistemas radar coherentes (preservan información de fase y amplitud) destinados a generar imágenes de reflectividad EM de alta resolución. La tecnología SAR comenzó a desarrollarse durante los años sesenta como una manera de superar las limitaciones de los sistemas Radar de Apertura Real (RAR). Para construir imágenes 2D de la superficie terrestre, los sistemas RAR barren la escena con un haz EM idealmente estrecho. En el caso de sistemas satelitales o aerotransportados, una geometría de observación lateral (SL, *Side-Looking*) proporciona sensibilidad en *rango* (distancia a la trayectoria del radar), mientras que en *azimut* (dirección de vuelo de la plataforma) la resolución viene determinada por la anchura del haz. En general, cuanto mayor es la antena con respecto a la longitud de onda de los pulsos, más estrecho es dicho haz. Esto limita el desempeño de los sistemas RAR satelitales y aerotrasportados, puesto que el tamaño de la antena estará restringido por limitaciones de peso y dificultades en el despliegue, y el uso de longitudes de onda menores generalmente conlleva una mayor atenuación atmosférica, además de un mayor consumo energético.

Los sistemas SAR, en cambio, usan antenas más pequeñas y menos directivas, que emiten pulsos a intervalos regulares (PRF, *Pulse Repetition Frequency*), también en configuración SL, mientras se desplazan a lo largo de la trayectoria de vuelo. Combinando coherentemente los ecos recibidos en las diferentes posiciones, y empleando la información de desplazamiento del sensor, el sistema es capaz de sintetizar una antena de mayor tamaño. La Figura 2.1 ilustra el modo de operación SAR convencional, el modo *stripmap*, en el cual se asume una dirección fija de apuntamiento del sensor a lo largo de la trayectoria. A la franja de superficie mapeada por el SAR se la denomina *swath*.

Nótese que, dada la configuración SL, las elevaciones del terreno producen distorsiones geométricas en la imagen SAR. Las distorsiones más comunes son *foreshortening*,

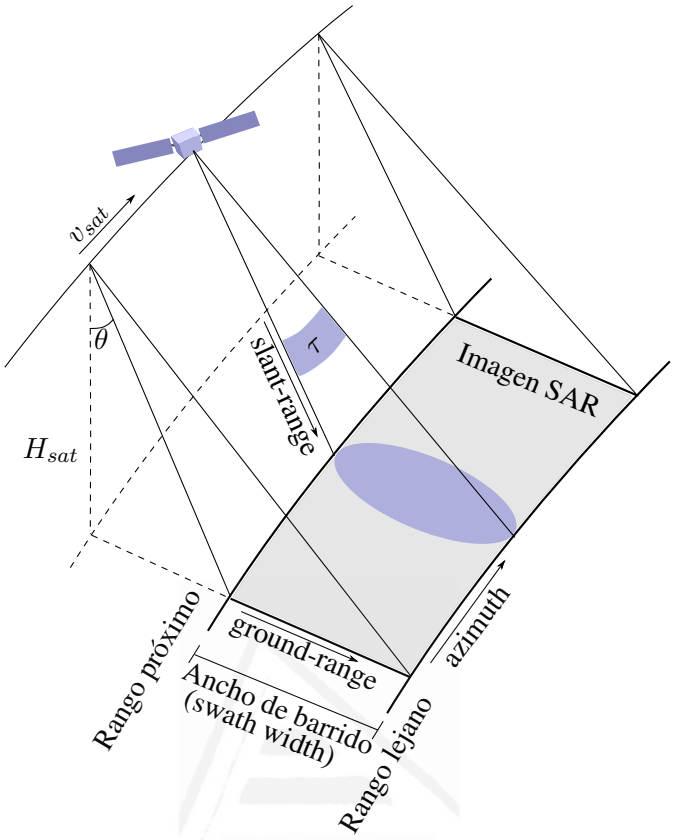

Figura 1.1. Geometría de adquisición SAR.

layover y *shadowing*. El *foreshortening* provoca que las pendientes del terreno encaradas al radar aparezcan contraídas, dando la impresión de que se inclinan hacia el sensor. Cuando el ángulo de la pendiente es igual, o incluso superior, al ángulo del incidencia, puntos en el valle pueden tener una mayor distancia oblicua al sensor (*slant-range*) que puntos en la cima, y por tanto la proyección de la pendiente encarada al radar se invierte y aparecen ambigüedades: diferentes puntos en valle, ladera y cima son mapeados en el mismo píxel, que aparece más brillante. Este efecto es conocido como *layover*, y no puede ser resuelto mediante geocodificación, así que estas áreas también aparecerán más brillantes cuando se reproyecte de coordenadas radar a coordenadas geográficas. Finalmente, pendientes opuestas a la iluminación del radar y con ángulos más pronunciados que el ángulo de incidencia producen sombras (*shadowing*) en la imagen SAR, puesto que no devuelven ningún eco.

Otro efecto no deseado inherente a todo sistema SAR es el moteado o *speckle*, originado por la combinación coherente de los retornos de múltiples centros de dispersión (*scattering*) dentro de la celda de resolución. Estas interferencias producen un efecto similar al ruido "sal y pimienta" que es característico de las imágenes SAR.

Como se mencionó anteriormente, los sistemas SAR son sistemas radar coherentes, luego miden tanto la amplitud como la fase de la señal retornada. Como resultado, producen imágenes de reflectividad complejas, comúnmente referidas como *Single-Look Complex*

(SLC), donde a cada celda de resolución se le asigna un valor complejo de reflectividad. La amplitud de la imagen SLC nos da una idea de la potencia retornada. En cuanto al término de fase, su valor depende de la distancia (rango) entre el sensor y el blanco. No obstante, al ser esta distancia de un orden muy superior a la longitud de onda (centenas de kilómetros frente a pocos centímetros), el pulso electromagnético completará un gran número de ciclos de fase durante su trayecto de ida y vuelta. Como la distancia exacta al blanco es, a priori, desconocida, el número total de ciclos no puede ser determinado. Por tanto, no se puede obtener información útil de la fase en este punto.

Información adicional acerca de los sistemas SAR, su evolución y la interpretación de las imágenes SAR puede encontrarse en [Carrara et al., 1995][Oliver and Quegan, 1998].

1.2.2 Interferometría e Interferometría Diferencial SAR

Las técnicas de Interferometría SAR (InSAR) nacen con el objetivo de medir distancias relativas y mapear la topografía de una zona, explotando la información de fase de dos imágenes SAR adquiridas desde posiciones diferentes, bien usando dos antenas (pasada única o *single-pass*) o bien realizando varias pasadas (*repeat-pass*). Combinando dos adquisiciones SAR, de modo similar al funcionamiento de la visión humana, se obtiene sensibilidad a las diferencias angulares, y se puede obtener información topográfica a partir de la diferencia de camino recorrido, relacionada con la fase interferométrica. La distancia física entre las órbitas satelitales en el momento de la adquisición se conoce como *baseline espacial*, mientras que la separación temporal (en caso de adquisiciones no simultáneas) se conoce como *baseline temporal*.

La fase interferométrica puede entenderse como una mezcla de contribuciones de fase, incluyendo el término topográfico, el término de deformación (en el caso de que la escena haya cambiado su posición entre adquisiciones), un término asociado a cambios en las condiciones atmosféricas, y ruido. Hay que tener en cuenta que, en este punto, la fase interferométrica aún presenta una ambigüedad en ciclos de fase, así que su valor estará comprendido entre $-\pi$ y π, lo que aparecerá como "franjas" en la imagen de fase.

La topografía puede ser extraída de la fase interferométrica cancelando las contribuciones no deseadas. Por ejemplo, las contribuciones debidas a deformaciones de la superficie y a variaciones atmosféricas pueden minimizarse reduciendo el tiempo entre adquisiciones (*repeat time*) o usando interferometría *single-pass*.

Una vez aislado el término topográfico, la fase interferométrica está directamente relacionada con la altura superficial, y la frecuencia de las franjas de fase sirve como indicador de lo pronunciado de la topografía. Sin embargo, para proporcionar valores de fase absolutos, la fase interferométrica tiene aún que atravesar una etapa de desambiguación conocida como "desenrollado de fase", esto es, los ciclos de fase modulo 2π deben ser transformados en valores de fase absolutos, continuos, de modo que se pueda aplicar una conversión directa de fase a altura. Finalmente, todos los valores de altura en coordenadas radar (rango, azimut)

se reproyectan en coordenadas geográficas, en un proceso conocido como *geocodificación*, para generar por último un modelo digital de elevación (DEM, *Digital Elevation Model*).

Las técnicas InSAR son útiles para obtener la topografía de áreas extensas a partir de observaciones SAR. Las técnicas de Interferometría Diferencial SAR (DInSAR) van un paso más allá, permitiéndonos medir la deformación experimentada por el terreno en el lapso de tiempo entre adquisiciones, siempre que la topografía de la zona ya sea conocida o bien pueda ser obtenida usando InSAR convencional.

En otras palabras, el objetivo de las técnicas DInSAR es aislar el término relacionado con la deformación frente al resto de contribuciones a la fase interferométrica. Entonces, las franjas interferométricas estarán relacionadas con la deformación en la dirección de observación (*line-of-sight*) del mismo modo que en el caso InSAR estaban relacionadas con la topografía.

La cancelación de la componente topográfica es un paso clave en el procesado DInSAR. Existen diferentes enfoques sobre cómo eliminar el término topográfico de la fase interferométrica, como se describe por ejemplo en [Mora, 2004]. El esquema usado en este trabajo para la formación de interferogramas diferenciales recurre a un DEM externo para estimar y cancelar el término de fase topográfico.

Además de las posibles imprecisiones del DEM, existen varios factores que pueden degradar la calidad del interferograma diferencial. Podemos resumir estas limitaciones en cuatro puntos:

- **Decorrelación temporal**: Debido a la necesidad de usar grandes baselines temporales (lapso de tiempo entre imágenes) para monitorizar desplazamientos lentos, pueden aparecer problemas de decorrelación temporal, especialmente en zonas con vegetación, donde las condiciones de retrodispersión de la escena pueden cambiar considerablemente entre adquisiciones.

- **Decorrelación geométrica**: El cambio en la geometría de adquisición de las dos imágenes SLC conlleva un desplazamiento relativo de su espectro en rango. Para la formación del interferograma, sólo será útil la porción del espectro común a ambas imágenes. La baseline espacial que hace que los espectros en rango no tengan banda común se conoce como *baseline crítica*. Como ejemplo, para los satélites ERS, con un ancho de banda de 18 MHz, la baseline crítica es de aproximadamente 1200 m, aunque en la práctica es preferible el uso de baselines mucho menores.

- **Artefactos atmosféricos**: Los cambios en las condiciones atmosféricas pueden producir franjas de fase en el interferograma diferencial, que presentan magnitudes y características espaciales similares al término asociado a la deformación, y por tanto resulta difícil separar ambas contribuciones.

- **Errores en el desenrollado de fase**: En la mayoría de situaciones, los interferogramas se ven seriamente afectados por ruido y artefactos atmosféricos, por lo que requerirán

el uso de técnicas de desenrollado de fase avanzadas. No obstante, estas técnicas no son infalibles y, en general, la capacidad de extraer la componente de deformación a partir de un único interferograma diferencial será muy limitada.

Considerando estos aspectos, encontramos que sólo una porción de las imágenes SLC disponibles serán adecuadas para producir interferogramas diferenciales útiles.

Con el objetivo de suprimir o mitigar estas fuentes de error, se han propuesto una serie de técnicas DInSAR avanzadas. Estas técnicas logran estimaciones más robustas y precisas, combinando para ello la información proporcionada por múltiples interferogramas diferenciales. En lugar de procesar todos los puntos de la escena, las técnicas DInSAR más avanzadas seleccionan sólo aquellos píxeles considerados fiables *a priori* de acuerdo con ciertos criterios de calidad. Estos métodos son generalmente englobados bajo el término Interferometría de Dispersores Persistentes (PSI, *Persistent Scatterers Interferometry*). La optimización del desempeño de las técnicas PSI mediante el uso de polarimetría es el objetivo principal de esta tesis.

Podemos encontrar información adicional sobre InSAR y DInSAR en [Hansen, 2001].

1.2.3 Interferometría de Dispersores Persistentes

Desde su concepción a finales de los 90, las técnicas de Interferometría de Dispersores Persistentes (PSI, *Persistent Scatterers Interferometry*) se han utilizado ampliamente para monitorizar deformaciones de la superficie terrestre [Ferretti et al., 2000][Ferretti et al., 2001]. Las técnicas PSI explotan la información de un conjunto de interferogramas, obtenidos a partir de una serie de imágenes SAR adquiridas en distintas fechas, para extraer información precisa de la evolución de la deformación del terreno a lo largo del tiempo. A diferencia de los métodos convencionales de interferometría diferencial, las técnicas PSI seleccionan para el procesado sólo aquellos puntos considerados de antemano fiables (*candidatos*), de acuerdo con cierto criterio de calidad. En entornos urbanos, donde es habitual encontrar dispersores puntuales deterministas (llamados Persistent Scatterers, PS) asociados a reflexiones intensas y estables en construcciones humanas, el criterio de calidad más empleado es el índice de dispersion de amplitud (D_A), usado como forma indirecta de conocer la desviación estándar de fase [Ferretti et al., 2001]. En entornos naturales, sin embargo, se prefiere la coherencia promedio $\overline{\gamma}$ como indicador de calidad de fase [Berardino et al., 2002][Mora, 2004]. Los puntos seleccionados usando este método se conocen normalmente como píxeles coherentes (CP) y suelen corresponden a dispersores distribuidos estables, más que a dispersores puntuales. Nótese que el estimador de máxima verosimilitud (*maximum likelihood*, ML) de la coherencia interferométrica requiere, generalmente, llevar a cabo un promediado de muestras vecinas (proceso referido habitualmente como *multi-looking)* y, como consecuencia, la resolución espacial se ve degradada en este caso.

Después de esta selección preliminar, se construye una red espacial de píxeles, bien enlazando cada píxel candidato con todos los candidatos vecinos dentro de un radio, o bien

usando técnicas de triangulación (por ejemplo, Delaunay). Seguidamente, se ajustará un modelo dependiente de la velocidad de deformación (por lo general asumida lineal en este punto) a las diferencias de fase asociadas a cada enlace. De este modo, la contribución de términos asumidos prácticamente iguales para píxeles vecinos, como el término atmosférico, se verá cancelada o reducida significativamente. Aquellos enlaces que no alcancen un determinado nivel de ajuste o coherencia de modelo (función de coste) serán eliminados, y los píxeles desconectados se descartarán como válidos y por lo tanto serán ignorados en subsiguientes etapas del procesado.

Una vez ajustado el modelo lineal, la componente no lineal de la velocidad extraerse a partir de los residuos de fase (diferencia entre la fase original y la modelada) mediante filtrados espaciales y temporales, explotando las diferencias en el comportamiento espacio-temporal del ruido, la contribución atmósferica y la deformación no lineal, como se describe por ejemplo en Mora [2004].

Por lo general, el método se comportará de manera más robusta cuanto mayor sea la densidad de píxeles fiables seleccionados. Sin embargo, una relajación excesiva del criterio de calidad para incrementar el número de píxels entraña dificultades en el procesado, puesto que aparecerán nuevas fuentes de error. Por lo tanto, se ha de alcanzar un compromiso a la hora seleccionar el umbral en el criterio de calidad.

Un libro de referencia en este área es [Kampes, 2006].

1.2.4 PolSAR y PolInSAR

Como todo sistema radar, un SAR emite ondas electromagnéticas (transversales) y analiza los ecos recibidos para medir las características del blanco. Una de las propiedades fundamentales de tales ondas electromagnéticas es su estado de polarización, que puede definirse como la figura geométrica descrita por el extremo del vector campo eléctrico en el plano perpendicular a la dirección de propagación.

La mayoría de sistemas SAR emiten ondas linealmente polarizadas, esto es, la oscilación del campo eléctrico ocurre en una única dirección (por ejemplo, polarización vertical u horizontal) y miden la señal devuelta en la misma dirección de polarización o "canal" (p. ej. transmisión y recepción vertical o, para abreviar, VV). De manera similar, otros sistemas SAR se diseñan para emitir y recibir ondas polarizadas circularmente o con polarización elíptica.

Cuando las ondas incidentes excitan el blanco, entre otros efectos, éste re-radia un campo EM. Dependiendo de las propiedades físicas del blanco, como su geometría, orientación o conductividad, el estado de polarización de la onda retornada puede ser diferente, o incluso ortogonal, a aquél de la onda incidente. En la mayoría de casos, la onda retornada consiste en una mezcla de mecanismos de dispersión (a lo que habitualmente nos referimos como onda "parcialmente polarizada"), que no pueden ser separados usando un sistema de canal único.

Los sistemas SAR polarimétricos (PolSAR) se desarrollaron con el objetivo de extraer propiedades físicas adicionales del blanco, además de su reflectividad EM. Con este propósito, los sistemas PolSAR transmiten y reciben diferentes combinaciones de polarización. En lugar de obtener un único coeficiente de reflectividad complejo, un sistema PolSAR proporciona una matriz de coeficientes para cada píxel de la escena, con tantos elementos como combinaciones de canales de transmisión-recepción. Este modo de organizar los datos PolSAR se conoce como la matrix de *Sinclair* o de *scattering* (dispersión), $\mathbf{S}$. Sobre esta matriz pueden aplicarse, por ejemplo, una serie de teoremas de descomposición, que nos permitirán expresar los datos como la contribución de varios mecanismos de dispersión "canónicos" (reflexión especular o superficial, volumen aleatorio, etc.) obteniendo así una visión sobre las características físicas de la escena.

Un formalismo usado habitualmente, que resulta de gran ayuda para la extracción de información física a partir de la descripción polarimétrica del objeto dispersor (*scatterer*), consiste en la construcción del llamado "vector de blanco" o *target vector*, $\mathbf{k}$. El vector de blanco se forma simplemente vectorizando la matriz de scattering $\mathbf{S}$, lo que matemáticamente se realiza proyectando la matriz de scattering sobre un conjunto de matrices base ortonormales (generalmente las matrices de spin de Pauli), como se describe por ejemplo en [Cloude and Papathanassiou, 1998]. Aunque se pueden usar diferentes bases para la vectorización, el conjunto de Pauli es una elección común porque los elementos del vector resultante estarán estrechamente relacionados con la física de dispersión de ondas, y permitirán por tanto una mejor interpretación de los mecanismos de dispersión. Es más, calculando el producto escalar de $\mathbf{k}$ con su transpuesto conjugado, obtenemos la *matriz de coherencia* $\mathbf{T}$, muy útil para describir blancos parcialmente polarizados cuando entran en juego estadísticos de segundo orden.

Se ha llevado a cabo mucho trabajo en el ámbito de la descomposición de blancos basada en matrices $\mathbf{T}$. Nótese que, en entornos dinámicos, es habitual que los elementos dispersores no estén fijos, sino sujetos a variación espacial y temporal. Estos blancos se denominan habitualmente "dispersores parciales", ya que son análogos a las ondas parcialmente polarizadas y, en general, se pueden describir de manera más precisa si se considera su dispersión como un proceso estocástico en espacio y tiempo. Por tanto, los dispersores parciales pueden describirse a partir de los momentos de segundo orden de las fluctuaciones, que serán extraídos de las matrices $\mathbf{T}$ [Lee and Pottier, 2009]. Una propiedad interesante de las matrices $\mathbf{T}$ es que su descomposición en autovectores proporciona un conjunto de vectores de proyección ortonormales, asociados a diferentes mecanismos de dispersión dentro de la celda de resolución, y cuyos autovalores asociados nos dan una idea de la contribución de cada mecanismo a la dispersión total.

La interferometría SAR polarimétrica (PolInSAR) se desarrolló con el objetivo de separar verticalmente los centros de fase correspondientes a diferentes mecanismos de dispersión dentro de una misma celda de resolución [Cloude and Papathanassiou, 1998]. Las técnicas PolInSAR tienen una gran variedad de aplicaciones potenciales. Por ejemplo, en ecosistemas forestales pueden ser usadas para estimar la distancia relativa entre las copas de los árboles (dispersión en volumen aleatorio) y el tronco-suelo (mecanismo de doble rebote o diedro), permitiendo así medir la altura de los árboles o estimar la cantidad de biomasa

sobre áreas extensas.

A fin de generar interferogramas a partir de datos polarimétricos, un determinado vector de blanco ($\mathbf{k}$) puede ser proyectado sobre un vector de proyección unitario (ω), dando como resultado un coeficiente escalar complejo (μ), que será análogo al tipo datos obtenidos por los sistemas de polarización única (single-pol) [Cloude and Papathanassiou, 1998]. Por lo tanto, estos coeficientes podrán ser combinados para formar un interferograma, de manera similar a la interferometría SAR convencional. Los vectores de proyección pueden elegirse de tal modo que los coeficientes resultantes estén relacionados con un mecanismo de dispersión particular, o pueden ser elegidos de manera que se optimice la coherencia interferométrica.

La posibilidad de optimizar la coherencia interferométrica, y potencialmente cualquier otro indicador de calidad deseado, mediante la modificación de los vectores de proyección, es uno de los aspectos que se explotarán en esta tesis.

Una completa revisión de PolSAR y PolInSAR se puede encontrar en [Cloude, 2010] y [Lee and Pottier, 2009].

1.2.5 Polarimetría e Interferometría de Reflectores Persistentes

La primera aplicación de la polarimetría a PSI para entornos urbanos se propuso en [Perissin and Ferretti, 2009], donde se hizo uso de datos dual-pol adquiridos por el satélite Envisat (canales incoherentes) para reconocer características físicas de los blancos y así clasificar los PS. En [Dheenathayalan and Hanssen, 2011] se presenta también una estrategia de clasificación de PS apoyada por polarimetría, en el contexto de la estimación de movimientos relativos entre terreno y edificaciones, usando datos dual-pol adquiridos por TerraSAR-X (canales coherentes).

Con el objetivo de aprovechar aún más la diversidad polarimétrica en las etapas iniciales del procesado PSI, en [Pipia et al., 2009a] se propuso un algoritmo dirigido a incrementar la calidad y cantidad de píxeles pre-seleccionados para el procesado. El algoritmo propuesto consiste en seleccionar, del conjunto de canales proporcionados por el sensor, aquel que proporciona la mayor coherencia interferométrica promedio para cada píxel. El algoritmo se evaluó usando datos dual-pol (HH, VV) adquiridos por un SAR con base en tierra, logrando una mejora significativa en la densidad de puntos CP seleccionados y demostrando por vez primera el potencial de la polarimetría en PSI. Este enfoque, aunque ilustrativo, conduce sólo a una solución subóptima, ya que sólo considera una fracción (proyecciones discretas) del espacio polarimétrico disponible. Posteriormente, en Pipia et al. [2009b] se propone un método de optimización polarimétrica de la coherencia, válido para sistemas SAR con base en tierra y baseline nula (sin separación perpendicular entre antena emisora y receptora). Este método explota el hecho de que este tipo de sistemas SAR no es sensible a la topografía, como se discute en la publicación adjunta [Navarro-Sanchez et al., 2010], lo que generalmente no es aplicable en plataformas SAR satelitales.

Alentada por estos trabajos preliminares, esta tesis se ha dedicado a la búsqueda de técnicas eficaces y eficientes para la optimización de la PSI por satélite mediante polarimetría, con el fin de beneficiarnos del pleno potencial de los sistemas SAR de nueva generación.

1.3 Resultados

EL punto de partida de este estudio fue la definición de un marco general para la optimización polarimétrica de técnicas PSI, basado en la maximización (o minimización, según corresponda) de los parámetros de calidad considerados para la selección de píxeles válidos [Navarro-Sanchez et al., 2010]. Para realizar esta optimización, se lleva a cabo una búsqueda, píxel a píxel, a fin de encontrar la proyección o "canal" que proporciona los mejores resultados para cada punto de la escena. Nótese que la búsqueda no está limitada exclusivamente a los canales proporcionados por el sensor (p. ej. horizontal, vertical y cruzada), sino que se tienen en cuenta las posibles combinaciones lineales entre canales con el objetivo de cubrir todo el espacio polarimétrico disponible.

El esquema propuesto cuenta con la ventaja de poder ser aplicado a cualquier técnica PSI conocida con mínimas modificaciones, a modo de pre-procesado. De esta manera, el procesador PSI desarrollado por la Universidad de Alicante en proyectos anteriores, y que implementa distintos métodos PSI, ha sido adaptado para acoger los nuevos algoritmos polarimétricos, con el fin de evaluar su desempeño.

Los métodos presentados en este trabajo han sido adaptados y probados para los criterios de calidad más habituales: selección de píxeles con un bajo índice de dispersión de amplitud (D_A), calculado sobre el conjunto completo de imágenes SAR, y selección por alta coherencia promedio ($\overline{\gamma}$), obtenida sobre un conjunto de interferogramas filtrados (*multi-look*).

La sensibilidad de estos parámetros a la polarimetría se demostró en [Navarro-Sanchez et al., 2010] usando una serie de imágenes dual-pol (polarizaciones horizontal y vertical) adquiridas por el satélite alemán TerraSAR-X sobre el área urbana de Murcia (España). Valores tanto de D_A como de $\overline{\gamma}$ se representaron en función del canal polarimétrico (dado por una parametrización del vector de proyección, ω) para un conjunto arbitrario de puntos de la escena, mostrando diferencias de magnitud significativas para los diferentes canales, especialmente evidentes en el caso de D_A. Hay que tener en cuenta que, a diferencia de la coherencia, la dispersión de amplitud se calcula para datos *single-look*, es decir, no existe promediado entre píxeles vecinos. En consecuencia, el comportamiento polarimétrico de cada celda de resolución es más probable que sea determinado por la geometría de dispersores puntuales dominantes, con un mecanismo de dispersión bien definido, en lugar de venir dado por las características medias de un área extensa.

Seleccionando, para cada píxel, el canal que optimiza el criterio de calidad, es posible incrementar drásticamente el número de píxeles seleccionados como válidos para el

procesado posterior, sin necesidad de modificar los umbrales de selección, como se muestra en [Navarro-Sanchez et al., 2010]. Como ejemplo, para un umbral de coherencia de 0,8, un 17,29 % de los píxeles de la escena fueron seleccionados sobre el área de estudio para los datos optimizados (dual-pol), frente a sólo un 7,64 % de píxeles seleccionados para el canal VV (transmisión y recepción vertical) por sí solo. Esto significa una densidad de puntos seleccionados de más del doble, lo cual es un incremento espectacular, especialmente si tenemos en cuenta que sólo se ha incorporado al procesado un canal de medida adicional (HH, transmisión y recepción horizontal). Como podíamos esperar, el incremento es incluso superior en el caso de D_A, debido a la mayor sensibilidad de los datos *single-look* a las características polarimétricas. Por ejemplo, considerando un umbral típico de 0,25, un 30,88 % de los píxeles son seleccionados para los datos optimizados dual-pol, frente a un 7,72 % para el canal VV por sí solo, lo que significa una densidad de más del triple de píxeles candidatos.

Es importante tener en cuenta que, en este método, forzamos que el vector ω correspondiente a cada píxel sea el mismo para el conjunto completo de imágenes. Esto puede interpretarse como la selección del mecanismo de dispersión que captura mejor las características polarimétricas estables del área cubierta por la celda de resolución. Esta restricción es necesaria para que el método PSI pueda construir series temporales consistentes de fases relacionadas con deformaciones. De otro modo podríamos seleccionar, para el mismo píxel, diferentes mecanismos de dispersión para instantes distintos, correspondientes a diferentes centros de fase en la celda de resolución que podrían tener alturas distintas. Como resultado, estas diferencias de fase a lo largo del tiempo podrían se interpretadas indebidamente como cambios de fase debidos a deformación.

Los primeros resultados de deformación basados en estas técnicas fueron obtenidos usando una serie de imágenes dual-pol (HH, VV) adquiridas por TerraSAR-X, mostrando un incremento significativo en la densidad de puntos y, por tanto, un incremento de cobertura de los mapas generados [Navarro-Sanchez and Lopez-Sanchez, 2012]. Además, como producto adicional de la optimización, se comprobó la capacidad de los algoritmos para proporcionar una clasificación de los distintos mecanismos de dispersión presentes en la escena (reflexión en superficie, doble rebote, difusión), asociados a su vez a distintos tipos de objeto (edificios, vegetación, asfalto, etc.). Los mecanismos de dispersión dominantes están relacionados con los vectores de proyección óptimos encontrados. Se observa que los píxeles seleccionados como dispersores persistentes o puntos coherentes tienden a presentar un mecanismo de dispersión tipo diedro, mecanismo relacionado generalmente con reflexiones terreno-edificio (doble rebote).

En [Navarro-Sanchez and Lopez-Sanchez, 2011] se inició el estudio de indicadores de calidad puramente polarimétricos para la selección de píxeles en PSI. Estos indicadores de "estacionariedad polarimétrica" mostraron tener cierta correlación con los criterios de selección clásicos, pero aportaban información complementaria sobre la evolución del blanco.

En este punto, los algoritmos propuestos (basados en una búsqueda de parámetros mediante "fuerza bruta") eran simples, pero computacionalmente costosos, y por tanto su uso estaba limitado a datos con un máximo de dos canales polarimétricos. Por consiguiente, se dirigieron los esfuerzos a mejorar la eficiencia de estos algoritmos, así como a desarrollar

métodos alternativos que, teniendo en cuenta una serie de restricciones, pudieran ofrecer un rendimiento superior y resultados similares. Los nuevos algoritmos fueron evaluados usando datos dual-pol de la ciudad de Murcia (TerraSAR-X) así como datos polarimétricos completos (*full-pol*, HH, VV, HV y VH) adquiridos sobre la ciudad de Barcelona (Radarsat-2). En ambos casos, los mapas de deformación obtenidos muestran un importante incremento de cobertura con respecto a los enfoques PSI convencionales. La mejora es especialmente evidente para el conjunto de datos full-pol, como era de esperar, teniendo en cuenta que el espacio polarimétrico de búsqueda es más amplio [Navarro-Sanchez et al., 2014].

Como contribución más reciente a esta investigación, en [Navarro-Sanchez and Lopez-Sanchez, 2014] se propone un esquema de filtrado adaptativo espacial, guiado por parámetros estadísticos polarimétricos estimados en la dimensión temporal. El uso de estadísticos temporales, en lugar de estadísticos espaciales calculados a partir de píxeles vecinos, supone que la resolución espacial puede mantenerse inalterada en aquellas zonas que no se beneficien del filtrado, preservando detalles como bordes de edificios, farolas y otras estructuras, generalmente de construcción humana. Por lo tanto, el método permite procesar conjuntamente dispersores estables puntuales (PS) y dispersores distribuidos (*distributed scatterers*, DS), esto es, grupos de píxeles colindantes que comparten propiedades de reflectividad similares y que pueden ser considerados como parte del mismo blanco. Por conveniencia, se presenta también un criterio de calidad basado en la desviación estándar de fase estimada, que puede ser usado para la selección tanto de PS como de DS, como se describe en [Navarro-Sanchez and Lopez-Sanchez, 2014].

El uso de esta estrategia de pre-procesado (que se sirve de la información polarimétrica disponible) en conjunción con las técnicas de optimización de PSI propuestas, consigue incrementar la densidad de los mapas de deformación espectacularmente, superando con creces los resultados obtenidos por otras técnicas para los conjuntos de prueba considerados. Para datos TerraSAR-X dual-pol filtrados y optimizados, el área cubierta se incrementa más de 1,5 veces con respecto a datos optimizados no filtrados, y 3,7 veces con respecto a datos single-pol sin filtrar. En cuanto a los datos Radarsat-2 full-pol filtrados y optimizados, la cobertura se incrementa 1,35 veces con respecto a datos optimizados sin filtrar, y 9,3 veces con respecto a datos sin filtrar no optimizados (single-pol). La combinación del filtrado adaptativo y la optimización polarimétrica sobre datos full-pol es la configuración que proporciona los mejores resultados.

Cabe mencionar que, al no disponer de datos de validación medidos para las zonas de estudio usando otros métodos, los resultados de deformación obtenidos se han comparado de manera cualitativa con aquellos obtenidos usando técnicas clásicas, y con resultados de otros investigadores encontrados en la literatura (p. ej. [Herrera et al., 2010][Monserrat et al., 2011]). Los mapas obtenidos usando los métodos polarimétricos desarrollados muestran tendencias de deformación similares para las áreas estudiadas, pero una densidad de píxeles con información de deformación claramente superior

1.4 Conclusiones

ESTA investigación se ha dedicado al desarrollo de nuevos métodos para el control de deformaciones de la superficie terrestre, capaces de explotar de manera eficiente los datos SAR polarimétricos proporcionados por la nueva generación de sensores satélite. Los beneficios de la polarimetría para PSI han sido valorados: se han presentado y evaluado un conjunto de técnicas que combinan PSI y polarimetría, obteniendo mapas de deformación más densos y significativos (con respecto a single-pol), y se ha obtenido una visión de las configuraciones más ventajosas. Con esto, se satisfacen los objetivos primarios de esta investigación.

Se ha propuesto un marco general para el uso de datos polarimétricos en PSI: primero, los datos polarimétricos son convertidos en datos monocanal (análogos a datos single-pol) usando un conjunto de vectores de proyección, seleccionados de modo que se optimice el criterio de calidad usado para la selección de píxeles. Entonces, cualquier técnica PSI diseñada para datos monocanal (single-pol) podrá ser aplicada a los datos proyectados, obteniéndose un incremento general en la calidad y densidad de píxeles seleccionados y procesados.

Siguiendo este esquema general, se han propuesto una serie de algoritmos para la obtención de los vectores de proyección óptimos. Todos los métodos presentados han probado ser capaces de incrementar la cobertura de los mapas de deformación generados en cierto grado con respecto a PSI single-pol. Además, se ha presentado una nueva estrategia de filtrado, junto con una metodología para el procesado conjunto de dispersores puntuales y distribuidos que, en combinación con la optimización polarimétrica, ha sido capaz de producir mapas de deformación con una densidad cerca de 4 veces superior para datos dual-pol, y más de 9 veces superior para datos full-pol, con respecto a los mapas obtenidos a partir de datos single-pol para las escenas urbanas consideradas.

Aunque el uso de datos polarimétricos completos (full-pol) es lo más deseable, los datos dual-pol han probado ser capaces de proporcionar mejoras importantes en la densidad de los mapas, con un coste computacional sustancialmente menor. En escenarios urbanos, como los considerados en este estudio, los mecanismos tipo diedro (reflexiones terreno-edificio), asociados al canal Pauli HH$-$VV, son los más propensos a ser seleccionados como fiables. Por lo tanto, la combinación de los canales polarimétricos HH y VV es susceptible de producir buenos resultados, incluso si no se dispone de datos full-pol. No obstante, hay que tener en cuenta que obtener medidas coherentes de HH y VV conlleva los mismos requisitos que la adquisición full-pol en términos de PRF y reducción de swath, puesto que se requiere una transmisión multiplexada de polarizaciones horizontal y vertical. Sin embargo, como se demuestra en [Navarro-Sanchez et al., 2014], un sistema de polarización híbrida (hybrid-pol, emitiendo polarización circular y recibiendo H y V lineales, sería capaz de obtener una mejora similar, sin las limitaciones anteriormente expuestas. Por consiguiente, hybrid-pol sería la opción preferida en caso de no disponer de datos full-pol.

La validación de los resultados presentados con medidas de campo (*ground-truth*) aún no se ha abordado, y se recomienda como trabajo futuro. No obstante, el incremento en

la densidad de píxeles generalmente contribuirá a la robustez de los métodos PSI, añadiendo redundancia y, por tanto, mejorando la precisión de las estimaciones de fase.

El comportamiento de las técnicas propuestas puede variar para diferentes zonas o tipos de terreno. En particular, hay que tener presente que el rendimiento y la configuración óptima del filtro adaptativo propuesto dependen principalmente de las características de la escena bajo estudio, así como de las especificaciones del sensor. Como línea de investigación futura, se propone revisar cuidadosamente el desempeño del filtro en diferentes escenarios, en función de los parámetros de configuración. Además, distintos tests de hipótesis para la discriminación de áreas homogéneas deben ser estudiados y comparados.

Otra línea de trabajo que merece ser abordada es el estudio de criterios de calidad polarimétricos para la selección de píxeles. Esto permitiría determinar de manera más precisa qué píxeles son adecuados para el procesado, aprovechando la información adicional proporcionada por la polarimetría, abriendo el camino a enfoques alternativos de optimización polarimétrica. Algo de trabajo en esta línea se ha llevado a cabo en [Navarro-Sanchez and Lopez-Sanchez, 2011], del cual se extrae un anticipo de los beneficios potenciales que supondría una investigación exhaustiva en este área.

CHAPTER 2

Summary

2.1 Introduction

MONITORING of Earth's surface deformations has always been a matter as important as complicated. For instance, phenomena as the uplift or the subsidence (sinking) of an area can evolve through years or decades, and the order of magnitude of the deformation velocity is usually lower than the precision of the conventional measure systems. Both subsidence and uplift are geological processes of great impact on urban areas, where deformations of few centimetres can deteriorate structures or even destabilise them, with the consequent material and human risk.

Traditional methods for the study of deformations, based on the deployment of instrumentation *in situ* (as, for instance, extensometers or GPS networks), are costly and difficult to maintain, with the added disadvantage of providing only isolated measures for determined spots. In the last years, techniques based on SAR[1] differential interferometry (DInSAR) have established themselves as the most adequate tool for the monitoring of wide areas over long time periods. These techniques are able to obtain deformation maps, with millimetric precision and kilometric coverages, from the analysis of series of electromagnetic reflectivity images acquired by SAR sensors mounted on satellites (ERS-1, ERS-2, Envisat, Radarsat, TerraSAR-X,etc.) over the study area. Although the data acquisition policies may vary for different sensors, for many zones it is possible to find an historical archive of SAR images acquired by these sensors, thus enabling to study also the Earth's surface evolution at instants previous to a particular event (such as, for instance, an earthquake or a landslide). This supposes another advantage in comparison to techniques based on *in situ* instrumentation, since this is generally installed after the event in question, making it difficult to study triggering factors.

There exist, however, a number of factors which limit the applicability of conventional SAR differential interferometry techniques, such us changes in the atmospheric con-

[1] Synthetic Aperture Radar

ditions at different acquisition moments, spatial decorrelation, due to the different acquisition geometry of the images, or temporal decorrelation, because of changes between acquisitions experienced by the scene itself. With the objective of minimizing the impact of these and other factors, in the late 90's a set of techniques began to sprout, and are encompassed under the term *Persistent Scatterers Interferometry* (PSI). Instead of processing all of the pixels of a scene, this kind of techniques builds a network of pixels whose response is considered as reliable *a priori* under certain quality criteria (pixel candidates, PC).

PSI techniques have experienced a significant development since their first versions, and they have been successfully proven on a great variety of scenarios. Nevertheless, their performance is largely conditioned by the density and real quality of candidate pixels found in the study area. These pixels are usually associated with man-made structures such as buildings, metallic fences, etc. It is important to note that the returned signal measured by the SAR system depends largely on the polarimetric channel it works with. Therefore, structures whose electromagnetic response would be considered of good quality for a given channel, might present an unstable or attenuated response, or even become invisible, for other channels, as a function of their orientation and physical properties. However, PSI techniques have been traditionally formulated and applied to data acquired in a single polarization (generally horizontal or vertical), principally due to the lack of SAR satellites operating in multiple polarizations and acquiring images of the same area at regular intervals.

For its part, SAR polarimetry has a long history in the field of classification and image segmentation (discrimination of urban and rural areas, agricultural crops classification, etc.) as well as in physical parameters inversion (estimation of forests height and biomass, soil moisture, ice thickness, etc.). Once again, given the absence of polarimetric SAR satellites, the use of polarimetric time series had been limited to some campaigns with limited coverage, making use of airborne SAR or ground-based SAR systems. Fortunately, this scenario has changed in the last years with the launch of new and modern SAR satellites enabled with different polarimetric operation modes and capable of acquiring images of a same area with a revisit time (time between acquisitions) reasonably reduced, as they are TerraSAR-X (DLR, German Aerospace Center), ALOS-PALSAR (JAXA, Japanese Aerospace Exploration Agency), Radarsat-2 (CSA, Canadian Space Agency) or the future Sentinel-1 (ESA, European Space Agency) and RCM, Radarsat Constellation Mission (CSA).

This thesis begins motivated by the possibility of finding new ways of exploiting the polarimetric diversity offered by the new SAR sensors in an effective manner. Particularly, we start from the hypothesis that polarimetry can contribute to improve the performance of SAR differential interferometry approaches, and specially PSI techniques, allowing us to detect a larger number of reliable pixels or increasing the quality of the ones previously located.

Once the global motivation has been stated, the specific objectives of this thesis are detailed in the following:

1. Proposal and implementation of DInSAR algorithms that take advantage of the data acquired by polarimetric SAR sensors in an optimal way, paying special attention to

data provided by satellite sensors, given their potential in terms of coverage and operability.

2. Evaluation of proposed algorithms using SAR images acquired in different polarimetric modes, and comparison of achieved results with those obtained using non-polarimetric data.

3. Determination of the ideal polarimetric configuration for the study of urban environments, of first importance because of the aforementioned economical and human risks associated with the deterioration of structures by terrain deformations.

In the present document, the most significant publications fruit of this thesis are compiled, along with a synthesis of the results and conclusions reached. The text has been organised in four sections, plus publications and appendices, constituting this **Introduction** a general presentation of the motivation, objectives and structure of this work.

In section **State of art**, with the aim that this thesis be self-contained, the state of art is addressed, which will also be used to introduce, in a very concise manner, the main concepts and technologies implied.

In section **Results**, the most significant results of this thesis are compiled and commented.

Finally, in section **Conclusions** the main conclusions reached in this thesis are discussed, and future research lines are also suggested.

The text of this document is sustained by the appended articles, which have been published in two of the journals of greatest impact on the remote sensing field: *IEEE Geoscience and Remote Sensing Letters*, and *IEEE Transactions on Geoscience and Remote Sensing*. In addition, a complete list of publications in journals and international conferences generated during the development of this thesis has been included.

2.2 State of the art

AS stated in the introduction, the primary goal of this work has been to improve current remote sensing techniques for the study of Earth's surface deformation, particularly PSI approaches, because of their proven efficacy in urban scenarios. The idea is to adapt these techniques so that they can make use of the polarimetric diversity provided by the latest generation of satellite radar sensors.

This section is designed to serve as an introduction to the technologies related to the topic of this thesis, as well as to help describing the state of the art at the outset of this research work.

2.2.1 SAR remote sensing

Remote sensing can be defined as the measurement of physical properties of a target without an actual contact between target and sensor. Depending on the source of the measured energy, sensors can be classified as either passive sensors, which register the energy coming from an external source (photographic cameras, radiometers, etc.) or active sensors, when they emit energy over the target and capture the reflected signal, as it is the case of RADAR (RAdio Detection And Ranging) systems. Radar sensors emit electromagnetic (EM) pulses and process the echoes returned by the target to measure distances, altitudes, velocities, etc. Given their coverage and near immunity to light and weather conditions, techniques based on Synthetic Aperture Radar (SAR) systems are the usual choice for Earth's deformation monitoring.

SAR systems are coherent radar systems (they preserve phase and amplitude information) meant to generate high resolution complex EM reflectivity images. SAR began to develop during in the 60s as a way to overcome limitations of conventional Real Aperture Radar (RAR) systems. For 2D imaging of Earth's surface, RAR systems sweep the scene with an ideally narrow EM beam. In airborne and satellite systems, a Side-Looking (SL) observation geometry provides *range* (distance to the radar path) sensitivity, whereas in *azimuth* (platform travel direction) resolution is determined by the beam width. In general, the larger the antenna with respect to the pulses wavelength, the narrower the beam. This limits the performance of airborne and satellite RAR imaging systems, since the antenna size will be restricted by weight constraints and deployment difficulties, and smaller wavelengths generally come at the cost of greater atmospheric attenuation and power consumption.

On the other hand, SAR systems use smaller, less directive antennas, that emit EM pulses at regular intervals (the Pulse Repetition Frequency, PRF) while moving along the flight track, also in SL configuration. By combining coherently the echoes received at different positions, and making use of sensor motion information, a larger antenna can be synthesised. Figure 2.1 illustrates the conventional SAR operation mode, the *stripmap* mode, in which fixed pointing direction of the radar along the track is assumed. The strip of surface mapped by the SAR is called *swath*.

Note that, given the side-looking configuration, terrain elevation produces geometric distortions in the SAR image. Most common distortions are *foreshortening*, *layover* and *shadowing*. Foreshortening produces terrain slopes facing the radar to appear contracted, giving the impression that they lean towards the sensor. When the slope angle is equal or even superior to the incidence angle, points on the valley can have larger slant-range distance than the mountain tops, and then foreslope projection becomes reversed and ambiguities appear: different points of valley, slope and mountain top are mapped at the same pixel, which appears brighter. This effect is known as *layover*, and cannot be resolved by geocoding, so these areas will also appear brighter when projecting from radar to geographic coordinates. Finally, slopes away of the radar illumination with angles steeper than the incidence angle produce *shadows* in the SAR image, since there is no echo returning from them.

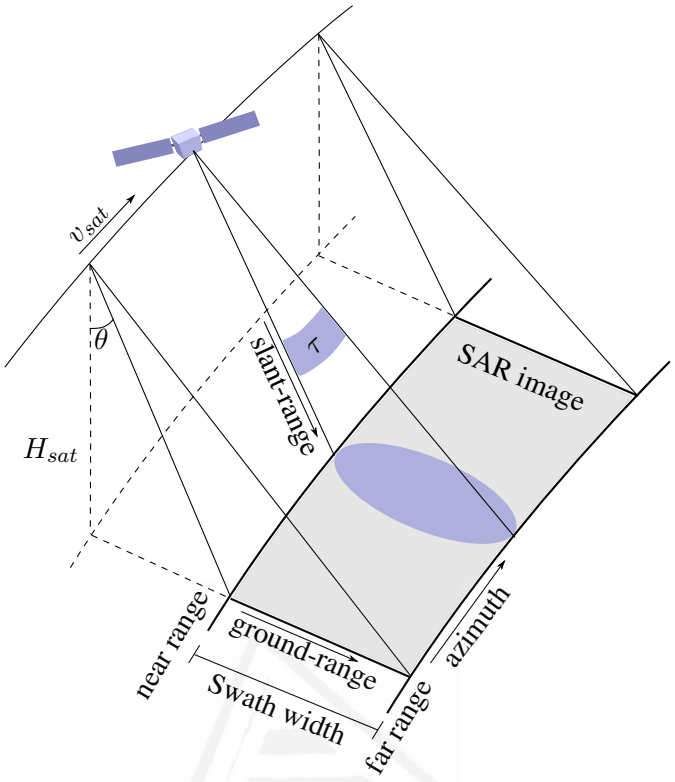

Figure 2.1. SAR acquisition geometry.

Another undesired effect inherent to any SAR system is *speckle*, originated by the coherent combination of the returns from multiple scattering centres inside the resolution cell. These interferences produce a "salt and pepper" noise-like effect that is characteristic of SAR images.

As aforementioned, SAR are coherent radar systems, so they measure both amplitude and phase of the backscattered signal. As a result, they produce complex reflectivity images, usually referred as Single-Look Complex (SLC), where each resolution cell is assigned a complex reflectivity value. The amplitude of the SLC image gives us an idea of the backscattered power. As for the phase component, its value depends on the range distance between the sensor and the target. However, note that this distance is several orders of magnitude greater than the pulses wavelength (several hundred kilometres against few centimetres), so the pulse will complete a large number of phase cycles during its round-trip time. As the exact distance to the target is *a priori* unknown, the total number of cycles cannot be disambiguated. Therefore, no useful information can be obtained from the phase at this point.

Further information on SAR imaging techniques and evolution of SAR systems can be found in [Carrara et al., 1995][Oliver and Quegan, 1998].

2.2.2 SAR Interferometry and Differential Interferometry

SAR Interferometry (InSAR) techniques are born with the objective of measuring relative distances and mapping the topography of an area, by exploiting the phase information of two SAR images acquired from different positions, either by using two antennas (single-pass) or by performing multiple passes (repeat-pass). By combining two SAR acquisitions, similarly to how human vision works, we become sensitive to the angular differences, and topographic information can be extracted from the travelled path difference, related to the interferometric phase. The physical distance between the satellite orbits at the moment of the acquisition is known as spatial baseline, whereas the temporal separation (in case of non-simultaneous acquisitions) is known as temporal baseline.

Interferometric phase can be thought as a mixture of phase contributions, including the topographic term, the deformation term (in case that the scene has changed its position between acquisitions), a term related to changes in atmospheric conditions between acquisitions, and noise. Note that, a this point, the interferometric phase still presents an ambiguity in phase cycles, so its value will be comprised between $-\pi$ and π, which appear as "fringes" in the phase image.

Topography can be extracted from interferometric phase by cancelling the undesired contributions. For instance, the contributions of surface deformation and atmospheric variations can be minimised by reducing the time between acquisitions (repeat time) or by using single-pass interferometry.

Once the topographic term is isolated, the interferometric phase is directly related to the surface height, and the frequency of the phase fringes serves as an indicator of the steepness of the topography. However, in order to provide absolute height values, interferometric phase has yet to go through a disambiguation stage known as "phase unwrapping", that is, modulo 2π phase cycles have to be turned into absolute, continuous phase values so that direct phase-to-height conversion can be applied. Finally, all the height values in radar coordinates (range, azimuth) are re-projected onto geographic coordinates, in a process known as *geocoding*, to generate the final topographic model or DEM (Digital Elevation Model).

InSAR techniques are useful to obtain the topography of large areas from SAR observations. Differential SAR Interferometry (DInSAR) techniques go one step further, allowing us to measure the deformation experienced by the terrain in the lapse of time between acquisitions, provided that the topography of the area is already known or it can be obtained by conventional InSAR.

In other words, the objective of DInSAR techniques is to isolate the term related to the deformation from the rest of contributions to the interferometric phase. Then, the interferometric fringes will be related to the deformation in the line-of-sight direction in the same way they were related to topography in the InSAR case.

The cancellation of the topographic component is a key step in DInSAR processing. There exist different approaches on how to remove the topographic term from the interfero-

metric phases, as described for example in [Mora, 2004]. The scheme used in this work for differential interferograms formation relies on an external DEM to estimate and cancel the topographic phase term.

In addition to the possible DEM inaccuracies, there exist some limiting factors that may degrade the quality of the differential interferogram. We can summarise these limitations in four points:

- **Temporal decorrelation**: Due to the requirement of large temporal baselines (lapse of time between images) for monitoring slow displacements, temporal decorrelation problems may appear, specially in vegetated areas, where backscattering conditions of the scene may vary significantly between acquisitions.

- **Geometric decorrelation**: Changes in the acquisition geometry of the two SLC images entail a relative displacement of their range spectrum. For interferogram formation, only the portion of the spectrum common to both images is usable. The spatial baseline that causes the spectra to not have a common band is called *critical baseline*. As an example, for ERS satellites, with a bandwidth of 18 MHz, the critical baseline is around 1200 m, though in practice much smaller baselines are preferred.

- **Atmospheric artefacts**: Changes in atmospheric conditions may produce phase fringes in the differential interferogram, which present magnitude and spatial features similar to the deformation term, and hence are difficult to separate from the deformation contribution.

- **Phase unwrapping errors**: In most situations, interferograms will be severely affected by noise and atmospheric artefacts, therefore they will require the use of advanced phase unwrapping techniques. However, these techniques are not failproof and, in general, the capability to extract the deformation component from a single differential interferogram is very limited.

Considering all these aspects, we find that only a very reduced subset of the existing SLC images will be suitable to produce useful differential interferograms.

A number of advanced DInSAR techniques have been proposed with the objective of suppressing or mitigating these error sources. These techniques achieve more accurate and robust estimates by combining the information provided by multiple differential interferograms. Instead of processing all of the points of the scene, most advanced DInSAR techniques select only those pixels considered as reliable *a priori* according to certain quality criteria. These approaches are generally encompassed under the term Persistent Scatterers Interferometry (PSI). The optimization of PSI performance by means of polarimetry is the primary focus of this thesis.

Additional information on InSAR and DInSAR can be found in [Hansen, 2001].

2.2.3 Persistent Scatterers Interferometry

Since their conception in the late 90s, Persistent Scatterers Interferometry (PSI) techniques have been used extensively to monitor deformations of the Earth's surface [Ferretti et al., 2000][Ferretti et al., 2001]. PSI techniques exploit the phase information of a stack of interferograms, obtained from a set of SAR images acquired at different dates, to retrieve accurate information of the ground deformation evolution along time. In contrast to conventional differential interferometry methods, PSI techniques select for processing only those pixels that are considered as reliable beforehand (*candidates*), according to certain quality criterion. In urban environments, where it is common to find point-like, deterministic scatterers (called Persistent Scatterers, PS) associated with strong and stable backscattering from man-made structures, the most common quality criterion is the amplitude dispersion index (D_A), used as a proxy to the phase standard deviation [Ferretti et al., 2001]. In natural environments, however, the average coherence $\overline{\gamma}$, is usually preferred as indicator of the phase quality [Berardino et al., 2002][Mora, 2004]. Points selected using this method are usually referred as coherent pixels (CP) and correspond to stable distributed scatterers, rather than point-like ones. Notice that maximum likelihood estimation of interferometric coherences generally requires averaging of neighbouring samples (process usually referred as multi-looking) and, consequently, spatial resolution is degraded in this case.

After this preliminary selection, a spatial network of pixels is then constructed, either by linking each pixel candidate with all its neighbouring candidates within a radius, or by using a triangulation approach (e.g. Delaunay). Then, a model depending on velocity (generally assumed linear at this point) is fitted to the phase differences associated with each link. This way, contribution of terms assumed to be nearly equal for neighbouring pixels, such as the atmospheric term, is canceled or reduced significantly. Those links that do not fit the model to a certain degree of model coherence (cost function) will be removed, and disconnected pixels will be discarded as suitable for processing and hence ignored by subsequent steps of the processing.

The non-linear component of the velocity may then be extracted from the phase residuals (difference between the original phase and the modeled phase) by spatial and temporal filtering, exploiting the different space-time behaviour of random noise, atmosphere and non-linear deformations, as described for instance in [Mora, 2004].

Generally, the greater the density of reliable pixels selected, the more robustly the method will behave. However, an excessive relaxation of the quality criterion in order to increase the number of pixels entails difficulties in the processing, since new error sources appear. Therefore, a trade-off has to be considered when selecting the quality threshold.

A reference book in this area is [Kampes, 2006].

2.2.4 PolSAR and PolInSAR

As a radar system, a SAR emits (transverse) electromagnetic waves and analyses the received echoes in order to measure target features. One of the fundamental properties of such propagating electromagnetic waves is their polarisation state, which can be defined as the geometrical figure described by the tip of the electric field vector on the plane perpendicular to the travelling direction.

Most SAR systems emit linearly polarised waves, that is, the oscillation of the electric field occurs in a single direction (for example, vertical or horizontal polarization) and measure the backscattered signal in the same polarisation direction or "channel" (e.g. transmit vertical and receive vertical or, for short, VV). Similarly, other SAR systems are designed to emit and receive circularly or elliptically polarised waves.

When incident waves excite the target, among other effects, an EM field is re-radiated. Depending on the physical properties of the target, such as its geometry, orientation or conductivity, the polarisation state of the backscattered wave may be different, or even orthogonal, to that of the incident wave. In most cases, the returned wave will consist of a mixture of scattering mechanisms (what it is usually referred as a "partially polarised" wave), that cannot be separated using a single channel system.

Polarimetric SAR (PolSAR) systems were developed with the objective of retrieving additional physical properties of the target, other than its EM reflectivity. To do so, PolSAR systems transmit and receive different combinations of polarisations. Instead of a single complex reflectivity coefficient, a PolSAR system provides a matrix of coefficients for each pixel of the scene, with as much elements as transmit-receive channel combinations. This way of arranging PolSAR data is known as the *Sinclair* or *scattering* matrix, $\mathbf{S}$. Then, for instance, a number of decomposition theorems can be applied to express the data as the contribution of several "canonical" scattering mechanisms (surface or specular reflection, dihedral, random volume, etc.) thus obtaining insight on the physical features of the scene.

A commonly used formalism, which is helpful for the extraction of physical information from the polarimetric description of a scatterer, consists in the construction of the so-called *target vector*, $\mathbf{k}$. The target vector is formed by simply vectorizing the scattering matrix $\mathbf{S}$, which mathematically is performed by projecting the scattering matrix onto a set of orthonormal basis matrices (generally the Pauli spin matrices), as described for instance in [Cloude and Papathanassiou, 1998]. Though different basis can be used for the vectorization, the Pauli set is a common choice because the elements of the resulting vector are closely related to the physics of wave scattering, and allow a better interpretation of the scattering mechanisms. Moreover, by computing the outer product of $\mathbf{k}$ with its conjugate transpose, we obtain the *coherency matrix* $\mathbf{T}$, useful to describe partially polarised targets, when second order statistics come into play.

Much work has been done on target decomposition based on $\mathbf{T}$ matrices. Note that, in dynamically changing environments, it is common that scatterers are not fixed, but subject to spatial and temporal variation. These targets are usually referred as "partial scatterers",

since they are analogous to partially polarised waves. Generally, they can be analysed in a more precise way by considering the scattering from such targets as a stochastic process in space and time. Then, partial scatterers can be described using the second moments of the fluctuations, which will be extracted from the $\mathbf{T}$ matrices [Lee and Pottier, 2009]. An interesting property of $\mathbf{T}$ matrices is that its eigenvector decomposition provides a set of orthonormal projection vectors, associated with different scattering mechanisms within the resolution cell, and the associated eigenvalues give us insight on the contribution of each mechanism to the total backscatter.

Polarimetric SAR Interferometry (PolInSAR) is developed with the aim of separating vertically the phase centres of the different scattering mechanisms within a resolution cell [Cloude and Papathanassiou, 1998]. PolInSAR has a variety of potential applications. For instance, it can be used to estimate the relative distance between the canopy on forests (random volume scattering), and the ground-tree trunk (double-bounce or dihedral mechanism), thus allowing us to measure tree heights or the amount of biomass over wide areas.

In order to generate interferograms from polarimetric data, a target vector ($\mathbf{k}$) can be projected onto a unitary projection vector (ω), resulting in a complex scalar coefficient (μ), which is analogue to single-pol data [Cloude and Papathanassiou, 1998]. Therefore, these coefficients can be combined to form interferograms in a similar way as to conventional InSAR. The projection vectors can be chosen so that the resulting coefficients are related to a particular scattering mechanism, or they may be chosen in a way that interferometric coherence is maximised.

The possibility of optimizing interferometric coherence, and potentially any other desired quality indicator, by modifying the projection vectors, is one of the aspects that will be exploited in this thesis.

A complete review of PolSAR and PolInSAR can be found in [Cloude, 2010] and [Lee and Pottier, 2009].

2.2.5 Polarimetry and Persistent Scatterers Interferometry

The first application of polarimetry to urban PSI was proposed in [Perissin and Ferretti, 2009], where it was made use of Envisat incoherent dual-pol data to recognise target physical features and to classify PS. Another PS classification strategy supported by polarimetry was also presented in [Dheenathayalan and Hanssen, 2011] in the context of building-versus-ground relative movement estimation, using TerraSAR-X coherent dual-pol data.

To further exploit polarimetric diversity at initial PSI processing stages, an algorithm aiming to increase the quality and number of pixels pre-selected for PSI processing was introduced in [Pipia et al., 2009a]. The proposed algorithm consisted in selecting, from the set of polarimetric channels provided by the sensor, the one with maximum average interferometric coherence for each pixel. The algorithm was tested using dual-pol (HH, VV) ground-based

SAR data, achieving a significant improvement in the density of selected CP and demonstrating for the first time the potentials of polarimetry for PSI. This approach, though illustrative, leads only to a suboptimal solution, since it considers only a fraction (discrete projections) of the available polarimetric space. Subsequently, in [Pipia et al., 2009b], a polarimetric coherence optimisation approach was proposed, suitable for zero-baseline, ground-based SAR. This method exploits the fact that this kind of SAR system is not sensitive to topography, as discussed in the attached publication [Navarro-Sanchez et al., 2010], which is not generally the case for satellite SAR systems.

Encouraged by these preliminary works, this thesis has been devoted to the search of effective and efficient techniques for satellite PSI optimisation by means polarimetry, in order to benefit from the full potential of new generation SAR systems.

2.3 Results

THE starting point of the study was the definition of a general framework for the polarimetric optimisation of PSI, based on the maximisation (or minimisation, depending on the case) of the parameters of quality considered for the selection of valid pixels [Navarro-Sanchez et al., 2010]. In order to perform this optimisation, a search is carried out, on a pixel-by-pixel basis, to find the projection or "channel" providing the best results for each point of the scene. Note that the search is not limited to the channels provided by the sensor (e.g. horizontal, vertical and cross-polar), but linear combinations of channels can be obtained in order to cover all the available polarimetric space.

The proposed scheme has the advantage that it can be applied to any known PSI technique, with minimal modifications, as a pre-processing stage. Thus, the PSI processor developed in the University of Alicante in previous projects was adapted to take in the new polarimetric algorithms, in order to assess their performance.

The methods presented in this work have been adapted and tested for the most commonly used criteria of quality: selection of pixels with low amplitude dispersion index (D_A), computed for the whole set of SAR images, and selection by high average coherence ($\overline{\gamma}$), computed for a stack of multi-looked interferograms.

Sensitivity of these parameters to polarimetry was demonstrated in [Navarro-Sanchez et al., 2010] using a series of dual-pol images (horizontal and vertical polarisation) acquired by the German satellite TerraSAR-X over the urban area of Murcia (Spain). Values of D_A as well as $\overline{\gamma}$ were represented as a function of the polarimetric channel (given by a parameterisation of the projection vector, ω) for a set of arbitrary points of the scene, showing significant differences of magnitude for the different channels, specially evident in the case of D_A. Note that, in contrast to coherence, amplitude dispersion is computed for single-look data, that is, there is no averaging between neighbouring pixels. Consequently, polarimetric behaviour of each resolution cell is more likely to be determined by the geometry of single

dominant scatterers, with a well-defined scattering mechanism, instead of being determined by the average features of an extended area.

By selecting, for each pixel, the channel that optimises the quality criterion, it is possible to dramatically increase the number of pixel selected as suitable for processing, with no need to modify the selection thresholds, as shown in [Navarro-Sanchez et al., 2010]. As an example, for a coherence threshold of 0.8, 17.29% of the scene pixels were selected over the study area when considering optimised data (dual-pol), against only 7.64% pixels selected for the VV (vertical transmit-receive) single channel. This signifies more than double the density of selected points, which is a spectacular increase, considering that only an additional measured channel (HH, horizontal transmit-receive) was incorporated to the processing. As expected, the increment is even greater in the case of D_A, due to the higher sensitivity of single-look data to polarimetric features. For instance, considering a typical threshold of 0.25, 30.88% pixels are selected for dual-pol optimised data, against 7.72% for single VV channel, which means more than triple the density of pixel candidates.

It is important to note that, in this approach, we constrain the projection vector ω corresponding to each pixel to be the same for the whole set of images. This can be interpreted as selecting the scattering mechanism that better captures stable polarimetric features of the area covered by the resolution cell. This constraint is necessary for PSI in order to build consistent time series of phases related to deformations. Otherwise we might select, for the same pixel, different scattering mechanisms for different times, corresponding to different phase centres in the resolution cell that may have different heights. As a result, these phase differences over time would be wrongly interpreted as phase changes due to deformation.

First deformation results based on these techniques were obtained by using a set of dual-pol (HH,VV) TerraSAR-X images, showing a significant increase in the density of points and, hence, coverage of the generated maps [Navarro-Sanchez and Lopez-Sanchez, 2012]. Moreover, as a byproduct of the optimisation, it is assessed the ability of the algorithms to provide a classification of the different scattering mechanisms presents on the scene (specular reflection, double bounce, diffusion), in turn associated with different kind of targets (buildings, vegetation, asphalt, etc.). Dominant scattering mechanisms are related to the obtained optimum projection vectors. It is observed that pixels selected as persistent scatterers or coherent points tend to present a dihedral-like mechanism, generally related to ground-building (double bounce) reflections.

In [Navarro-Sanchez and Lopez-Sanchez, 2011], the use of purely polarimetric quality criteria for pixel selection was addressed. These indicators of polarimetric stationarity presented correlation with classical selection criteria, but they provided complementary information on the evolution of the target.

At this point, the proposed algorithms (based on a parameterised, brute-force search) were simple, but computationally costly, therefore their use was limited to data with a maximum of two polarimetric channels. Consequently, effort was put into improving the efficiency of these algorithms, as well as in developing alternative approaches which, taking into account a set of constraints, would offer a superior performance and similar results. The

algorithms were tested using dual-pol data of the city of Murcia (TerraSAR-X) as well as fully polarimetric data (HH, VV, HV and VH) acquired over the city of Barcelona (Radarsat-2). In both cases, retrieved deformation maps show an important increase in coverage with respect to conventional PSI approaches. The improvement is specially obvious for the full-pol dataset, as it was expected, given the wider polarimetric search space [Navarro-Sanchez et al., 2014].

As the latest contribution of this research, in [Navarro-Sanchez and Lopez-Sanchez, 2014] an adaptive spatial filtering scheme is proposed and applied to PSI. The proposed filter is driven by polarimetric statistics estimated in the temporal dimension. The use of temporal statistics to drive the filter, rather than spatial statistics computed from neighbouring samples, implies that spatial resolution can be kept unaltered in those areas which do not benefit from filtering, preserving details as building borders, lampposts and other structures, generally man-made. Therefore, the approach allows to jointly process stable point-like scatterers (PS) and distributed scatterers (DS), i.e., groups of neighbouring pixels sharing similar reflectivity properties that may be considered as part of the same target. For convenience, a quality criterion based on the estimated phase standard deviation is introduced, that can be used for both PS and DS selection, as described in [Navarro-Sanchez and Lopez-Sanchez, 2014].

The use of this pre-processing strategy (which makes use of the available polarimetric information), along with the proposed PSI optimisation algorithms, manages to increase spectacularly the density of deformation results, surpassing by far the results obtained by other techniques for the considered datasets. For filtered TerraSAR-X dual-pol data, area coverage is increased by over 1.5 times w.r.t. unfiltered, polarimetrically optimised data, and 3.7 times w.r.t unfiltered single-pol data. As for filtered Radarsat-2 full-pol data, area coverage is increased by $\times 1.35$ w.r.t. unfiltered, optimised data, and $\times 9.3$ w.r.t unfiltered single-pol data. The combination of adaptive filter and polarimetric optimisation on full-pol data is the configuration that provides the best results.

It is worth mentioning that, given our lack of validation data measured for the study areas by using other methods, the deformation results have been compared qualitatively with those obtained using classical techniques, and with results obtained in other studies found in the literature (e.g. [Herrera et al., 2010][Monserrat et al., 2011]). The maps obtained using the developed polarimetric techniques show similar overall deformation trends for the studied areas, when compared to other approaches, but a clearly superior density of pixels with deformation information.

2.4 Conclusions

THIS research has been devoted to the development of new approaches for surface deformation monitoring, able to exploit efficiently polarimetric SAR data provided by new generation satellite sensors. The benefits of polarimetry to PSI have been assessed: a set of techniques combining PSI and polarimetry have been introduced and evaluated, obtaining

denser and more meaningful deformation maps (w.r.t single-pol), and gaining insight on the most advantageous configurations. With this, the primary objectives of this research have been satisfied.

A general framework for polarimetric PSI has been proposed: first, polarimetric data are transformed to single-channel data by using a set of projection vectors, selected in a way that the quality criterion used for pixel selection is optimised. Then, any PSI technique designed for single-channel data can be applied to the projected data, obtaining a general increase in quality and density of pixels selected and processed.

Following this general scheme, a number of algorithms for the obtainment of the optimum projection vectors have been proposed. All of the presented approaches have proven to increase the coverage of generated deformation maps to some degree with respect to single-pol PSI. In addition, a novel polarimetric adaptive filtering strategy has been introduced, along with a methodology for the joint processing of point-like and distributed scatterers which, in combination with the polarimetric optimisation, produced a maps density increase of nearly $4\times$ for dual-pol data, and over $9\times$ for full-pol data, for the urban scenes considered.

Though the use of fully-polarimetric data is most desirable, dual-pol data has proven able to provide important improvements of maps density, at a substantially lower computational cost. In urban scenarios, such as the ones considered, dihedral-like scattering mechanisms (ground-building reflexions), associated with the Pauli $\mathrm{HH}-\mathrm{VV}$ channel, are the most prone to be selected as reliable. Therefore, the combination of HH and VV polarimetric channels is likely to provide good results, even if fully polarimetric data are not available. However, note that obtaining coherent measures of HH and VV bear the same requirements as full-pol in terms of PRF and reduced swath, since they require multiplexed transmission of horizontal and vertical polarisations. Nevertheless, as demonstrated in [Navarro-Sanchez et al., 2014], a hybrid-pol system emitting circular polarisation and receiving linear H and V would be able to obtain a similar improvement, with none of the aforementioned limitations. Consequently, hybrid-pol would be the preferred option when full-pol data are not available.

Validation of the presented results with ground-truth data is yet to be addressed, and recommended as future work. However, the increase of pixel density will generally contribute to the robustness of PSI approaches, adding redundancy and hence improving the accuracy of the phase estimates.

Behaviour of the proposed techniques may vary for different areas or types of terrain. Particularly, note that the performance and optimum configuration of the proposed adaptive filter depend mainly on the features of the scene under study, as well as the sensor specifications. As a future research line, the performance of the filter on different scenarios as a function of configuration parameters should be carefully revised. Additionally, different hypothesis tests for the discrimination of homogeneous areas must be studied and compared.

Another direct follow-up to this work is the detection, interpretation and processing of multiple stable scattering mechanisms within the same resolution cell, by exploiting the well-known capabilities of polarimetric InSAR. This may enable, for instance, selecting several

persistent scatterers at each pixel, hence increasing the redundancy of the PS network and, potentially, deformation retrieval accuracy.

An additional line of work worth to be addressed is the study of polarimetric quality criteria for pixels selection. This will allow to determine more precisely which pixels are suitable for processing, by taking advantage of the additional information provided by polarimetry, and will pave the way to alternative polarimetric optimisation approaches. Some work on this line has been already carried out [Navarro-Sanchez and Lopez-Sanchez, 2011], anticipating the potential benefits of a thorough research in this area.

CHAPTER 3

Publications

3.1 A Contribution of Polarimetry to Satellite Differential SAR Interferometry: Increasing the Number of Pixel Candidates

A Contribution of Polarimetry to Satellite Differential SAR Interferometry: Increasing the Number of Pixel Candidates

Victor D. Navarro-Sanchez, *Student Member, IEEE*, Juan M. Lopez-Sanchez, *Senior Member, IEEE*, and Fernando Vicente-Guijalba, *Student Member, IEEE*

***Abstract*—This letter presents a general method for increasing the number of pixel candidates, those selected for processing in advanced differential SAR interferometry, by means of the exploitation of the polarimetric information provided by new satellite sensors. The algorithm is formulated for two different criteria of selection: the average coherence over the stack of interferograms and the amplitude dispersion index of the stack of images. Experimental results obtained with dual-pol images of TerraSAR-X over an urban area have demonstrated the expected improvement. The number of pixel candidates for an arbitrary threshold is 60% higher than that for single-pol data when using the average coherence and three times higher when using the dispersion index. The approach has also been compared to a selection based on a set of conventional channels (the copolar linear channels and the first two Pauli ones), showing a slight improvement for coherence selection and an important one for amplitude dispersion selection.**

***Index Terms*—Differential synthetic aperture radar (SAR) interferometry, polarimetry.**

I. Introduction

THERE exist a number of advanced differential synthetic aperture radar (SAR) interferometry (ADInSAR) methods which are widely used to measure deformations of the Earth's surface with high accuracy [1]–[4]. These methods exploit the phase information of interferograms formed from stacks of SAR images, acquired at different dates, to generate maps of the average deformation rate and also temporal evolutions of the ground surface movement. In order to avoid decorrelation effects and other issues in the deformation estimation, all ADInSAR techniques start selecting for processing only those pixels that are considered as *a priori* valid under certain quality criteria. These pixels are generally known as *pixel candidates*. Then, after some steps of the processing, candidates are confirmed as suitable for the applied method or are discarded because they do not actually fit the expected behavior.

Manuscript received July 28, 2009; revised September 15, 2009. Date of publication October 30, 2009; date of current version April 14, 2010. This work was supported in part by the Spanish Ministry of Science and Innovation (MICINN) and in part by EU FEDER under Projects TEC2008-06764-C02-02 and HA2007-0075.

The authors are with the Signals, Systems and Telecommunication Group (SST), DFISTS, EPS, University of Alicante, 03080 Alicante, Spain (e-mail: victor.navarro@ieee.org; juanma-lopez@ieee.org; fernando.vicente@ua.es).

Color versions of one or more of the figures in this paper are available online at http://ieeexplore.ieee.org.

Digital Object Identifier 10.1109/LGRS.2009.2033013

In general, ADInSAR methods need a large number of pixel candidates to work properly. For instance, processing stages, such as phase unwrapping, spatial filtering, interpolation, etc., work more consistently when the density of pixels is high than when pixels are sparsely distributed in the image. However, an excessive relaxation of the quality criteria for increasing the number of candidates entails difficulties in the processing since new error sources appear. Consequently, a tradeoff is always employed for deciding the thresholds of the quality criteria. Signal parameters usually employed as quality criteria for pixel-candidate selection are the *average coherence* for the full set of interferograms [3], [4], where coherence is computed over multilook spatial windows in the interferograms, and the *amplitude dispersion index* [2], computed for the whole stack of single-look complex images and thus preserving full resolution.

To date, all satellites used by ADInSAR approaches (e.g., the ERS-1, ERS-2, Radarsat-1, JERS-1, etc.) have provided images acquired at a single polarimetric channel (HH or VV). With the recent launch of satellite SAR sensors producing images with more than one polarimetric channel (for instance, Radarsat-2, the ALOS-PALSAR, TerraSAR-X, etc.), there exists the potential to exploit this diversity to increase the number of pixel candidates, either by selecting a polarization channel or by combining the available channels in an intelligent way.

This letter is aimed to present a general framework to exploit the polarimetric information available to increase the number of pixel candidates. The proposed approach consists in a search over the available polarimetric space in order to optimize the parameter employed for the selection. Therefore, the approach can be applied to every known selection criteria. This method has been adapted and tested in this letter to the two aforementioned criteria (average coherence and amplitude dispersion index). In this letter, we present the formulation only for the dual-pol case, as the TerraSAR-X images at our disposal, but the extension to fully polarimetric (quad-pol) images is straightforward.

Other alternative techniques for improving the pixel-candidate selection by means of polarimetry have been recently introduced in the context of ADInSAR but applied to data acquired with a ground-based SAR [5], [6]. In the first case, instead of looking for an optimum channel in the whole signal space, they select the best choice from a limited set of conventional channels, e.g., HH and VV [5]. As a result, the number of pixel candidates increases with respect to a single-pol case, but leading to a suboptimal solution. In contrast, a

polarimetric optimization is carried out for each pixel and also for each interferogram in [6]. Consequently, the selected polarimetric channel changes from interferogram to interferogram. This degree of freedom is available because the system works in a zero baseline configuration, and hence, there is no topographic component in the phase. Note that, in general, different polarimetric channels correspond to different phase centers in the pixel. Therefore, in a nonzero baseline configuration, as the one approached in this letter, a change in the phase center from interferogram to interferogram would entail a (topographic) phase change that would contaminate the time series of interferometric phases due to deformation. Hence, the optimization proposed in this letter will deliver a single polarimetric channel for the whole stack of interferograms.

This letter is organized as follows. Section II presents the general framework for the selection of polarimetric channels in order to form the interferograms. The set of images used for the experimental validation is introduced in Section III. Then, Sections IV and V describe the procedure to optimize the selection of pixels when considering the mean coherence and the amplitude dispersion as criteria, respectively. Both approaches are also tested, and the obtained results are commented. Finally, the main conclusions are summarized in Section VI.

II. Formulation

A general formulation for polarimetric SAR interferometry, also known as vector interferometry, was already proposed in [7], considering quad-pol SAR data. For each resolution element, a scattering vector (or *target vector*) $\underline{k}$ is obtained as a vectorization of its 2×2 scattering matrix $[S]$. Although a different basis can be used for the vectorization, the Pauli basis is a common choice because the elements of the resulting vector exhibit a clear physical meaning.

In the case of dual-pol SAR systems, we only have reflectivity information from two combinations of transmit/receive polarizations. If we consider no data from cross-polar channels, we must use a reduced version of $\underline{k}$, defined as

$$\underline{k} = \frac{1}{\sqrt{2}}[S_{\mathrm{HH}} + S_{\mathrm{VV}}, S_{\mathrm{HH}} - S_{\mathrm{VV}}]^{\mathrm{T}} \tag{1}$$

where $^{\mathrm{T}}$ means transposition, S_{HH} and S_{VV} stand for the horizontal and vertical copolar channels, respectively, and the Pauli basis has been used. We assume that HH and VV are measured coherently, i.e., their phases are properly acquired and calibrated to the same reference.

Although the lack of cross-polar information may constitute a drawback because the full polarimetric space cannot be synthesized, it is known that, for most natural targets, the magnitude of the cross-polar measurements are one order of magnitude smaller than those of the copolar channels. Hence, they may suffer more degradation due to noise, which, in turn, might be increased through the optimization process. Cross-polar contributions, however, become more significant for urban areas, particularly when single-look images are processed (as in the amplitude dispersion selection) because of the presence of single dominant targets at each resolution cell. Therefore, the decision on whether to include cross-polar channels, if available, will depend on the technique to be applied and the target area itself.

Fig. 1. Composite RGB image of the area under study in Murcia (Spain) formed by the average intensities. Channels: R = HH, G = VV, and B = HH − VV.

In order to generate an interferogram, each target vector $\underline{k}$ can be projected onto a unitary complex vector $\underline{\omega}$, resulting in a scattering coefficient μ defined as $\mu = \underline{\omega}^{*\mathrm{T}}\underline{k}$ [7]. The scattering coefficient μ is a scalar complex value, obtained as a linear combination of the elements of $\underline{k}$. As a complex value, it is analogous to what we could get from a single-channel SAR system for a resolution element. Thus, we can make use of all interferometry techniques developed for single-pol data, including ADInSAR, by applying them to μ.

At this stage, the issue is how to choose the projection vector $\underline{\omega}$ for each pixel of the SAR images or interferograms, so that we get better results than just considering one polarization channel. In order to solve the problem more easily, one can parameterize the projection vector in a way that guarantees its unitarity, $|\underline{\omega}| = 1$, and ensures that all the possible unambiguous values of $\underline{\omega}$ are taken into account

$$\underline{\omega} = \left[\cos(\alpha), \sin(\alpha)e^{j\psi}\right]^{\mathrm{T}}, \qquad \begin{cases} 0 \leqslant \alpha \leqslant \pi/2 \\ -\pi \leqslant \psi < \pi. \end{cases} \tag{2}$$

Note that (2) is a particular case, specific for dual-pol images, of the parameterization presented in [7]. With this expression, the problem is reduced to finding two real values, i.e., α and ψ, whose range is finite and known, to optimize the selection criterion.

III. Data Set

A set of 12 dual-pol images acquired by TerraSAR-X in 2009, from February 19 to July 1, over the urban area of Murcia (Spain) has been used to test the proposed algorithms. All images have been acquired at HH and VV channels, with a mean incidence angle of 37.8°. Azimuth and slant-range resolutions are 6.6 and 1.17 m, respectively, whereas pixel dimensions are 2.44 and 0.91 m, respectively. Therefore, the resulting oversampling factors are 2.7 and 1.28 in azimuth and range, respectively.

The processing has been applied over a part of the image with 2000×2000 pixels. A color composite formed by the average intensities is shown in Fig. 1. The different colors in the composite image provide an insight about the information content of polarimetry. The city is mostly located in the center of the image, showing different dominant channels at different parts, whereas the outer part, which corresponds to rural areas, is mostly dominated by the VV channel.

IV. Selection Based on Average Coherence

A. Algorithm

The interferometric coherence γ for the scalar case can be computed as

$$\gamma = \frac{\langle s_1 s_2^* \rangle}{\sqrt{\langle s_1 s_1^* \rangle \langle s_2 s_2^* \rangle}}, \qquad 0 \leq |\gamma| \leq 1 \tag{3}$$

where s_1 and s_2 are the scattering coefficients for the same resolution element, corresponding to two images. The module of the interferometric coherence $|\gamma|$, usually named as *coherence*, is a measure of the phase noise of the interferogram, while $\arg(\gamma)$ is the resulting interferometric phase. The $\langle \cdot \rangle$ brackets denote a spatial averaging employed to estimate the interferometric coherence in substitution of the statistical *expected value* operator.

Since a high coherence is an indicator of good quality phase, there are ADInSAR methods (e.g., [3] and [4]) which directly use the coherences of the set of interferograms in order to establish the selection criterion for the pixel candidates. The most simple way to do it is by means of the average coherence $\overline{|\gamma|}$, computed for a stack of K interferograms as

$$\overline{|\gamma|} = \frac{1}{K} \sum_{k=1}^{K} |\gamma_k| \tag{4}$$

where subscript k denotes the kth interferogram and $k = 1, 2, \ldots, K$. For each interferogram, a different pair of images is taken from a total set of N images. After computing the average coherence for each pixel, those pixels with a value above a certain threshold are selected as pixel candidates for further processing.

Considering the vector case, we just have to use μ instead of s in (3). Then, as already justified in Section I, constraining $\underline{\omega}$ to be the same for both images, we obtain the following expression of the coherence of interferogram k [8]:

$$\gamma_k = \frac{\underline{\omega}^{*\mathrm{T}} [\Omega_{12}] \underline{\omega}}{\sqrt{\underline{\omega}^{*\mathrm{T}} [T_{11}] \underline{\omega}} \sqrt{\underline{\omega}^{*\mathrm{T}} [T_{22}] \underline{\omega}}} \tag{5}$$

where $[T_{11}]$, $[T_{22}]$, and $[\Omega_{12}]$ are the 2×2 versions of the 3×3 homonymous matrices defined in [7] and computed for the pair of images of the kth interferogram.

The optimization algorithm proposed here consists in searching the unitary vector $\underline{\omega}$ that maximizes the average coherence (4). Considering the parameterization of $\underline{\omega}(\alpha, \psi)$ given by (2), we only need to find the best values of α and ψ for each pixel.

The multibaseline coherence optimization problem in (4) was solved analytically in [9] using a generalized eigenvalue problem. That analytical solution is more efficient than the numerical search proposed here, particularly when working with quad-pol data since it leads to extra parameters in the search and, hence, to a high computational cost. From the two alternative solutions proposed in [9], named multiple scattering mechanism and equal scattering mechanism (ESM), only the ESM constrains $\underline{\omega}$ to be the same for the whole stack of interferograms as it is imposed here. This constraint is necessary for ADInSAR in order to build consistent time series of phases related to deformations. Otherwise, there would appear many different phases at a single date in the temporal evolution of one pixel's phase, corresponding to different scattering mechanisms chosen for the interferograms formed by the image of that date. Moreover, selecting the same $\underline{\omega}$ for the whole set of interferograms can be interpreted as selecting the most stable or coherent scattering mechanism over time.

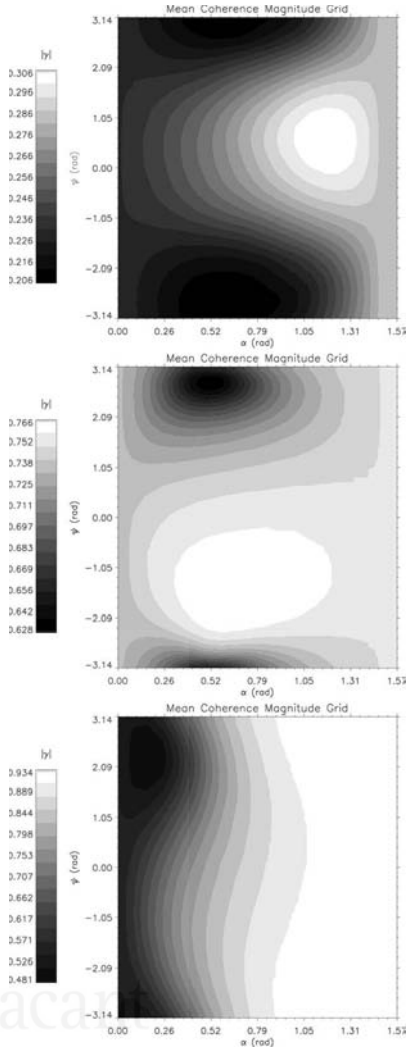

Fig. 2. Values of average coherence $\overline{|\gamma|}$ obtained for three randomly located pixels as a function of α and ψ (resolution $= 5°$).

B. Test

Fig. 2 shows the possible values of $\overline{|\gamma|}$ as a function of α and ψ for three pixels randomly located in the study area. A multilook of 15×15 pixels has been used for coherence computation, which corresponds to an effective number of looks of 65 (see oversampling factors in Section III). In this test, we have generated 66 interferograms, which is the maximum number from the available images. Note that the function is smooth enough for numerical methods to converge easily to its maximum. Each pixel exhibits a different dynamic range (difference between the worst and the best channel) of the average coherence, being above 0.5 in some cases. As expected, it is not possible for all pixels to obtain high coherences despite the use of the polarimetric information, but for many of them, there exists a real improvement when it is exploited.

For comparison purposes, Fig. 3 shows the histograms of $\overline{|\gamma|}$ obtained for different polarimetric channels and for the optimum projection, computed for all pixels of the image. For

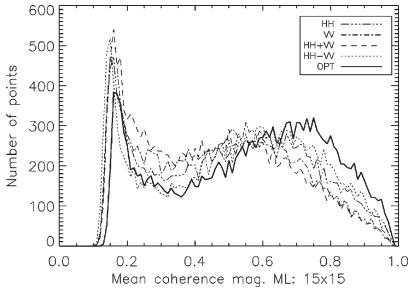

Fig. 3. Histograms of $\overline{|\gamma|}$ for channels HH, VV, HH + VV, HH − VV, and optimum.

TABLE I
PERCENTAGE OF PIXEL CANDIDATES SELECTED FOR EACH CHANNEL, CONSIDERING DIFFERENT $\overline{|\gamma|}$ THRESHOLDS

$\overline{\lvert\gamma\rvert}$ threshold	HH	VV	HH+VV	HH−VV	HH∪VV∪HH+VV∪HH−VV	Optimum
0.6	37.64%	31.09%	28.57%	41.74%	47.39%	49.59%
0.7	22.87%	17.63%	16.27%	26.03%	31.37%	33.72%
0.8	10.85%	7.64%	7.37%	12.45%	15.66%	17.29%
0.9	3.13%	2.02%	2.02%	3.54%	4.78%	5.35%

the optimum channel, about 50% of the pixels show values of $\overline{|\gamma|}$ above 0.6, while for the copolar and the Pauli channels, the number of points above that threshold is comprised between 30% and 40%.

To illustrate the application of this approach to ADInSAR, Table I presents the percentages of selected candidates from the total number of pixels, according to different thresholds, when the following channels are considered: HH, VV, HH + VV, and HH − VV. The column labeled as HH ∪ VV ∪ HH + VV ∪ HH − VV corresponds to the algorithm proposed in [5] but applied to both linear copolar channels and the first two Pauli channels. The term ∪ denotes the *union* operator, in the sense of using the best from the set formed by all the channels considered. From Table I, it is interesting to mention that the second Pauli channel (HH − VV) is the best of the conventional channels, overcoming the performance of HH and VV. This channel corresponds to even bounces of the radar signal, which are originated at many dihedrals present in an urban area. The algorithm proposed in this letter increases importantly (about 60% for each threshold) the number of selected pixels when compared to single-pol interferometry. Finally, note that the algorithm proposed in [5], when applied to the mentioned four channels, is only slightly worse (about 10%) than the optimum one. That method is computationally faster and can be sufficient, depending on the application and the observed area.

V. SELECTION BASED ON AMPLITUDE DISPERSION

A. Algorithm

Let us first consider the single-pol case. A single data point consists of a complex scalar signal s of magnitude $a = |s|$. Considering a stack of corregistered SAR images, the amplitude dispersion index D_A is defined as [2]

$$D_A = \frac{\sigma_a}{\bar{a}} = \frac{1}{\overline{|s|}\sqrt{N}} \sqrt{\sum_{i=1}^{N} \left(|s_i| - \overline{|s|}\right)^2} \tag{6}$$

where σ_a is the amplitude standard deviation, $\bar{a} = \overline{|s|}$ is the mean amplitude, N is the number of images, and s_i is the scattering coefficient of the pixel for the image i. As justified in [2], low values of D_A are good estimates of the phase standard deviation σ_ϕ; therefore, this parameter is a suitable criteria for pixel-candidate selection.

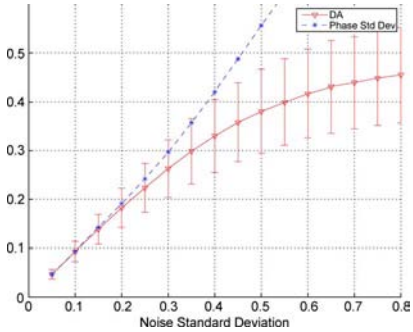

Fig. 4. Comparison of the amplitude dispersion index D_A and the phase standard deviation as a function of noise, computed with a numerical simulation performed in the same way as in [2, Fig. 1], but with 12 images instead of 34.

In the polarimetric case, we replace scattering coefficient s by $\mu = \underline{\omega}^{*\mathrm{T}}\underline{k}$, yielding

$$D_A = \frac{\sigma_a}{\bar{a}} = \frac{1}{\overline{|\underline{\omega}^{*\mathrm{T}}\underline{k}|}\sqrt{N}} \sqrt{\sum_{i=1}^{N} \left(|\underline{\omega}^{*\mathrm{T}}\underline{k}_i| - \overline{|\underline{\omega}^{*\mathrm{T}}\underline{k}|}\right)^2}. \tag{7}$$

In this case, one can search the unitary vector $\underline{\omega}$ (i.e., the best values of α and ψ) that minimizes D_A for each pixel.

B. Test

It is important to mention that the error in the estimation of D_A becomes large when the number of available images is small; therefore, it is recommended to employ a minimum of 30 images. Since we dispose of only 12 images, the resulting standard deviation of D_A is larger than in the case of 34 images (see error bars in Fig. 4 compared with [2, Fig. 1]). Therefore, the threshold for candidate selection should be more restrictive than for more available images.

Fig. 5 shows the values of D_A as a function of α and ψ for three pixels randomly located in the study area. As well as for the average coherence, the function is smooth enough for numerical methods to converge easily to its minimum. We can observe the high dependence on the polarization of D_A, even greater than for the average coherence. Notice that this method uses single-look data; therefore, there is no spatial averaging with neighbor pixels. Therefore, polarimetric response is more likely to be defined by the orientation and shape of single dominant scatterers inside each resolution cell, instead of being defined by the average features of an extended area. As we can see in the top plot, considering the optimum channel can lead to an improvement (a decrease) of D_A of around 0.6.

Fig. 6 shows the histograms of D_A obtained for HH and VV channels, the Pauli channels, and the optimum channel. In this case, there is a dramatic improvement in amplitude stability when we consider the optimum channel, in contrast to any of the conventional channels. Finally, Table II shows a comparison of the number of candidates selected for different polarization channels and D_A thresholds. Notice that considering the optimum projection allows us to lower the D_A threshold to 0.1 and still obtain a reasonable density of

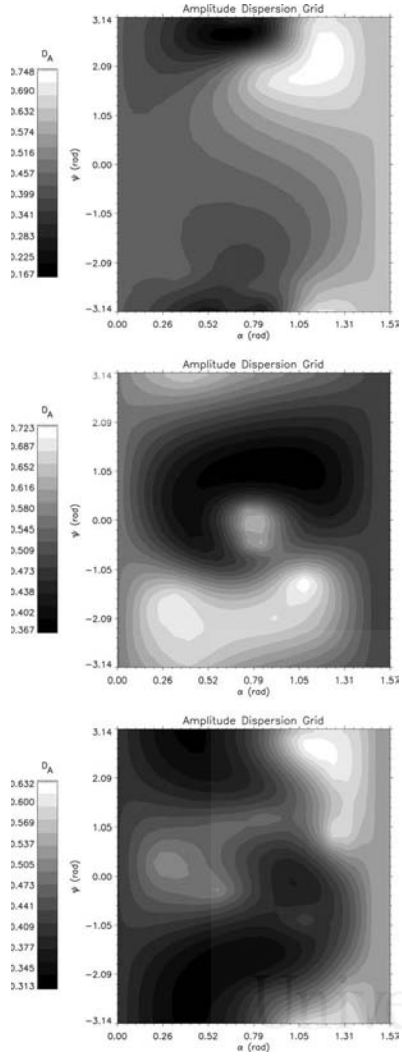

Fig. 5. Values of amplitude dispersion index D_A obtained for three randomly located pixels as a function of α and ψ (resolution $= 5^\circ$).

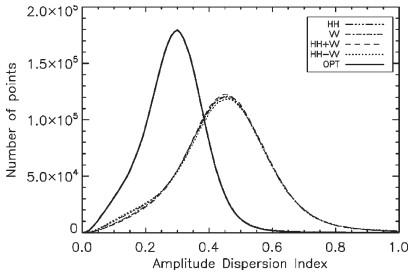

Fig. 6. Histograms of D_A for channels HH, VV, HH + VV, HH − VV, and optimum.

pixels, getting more than three times the number of candidates provided by single-pol data. In this case, our approach provides results about 60% better than those in [5] (column labeled as HH ∪ VV ∪ HH + VV ∪ HH − VV) in terms of number of pixels, as a consequence of the mentioned stronger sensitivity of single-look data to polarimetry.

VI. Conclusion

In this letter, we have presented a general method for increasing the number of selected pixel candidates in ADInSAR by properly using the polarimetric information provided by new satellite sensors. The algorithm has been applied to selections based on the average coherence over the set of interferograms and on the amplitude dispersion index of the stack of images, but it can be easily extended to any other criteria. The approach has been tested with dual-pol images of TerraSAR-X over an urban area, showing a clear improvement with respect to single-pol data in both cases in terms of number of pixel candidates. The improvement is more important for the amplitude dispersion criterion, since single-look data are more sensitive to polarization features. As for the average coherence criterion, a simpler suboptimal algorithm based on choosing among the linear and the Pauli channels offers a solution at a low computational cost that is only slightly worse than the optimization; therefore, it may be sufficient for most applications.

The results presented in this letter need to be confirmed in the future with more images, particularly concerning the estimation of the amplitude dispersion index, as soon as they are available. In addition, a quad-pol extension of this method could be applied to Radarsat-2 data. Finally, ADInSAR approaches have to be applied to the selected candidates to confirm their suitability for the whole processing, not only for the initial selection.

TABLE II
Percentage of Pixel Candidates Selected for Each Channel, Considering Different D_A Thresholds

D_A threshold	HH	VV	HH+VV	HH−VV	HH∪VV∪HH+VV∪HH−VV	Optimum
0.3	14.07%	13.14%	12.64%	14.42%	27.87%	51.59%
0.25	8.68%	7.72%	7.35%	9.08%	16.76%	30.88%
0.2	4.99%	4.21%	3.95%	5.33%	9.55%	16.34%
0.15	2.43%	1.91%	1.80%	2.64%	4.68%	7.70%
0.1	0.80%	0.59%	0.56%	0.88%	1.58%	2.71%

Acknowledgment

All TerraSAR-X images have been provided by DLR in the framework of Project GEO0389.

References

[1] A. Ferretti, C. Prati, and F. Rocca, "Nonlinear subsidence rate estimation using permanent scatterers in differential SAR interferometry," *IEEE Trans. Geosci. Remote Sens.*, vol. 38, no. 5, pp. 2202–2212, Sep. 2000.

[2] A. Ferretti, C. Prati, and F. Rocca, "Permanent scatterers in SAR interferometry," *IEEE Trans. Geosci. Remote Sens.*, vol. 39, no. 1, pp. 8–20, Jan. 2001.

[3] P. Berardino, G. Fornaro, R. Lanari, and E. Sansosti, "A new algorithm for surface deformation monitoring based on small baseline differential SAR interferograms," *IEEE Trans. Geosci. Remote Sens.*, vol. 40, no. 11, pp. 2375–2383, Nov. 2002.

[4] O. Mora, J. J. Mallorquí, and A. Broquetas, "Linear and nonlinear terrain deformation maps from a reduced subset of interferometric SAR images," *IEEE Trans. Geosci. Remote Sens.*, vol. 41, no. 10, pp. 2243–2253, Nov. 2003.

[5] L. Pipia, X. Fabregas, A. Aguasca, C. López-Martínez, S. Duque, J. J. Mallorquí, and J. Marturià, "Polarimetric differential SAR interferometry: First results with ground-based measurements," *IEEE Geosci. Remote Sens. Lett.*, vol. 6, no. 1, pp. 167–171, Jan. 2009.

[6] L. Pipia, X. Fabregas, A. Aguasca, C. López-Martínez, and J. J. Mallorquí, "Polarimetric coherence optimization for interferometric differential applications," in *Proc. IGARSS*, Cape Town, South Africa, Jul. 2009.

[7] S. R. Cloude and K. P. Papathanassiou, "Polarimetric SAR interferometry," *IEEE Trans. Geosci. Remote Sens.*, vol. 36, no. 5, pp. 1551–1565, Sep. 1998.

[8] E. Colin, C. Titin-Schnaider, and W. Tabbara, "An interferometric coherence optimization method in radar polarimetry for high-resolution imagery," *IEEE Trans. Geosci. Remote Sens.*, vol. 44, no. 1, pp. 167–175, Jan. 2006.

[9] M. Neumann, L. Ferro-Famil, and A. Reigber, "Multibaseline polarimetric SAR interferometry coherence optimization," *IEEE Geosci. Remote Sens. Lett.*, vol. 5, no. 1, pp. 93–97, Jan. 2008.

3.2 Improvement of Persistent-Scatterer Interferometry Performance by Means of a Polarimetric Optimization

Improvement of Persistent-Scatterer Interferometry Performance by Means of a Polarimetric Optimization

Victor D. Navarro-Sanchez, *Student Member, IEEE*, and Juan M. Lopez-Sanchez, *Senior Member, IEEE*

***Abstract*—This letter is aimed at presenting results confirming the contribution of polarimetry to improve the performance of persistent-scatterer interferometry. The improvement is provided by the identification of more pixels with good phase quality, under criteria commonly employed in this context, after a search in the available polarimetric space. The ground deformation results obtained with a series of 41 dual-polarization images acquired by TerraSAR-X over the metropolitan area of Murcia, Spain, have been used to illustrate this approach.**

***Index Terms*—Persistent scatterers, polarimetry, subsidence, synthetic aperture radar (SAR) interferometry.**

I. Introduction

PERSISTENT-SCATTERER interferometry (PSI) techniques are a powerful tool to measure ground deformation evolution over wide areas. In all cases, they are based on analyzing the phases of time series of interferograms generated from pairs of satellite synthetic aperture radar (SAR) images. Before the analysis of the phases, they select for processing only those pixels that are considered as *a priori* reliable under certain quality criteria, namely, persistent-scatterer candidates (PSCs). PSCs have to be confirmed as suitable for processing in subsequent steps of the processing or otherwise be discarded.

PSI techniques have been traditionally applied to single-polarization data, mainly due to the lack of satellite sensors operating in multiple polarizations. The scenario has changed recently with the launch of satellite sensors with polarimetric capabilities, such as TerraSAR-X, Radarsat-2, ALOS-PALSAR, and more that are to come in the next few years, like European Space Agency's Sentinel-1. This encourages the design of new PSI algorithms that can benefit from polarimetric diversity.

In [1], we proposed a general framework for using polarimetry to improve PSI performance, which allowed us to optimize the parameter chosen as quality criterion, thus increasing the total number of PSCs selected. The approach was tested using a set of only 12 TerraSAR-X dual-polarization images (HH and VV) acquired over the metropolitan area of Murcia, Spain, for the two most commonly used criteria of selection: amplitude dispersion index [2], computed for the whole set of SAR images, and average interferometric coherence [3], [4] computed for a stack of multilooked interferograms. Results showed a significant improvement in terms of the number of PSCs selected, specially important for the amplitude dispersion criterion, since single-look data are more sensitive to polarimetric features of dominant scatterers within the resolution cell.

In this letter, we confirm the suitability of the optimization approach for providing valid and improved deformation results, i.e., we have applied the whole PSI processing chain to optimized data using a larger stack of images. In addition, a study of the polarimetric features of the observed scenario is carried out to assess the benefits of exploiting polarimetry for PSI and to identify the kind of scattering mechanisms that are more likely to be selected as PSCs, which would help us to develop more efficient algorithms for PSI. Note that PSC characterization using polarimetric data was also dealt with in [5] using Envisat alternating polarization acquisitions.

This letter is organized as follows. Section II describes the input data set used to test the proposed approach. PSC selection results are described in Section III, along with a polarimetric study of the PSCs and final deformation results for both single-polarization and optimized data. Finally, main conclusions are summarized in Section IV.

II. Data Set

Input data consist in a set of 41 coherent dual-polarization TerraSAR-X images (HH and VV) of the city of Murcia, Spain. The images were acquired in the period February 19, 2009, to May 27, 2010, with a mean incidence angle of 37.8°. Azimuth and slant-range resolutions are 6.6 and 1.17 m, whereas pixel dimensions are 2.44 and 0.91 m, respectively. Therefore, the resulting oversampling factors are 2.7 and 1.28 in azimuth and range, respectively. The processing has been applied over a 2000×2000 portion of the images, centered in the urban area of Murcia. Fig. 1 shows an amplitude image of the selected scene. We have also selected two subscenes of 400×400 pixels corresponding to rural and urban areas, to compare the behavior of the algorithms in different environments.

Manuscript received June 14, 2011; revised October 14, 2011; accepted November 10, 2011. Date of publication December 30, 2011; date of current version May 7, 2012. This work was supported by the Spanish Ministry of Science and Innovation (MICINN) under Projects TEC2008-06764-C02-02 and TEC2011-28201-C02-02 and under Grant PR2009-0364 of the National Program of Human Resources Movability.

The authors are with the Signals, Systems and Telecommunication Group, University of Alicante, 03080 Alicante, Spain (e-mail: victor.navarro@ieee.org; juanma-lopez@ieee.org).

Color versions of one or more of the figures in this paper are available online at http://ieeexplore.ieee.org.

Digital Object Identifier 10.1109/LGRS.2011.2176715

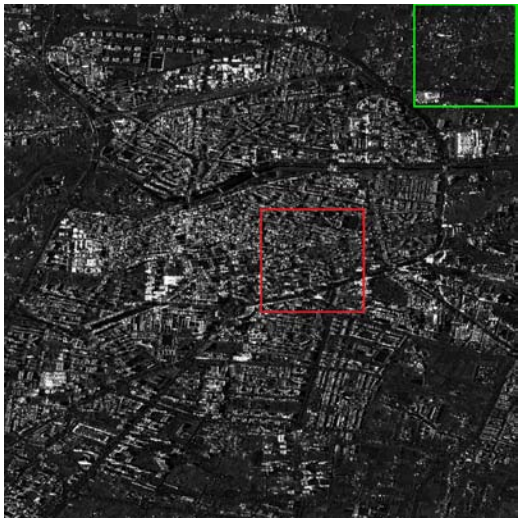

Fig. 1. Amplitude image of the scene employed in the tests (VV channel). (Green square) Rural subscene. (Red square) Urban subscene.

TABLE I
RELATIONSHIP BETWEEN THE VALUES OF $[\alpha, \psi]$ AND DIFFERENT SCATTERING MECHANISMS, FOR THE PAULI BASIS PROJECTION

Surface (odd bounces)	$\alpha = 0;$	$\psi = [-\pi \cdots \pi]$
Linear dipole (vertical)	$\alpha = \pi/4;$	$\psi = \pm\pi$
Linear dipole (horizontal)	$\alpha = \pi/4;$	$\psi = 0$
Dihedral (even bounces)	$\alpha = \pi/2;$	$\psi = [-\pi \cdots \pi]$

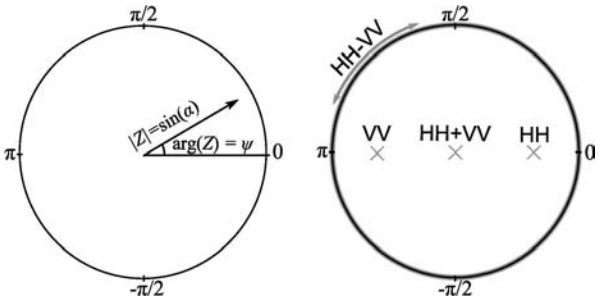

Fig. 2. Interpretation of polar plots. Each pair $[\alpha, \psi]$, as defined in (2), corresponds to the projection of the scattering vector k onto a different polarimetric channel. (Right) Location of the conventional lexicographic (HH and VV) and Pauli (HH + VV and HH − VV) channels on the polar plots.

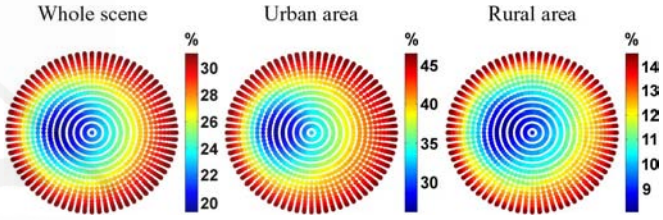

Fig. 3. Density of PSCs (expressed in percent) selected for each polarimetric channel, considering the $\overline{|\gamma|}$ criterion with a 0.7 threshold.

For comparison purposes, we have also performed the selection of pixel candidates for a different set of 41 single-polarization TerraSAR-X images, acquired at VV channel, with a mean incidence angle of 35.3°, from February 1, 2009, to May 20, 2010. These images have azimuth and slant-range resolutions of 3.0 and 1.17 m, with pixel spacings of 1.89 and 0.91 m, respectively. We have selected a crop of 2582 × 2000 corresponding approximately to the same area considered for the dual-polarization images. Subscenes of urban and rural areas have been selected too, with a size of 520 × 400 pixels.

III. RESULTS

A. Selection Based on Average Coherence

The average-coherence optimization proposed in [1] for dual-polarization data consists in finding, for each pixel, the projection vector $|\underline{\omega}|$ that maximizes the following expression:

$$\overline{|\gamma|} = \frac{1}{K}\sum_{k=1}^{K}|\gamma_k|, \qquad \gamma_k = \frac{\underline{\omega}^{\dagger}[\Omega_{12}]\underline{\omega}}{\sqrt{\underline{\omega}^{\dagger}[T_{11}]\underline{\omega}}\sqrt{\underline{\omega}^{\dagger}[T_{22}]\underline{\omega}}} \tag{1}$$

where subscript k denotes the kth interferogram, † stands for conjugate transpose, and $[T_{11}]$, $[T_{22}]$, and $[\Omega_{12}]$ are the 2 × 2 versions of the 3 × 3 homonymous matrices defined in [6]. $\underline{\omega}$ can be parameterized in a way that guarantees its unitarity and ensures that all its possible unambiguous values are taken into account

$$\underline{\omega} = \begin{bmatrix} \cos(\alpha) \\ \sin(\alpha)e^{j\psi} \end{bmatrix}, \qquad \begin{cases} 0 \leqslant \alpha \leqslant \pi/2 \\ -\pi \leqslant \psi < \pi. \end{cases} \tag{2}$$

Coherence computation is carried out over multilook data. Generally, larger multilook factors provide better estimates of the coherence at the cost of a lower spatial resolution. As a tradeoff, a multilook factor of 7 × 7 has been used, which corresponds to an effective number of looks (ENL) of ≈14 (see oversampling factors in Section II). This ENL is expected to provide coherence estimates with standard deviations of below 0.1 for coherence values above 0.7 and below 0.05 for coherence values above 0.9, according to the expressions derived in [7]. From all the possible pairs of images, we have established a 100-m limit for the perpendicular baseline and 100 days for the temporal baseline, resulting in the generation of 167 interferograms from the 41 dual-polarization images.

First, in order to analyze the influence of the polarimetric channel on the average coherence, we have carried out independent PSC selections using all possible projection vectors $\underline{\omega}(\alpha, \psi)$. In practice, we have obtained the projection vector by varying the parameters α and ψ in their valid range with a 5° step. Since the interpretation of $[\alpha, \psi]$ depends on the projection basis of $\underline{k}$, we include in Table I the relationship of canonical scattering mechanisms with values of $[\alpha, \psi]$ for the Pauli basis.

The total number of PSCs selected for each combination of α and ψ will be represented for analysis. In order to ease interpretation of these results, we use a polar plot where each result is located in a position given by Z, defined as $|Z| = \sin(\alpha)$, $\arg(Z) = \psi$. This representation corresponds to a projection of the hemisphere defined by α and ψ. Fig. 2 shows the position of some canonical channels in the plots. Selection results are shown in Fig. 3, for the whole scene and also for urban and rural subscenes, as defined in Section II. Notice that, for this particular analysis, we do not vary the polarimetric channel in a pixel basis but we use the same channel for the whole scene at the selection stage. The influence of the polarimetric channel chosen is evident, with a difference of about 50% more PSCs selected when comparing the best and the worst channels, for all of the scenes and subscenes considered. As a general

TABLE II
PSCs SELECTED FOR DIFFERENT POLARIMETRIC CHANNELS AND THE OPTIMIZED RESULT, CONSIDERING A $|\overline{\gamma}|$ THRESHOLD OF 0.7

	HH	VV	HH+VV	HH−VV	Optimum
Whole scene	28.29%	24.07%	21.79%	31.00%	38.57%
Urban area	41.47%	34.02%	32.20%	45.23%	55.82%
Rural area	15.15%	10.04%	8.99%	14.25%	18.20%

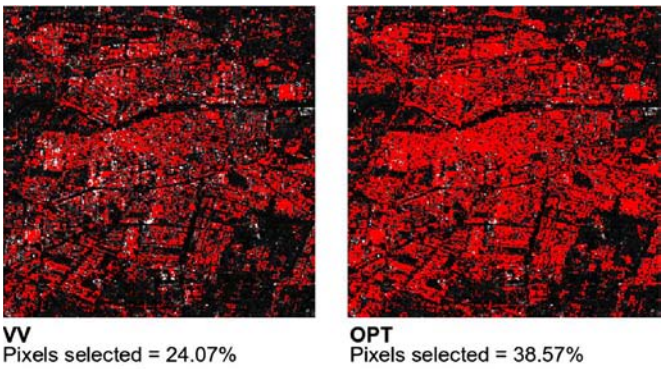

(a) $|\overline{\gamma}|$ threshold = 0.7, ML = 7×7, 167 interferograms.

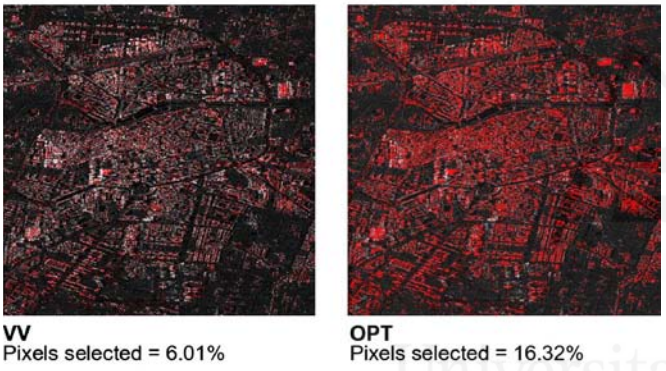

(b) D_A threshold = 0.3, single-look, 41 images.

Fig. 4. Comparison of pixel candidates selected for the VV and optimum channels, for (a) $|\overline{\gamma}|$ criterion and (b) D_A criterion. (a) $|\overline{\gamma}|$ $threshold = 0.7$; $ML = 7 \times 7$; 167 interferograms. (b) D_A $threshold = 0.3$; single look; 41 images.

trend, the number of PSCs selected raises as we move toward dihedral-like mechanisms, so a first approach to improve PSI performance may consist in selecting the HH − VV channel for processing, instead of the copolar ones, VV or HH. However, choosing the same channel for the whole scene still leads to a suboptimal solution, as will be shown later.

In the second place, the proposed optimization is applied in order to find the $\underline{\omega}$ vectors that maximize $|\overline{\gamma}|$ for each pixel. Table II compares the selection results for copolar, Pauli, and optimum channels. The improvement is notorious for all the scenes considered, particularly for urban environment, where we get about 37% more pixels selected compared to the best of single-polarization channels (HH). The increment with respect to VV is over 60% in all cases. The location of selected PSCs is shown in Fig. 4.

In Fig. 5, we show the histograms of α and ψ corresponding to points selected as PSCs after the optimization, in both polar representation and as separate histograms for each parameter. Most of the PSCs are found in the range $(\pi/4) < \alpha < (\pi/2)$, which correspond to anisotropic dihedrals, commonly found in urban environments. As for rural area, the total number of

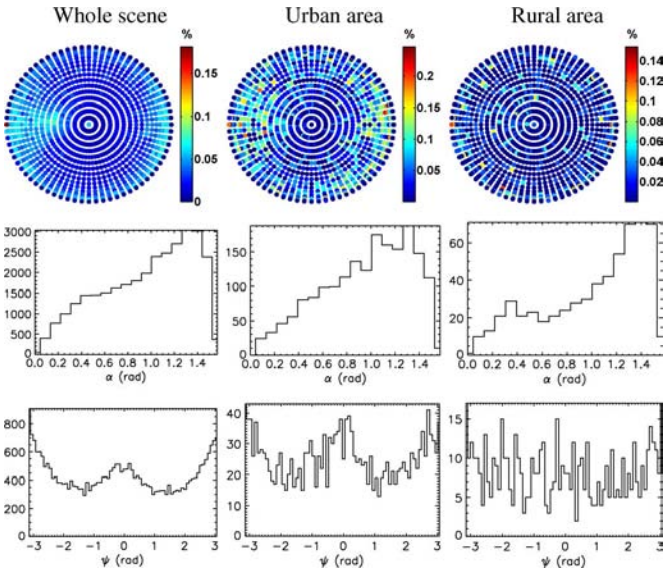

Fig. 5. Histograms of α and ψ associated with PSCs selected by $|\overline{\gamma}|$ optimization.

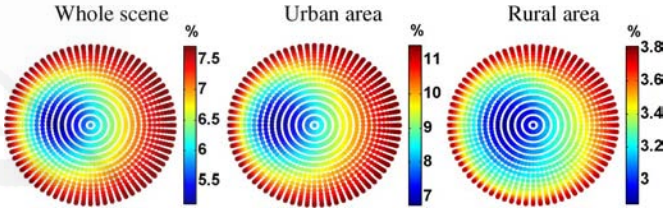

Fig. 6. Density of PSCs (expressed in percent) selected for each polarimetric channel, considering the D_A criterion with a 0.3 threshold.

PSCs selected decreases with respect to the urban scenario, but histograms still show a predominance of dihedral-like responses belonging to stable human-built structures, such as fences or small buildings. As for ψ, most PSCs show values near zero or $\pm\pi$, although this trend is not so evident for the rural subscene. First insights point out that parameter ψ is related to the orientation of the scatterers, with $\psi \approx 0$ for targets with a dominant horizontal response and $\psi \approx \pm\pi$ in the case of dominant vertical response. This should be confirmed and quantified in future work with ground-truth data.

B. Selection Based on Amplitude Dispersion

In this section, we present selection results obtained for the amplitude dispersion (D_A) criterion. The optimization proposed in [1] consists in finding, for each pixel, the $\underline{\omega}$ that minimizes the following expression:

$$D_A = \frac{\sigma_a}{\bar{a}} = \frac{1}{|\overline{\underline{\omega}^\dagger \underline{k}}|\sqrt{N}} \sqrt{\sum_{i=1}^{N} \left(|\underline{\omega}^\dagger \underline{k}_i| - |\overline{\underline{\omega}^\dagger \underline{k}}| \right)^2} \qquad (3)$$

where σ_a is the amplitude standard deviation, $\bar{a}$ is the mean amplitude, N is the number of images, and k_i is the target vector of the pixel for image i.

As done with the average-coherence criterion, in Fig. 6, we show the number of PSCs selected for different channels. We established an arbitrary threshold for D_A of 0.3. Results look quite similar to those obtained for the average-coherence

TABLE III
PSCs SELECTED FOR DIFFERENT POLARIMETRIC CHANNELS AND THE OPTIMIZED RESULT, CONSIDERING A D_A THRESHOLD OF 0.3

	HH	VV	HH+VV	HH−VV	Optimum
Whole scene	7.32%	6.02%	5.84%	7.66%	16.32%
Urban area	10.64%	8.03%	8.14%	11.33%	23.43%
Rural area	3.49%	3.20%	2.99%	3.72%	8.03%

criterion, although improvement is more significant for urban area, with a difference of 70% in the number of PSCs selected by the best and the worst channels, than for rural area, with only 33% difference. Notice that, as already mentioned in the introduction, D_A is more sensitive to polarimetric features since it is computed for single-look data, so polarimetric response is more likely to be dominated by orientation and structure of single strong scatterers inside the resolution cell, instead of being defined by the averaged features of an extended area. Consequently, selecting the same channel for all the scenes is still not achieving a notorious improvement with respect to single-polarization HH or VV. On the other hand, Table III shows a comparison of PSC selections for HH and VV channels, the Pauli channels, and the optimization result. In this case, there is a dramatic improvement in amplitude stability when we consider the optimum channel, in contrast to any of the conventional channels, even for rural area. The increase of PSC with respect to HH is over 120% in all cases. The increase with respect to VV channel ranges from 150% for rural area to 191% for urban area, which means almost triple the number of PSCs selected. Location of the selected PSCs is shown in Fig. 4.

Fig. 7 shows the histograms of α and ψ for pixels selected as PSCs after the optimization, considering a D_A threshold of 0.3. Histograms of α show maximum values near $\alpha = \pi/4$, but with larger variance than that for the average-coherence criterion (obtained with multilooked data). As for ψ, most pixels have values near $\pm\pi$. These results indicate a predominance of scattering from anisotropic dihedrals and vertically oriented structures, even for rural area. The polarimetric response from this kind of structures is strongly dependent upon orientation, as we can extract from the high variance of α and ψ; so, selecting only one channel (e.g., VV) for the whole scene would lead us to missing many potential PSCs, as revealed in Table III and Fig. 6. In this sense, the HH − VV channel would be a better *a priori* choice because of the wider scattering pattern associated with dihedrals. Nevertheless, as already demonstrated, much better results are achieved if we explore the whole available polarimetric space in a pixel-by-pixel basis.

C. PSC Selection for the Single-Polarization Data Set

The conventional pixel candidate selection has also been carried out for the single-polarization stack of images described in Section II, in order to evaluate the influence of the finer azimuth resolution of the single-polarization images. A multilook of 5 × 7 has been used for the coherence computation (ENL of 17, similar to dual-polarization 7 × 7). The same baseline limits have been considered (100 m; 100 days), generating 140 interferograms from the 41 images. Table IV shows the percentage of pixel candidates selected for different $\overline{|\gamma|}$ thresholds. These results are quite similar to those obtained for VV

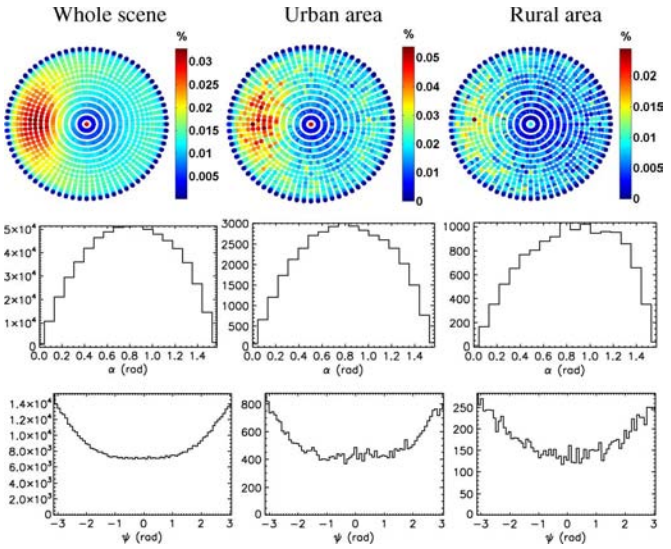

Fig. 7. Histograms of α and ψ associated with PSCs selected by D_A optimization.

TABLE IV
PSCs SELECTED FOR THE SINGLE-POLARIZATION DATA SET

	Whole scene	Urban area	Rural area
$\overline{\|\gamma\|} \geq 0.7$	22.95%	34.20%	11.56%
$D_A \leq 0.3$	5.67%	8.40%	3.27%

channel for the dual-polarization images. In this case, the better azimuth resolution of the single-polarization images has no significant influence in terms of area covered by pixel candidates. Therefore, for this application, it is more convenient to gather polarimetric data (despite their worse spatial resolution) since polarimetry provides a way to increase, in absolute terms, the area with deformation measurements.

D. Deformation Results

Finally, in order to confirm the suitability of the optimized data for the generation of accurate deformation results, the whole PSI processing chain was applied, and deformation maps were generated. We considered the average-coherence criterion with a multilook factor of 7 × 7. Selection follows a multilayer scheme [8], with thresholds from 0.9 to 0.7, so that the best quality pixels are selected and processed first and then used to improve the performance of subsequent layers. Fig. 8 shows the deformation rate (or velocity) of the area, estimated using both VV and the optimum channel. The number of PSCs, and hence coverage, obtained for the optimum channel is higher than that for single-polarization data, as expected.

An analysis over the common pixels (selected in both VV and optimum cases) shows that, in this scene, neither deformation velocities nor DEM errors differ significantly, since the density of pixels was quite high already with the VV channel. Therefore, the improvement can be quantified in terms of the additional information obtained at the extra pixels, which provides finer details and values over areas without information in the previous case.

As an example of the previous comment, Fig. 9 shows a detail of deformation results obtained for a highway bridge and its

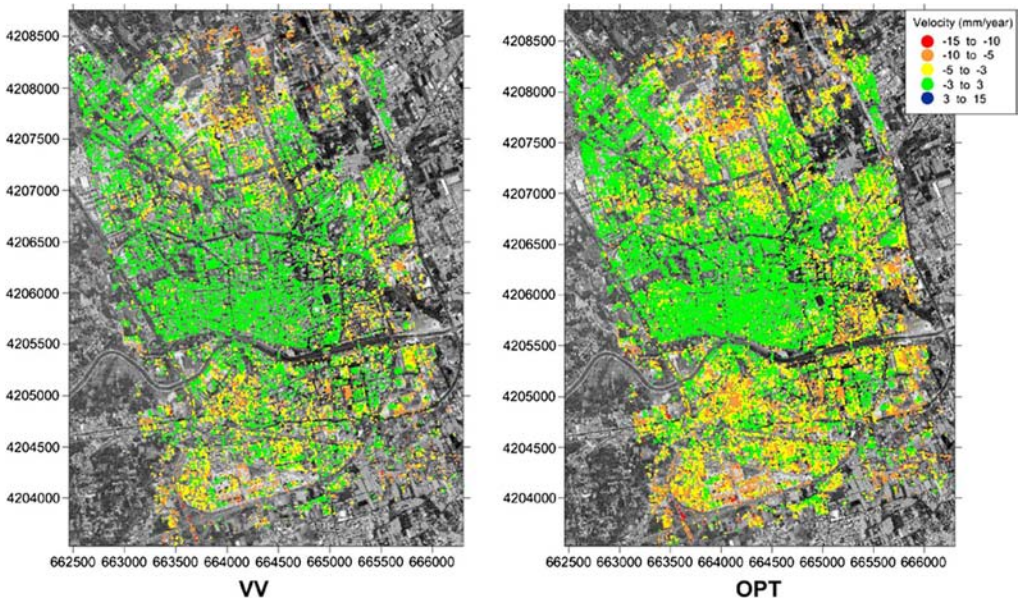

Fig. 8. Deformation results obtained for (left) the VV channel and (right) the computed optimum channel.

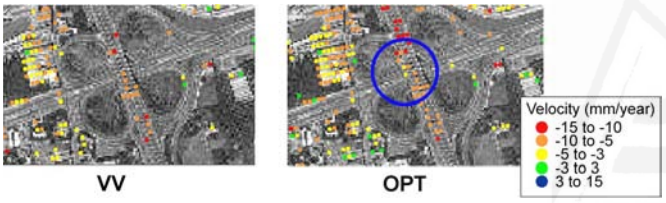

Fig. 9. Detail of deformation results for a highway bridge.

access ramps. The center of the bridge exhibits a stable behavior (subsidence less than -5 mm/year), due to the deep foundations of the pillars holding the structure, while the access ramps show more important deformation rates, due to the compression of the embankment. These results agree with those presented in [9], obtained using PSI with 39 single-polarization TerraSAR-X images, a multilook of 3×3, and $\overline{|\gamma|}$ threshold of 0.7.

IV. Conclusion

In this letter, we have confirmed the suitability of the approach proposed in [1] to improve the performance of PSI techniques by means of a polarimetric optimization. Results show a significant increase in the number of PSCs, which translates into denser maps with valid deformation estimates.

The polarimetric study of selected PSCs reveals a predominance of dihedral-like scatterers for multilook data. The most plausible explanation is that multilooking of large irregular structures behaving as dihedrals (e.g., building-ground) filters out irregularities, hence revealing an average nearly pure dihedral response. On the other hand, single-look data are dominated by anisotropic dihedrals and vertical structures, with scattering patterns very sensitive to the polarimetric channel. Consequently, benefits of the optimization are specially notorious for single-look data, with an increase of about 191% with respect to single-polarization VV data.

A quad-polarization extension of this approach will be tested in the next future with Radarsat-2 fully polarimetric data, as soon as we have enough images available. In addition, alternative selection criteria based on polarimetric features and polarimetric stationarity will be studied. Finally, the influence of frequency band upon the characteristics of targets selected as PSCs should be studied.

Acknowledgment

All synthetic aperture radar images have been provided by the German Aerospace Center (DLR) in the framework of Project GEO0389 of the TerraSAR-X Scientific Program.

References

[1] V. D. Navarro-Sanchez, J. M. Lopez-Sanchez, and F. Vicente-Guijalba, "A contribution of polarimetry to satellite differential SAR interferometry: Increasing the number of pixel candidates," *IEEE Geosci. Remote Sens. Lett.*, vol. 7, no. 2, pp. 276–280, Apr. 2010.

[2] A. Ferretti, C. Prati, and F. Rocca, "Nonlinear subsidence rate estimation using permanent scatterers in differential SAR interferometry," *IEEE Trans. Geosci. Remote Sens.*, vol. 38, no. 5, pp. 2202–2212, Sep. 2000.

[3] P. Berardino, G. Fornaro, R. Lanari, and E. Sansosti, "A new algorithm for surface deformation monitoring based on small baseline differential SAR interferograms," *IEEE Trans. Geosci. Remote Sens.*, vol. 40, no. 11, pp. 2375–2383, Nov. 2002.

[4] O. Mora, J. J. Mallorquí, and A. Broquetas, "Linear and nonlinear terrain deformation maps from a reduced subset of interferometric SAR images," *IEEE Trans. Geosci. Remote Sens.*, vol. 41, no. 10, pp. 2243–2253, Oct. 2003.

[5] P. Perissin and A. Ferretti, "Urban-target recognition by means of repeated spaceborne SAR images," *IEEE Trans. Geosci. Remote Sens.*, vol. 45, no. 12, pp. 4043–4058, Dec. 2009.

[6] S. R. Cloude and K. P. Papathanassiou, "Polarimetric SAR interferometry," *IEEE Trans. Geosci. Remote Sens.*, vol. 36, no. 5, pp. 1551–1565, Sep. 1998.

[7] R. Touzi, A. Lopes, J. Bruniquel, and W. P. Vachon, "Coherence estimation for SAR imagery," *IEEE Trans. Geosci. Remote Sens.*, vol. 37, no. 1, pp. 135–149, Jan. 1999.

[8] P. Blanco, J. Mallorqui, S. Duque, and D. Navarrete, "Advances on DInSAR with ERS and ENVISAT data using the coherent pixels technique (CPT)," in *Proc. IGARSS*, Aug. 2006, pp. 1898–1901.

[9] G. Herrera, R. Tomás, D. Monells, G. Centolanza, J. J. Majorquí, F. Vicente, V. D. Navarro, J. M. Lopez-Sanchez, M. Sanabria, M. Cano, and J. Mulas, "Analysis of subsidence using TerraSAR-X data: Murcia case study," *Eng. Geol.*, vol. 116, no. 3/4, pp. 284–295, Nov. 2010.

3.3 Polarimetric Approaches for Persistent Scatterers Interferometry

Polarimetric Approaches for Persistent Scatterers Interferometry

Victor D. Navarro-Sanchez, *Student Member, IEEE*, Juan M. Lopez-Sanchez, *Senior Member, IEEE*, and Laurent Ferro-Famil, *Member, IEEE*

***Abstract*— In previous works, a general framework to exploit polarimetric diversity to optimize the results of persistent scatterers interferometry (PSI) was presented, but tested only with dual-pol data. In this paper, the performance of these algorithms is assessed using fully polarimetric data, acquired by the Radarsat-2 satellite over the urban area of Barcelona, Spain. In addition, two new highly efficient polarimetric optimization methods, mean intensity polarimetric optimization and joint diagonalization-based polarimetric optimization, are introduced and evaluated. Given the variety of dual-pol configurations provided by current polarimetric satellites, such as TerraSAR-X and Radarsat-2, and the upcoming launch of Sentinel-1, ALOS-2, and Radarsat Constellation Mission, a study has been also carried out to determine the best performing dual-pol configurations for polarimetric PSI. Subsidence maps of the area of study are computed for single-pol, dual-pol, and full-pol data, which show the increase in pixel density with valid deformation results as more polarimetric information is made available. In particular, for full-pol data we get an increase of up to 2.5 times more pixels for coherence-based PSI techniques (degraded resolution), and over four times more for amplitude-based approaches (full resolution), in comparison with single-pol data. Both higher density and quality of pixels yield better results in terms of coverage and accuracy.**

***Index Terms*— Persistent scatterers, polarimetry, subsidence, synthetic aperture radar (SAR) interferometry.**

I. Introduction

PERSISTENT scatterers interferometry (PSI) is a popular tool for the retrieval of accurate subsidence maps, thanks to its wider coverage and lower cost in comparison with traditional approaches based on the deployment of *in situ* instrumentation (e.g., GPS sensor networks). PSI techniques analyze stacks of differential interferograms built from a set of synthetic aperture radar (SAR) images, generally acquired by satellite sensors operating in single-pol configuration [1]–[5]. One of the main features of these techniques is that they start selecting for processing only those pixels that are considered as *a priori* reliable under certain quality criteria. We usually refer to these pixels as persistent scatterer candidates (PSCs) for amplitude-based criteria, or coherent pixel candidates (CPCs) for selection based on interferometric coherence. Then, in the following steps of the data processing, these points will be either confirmed as suitable for the method or discarded if they do not exhibit the expected behavior. The quality and density of PSCs or CPCs in the scene is a decisive factor for the accuracy of the outcome of the system.

Though traditionally applied to single-pol data, the availability of improved satellite SAR sensors with polarimetric capabilities such as Radarsat-2, TerraSAR-X, or ALOS-PALSAR makes us wonder how this diversity may help us to improve performance of PSI techniques. To this end, in previous works [6], [7], we analyzed the potential use of polarimetry in PSI. A polarimetric optimization approach was proposed, which consisted of a search over the available polarimetric space in order to find, for each pixel, the projection channel that optimized the selection criterion, thus maximizing the number of input points for the PSI method. Polarimetric (multichannel) data can be reprojected onto this optimum channel, getting a complex scattering coefficient analogous to single-pol data. Therefore, this technique can be applied as a preprocessing step for a variety of PSI approaches, with no need of further modification.

In the aforementioned works, we tested the approach using TerraSAR-X data in a dual-pol (HH, VV) configuration for two of the most commonly used criteria of selection: the amplitude dispersion index D_A computed over a set of calibrated SAR images, and the average interferometric coherence $|\overline{\gamma}|$, computed over a set of multilooked differential interferograms, obtaining in both cases a significant increase in the number of points selected. We also observed that the analysis of the obtained projection vectors helps us to interpret and identify the different scattering mechanisms present in the area of interest.

In addition to the algorithms introduced in [6] and [7], two new polarimetric PSI approaches are presented in this paper: mean intensity polarimetric optimization (MIPO) and joint diagonalization-based polarimetric optimization (JDPO) which is a modified version of the coherence optimization algorithm proposed in [8] and makes it suitable for our problem. Alternative ways of using polarimetry in conjunction with satellite PSI have been also proposed by other authors in [9] (separation of different scatterers in the same resolution

Manuscript received September 5, 2012; revised January 17, 2013; accepted March 10, 2013. Date of publication May 6, 2013; date of current version December 17, 2013. This work was supported in part by the Spanish Ministerio de Economía y Competitividad and European Union FEDER funds under Project TEC2011-28201-C02-02.

V. D. Navarro-Sanchez and J. M. Lopez-Sanchez are with the Signals, Systems and Telecommunication Group, EPS, University of Alicante, Alicante E-03080, Spain (e-mail: victor.navarro@ieee.org; juanma-lopez@ieee.org).

L. Ferro-Famil is with the SAR Polarimetry Holography Interferometry Radargrammetry Team, Institute of Electronics and Telecommunications of Rennes, University of Rennes 1, Rennes 35042, France (e-mail: laurent.ferro-famil@univ-rennes1.fr).

Color versions of one or more of the figures in this paper are available online at http://ieeexplore.ieee.org.

Digital Object Identifier 10.1109/TGRS.2013.2253111

cell) and [10] (identification of building to ground relative deformation).

New-generation satellite SAR sensors are able to provide polarimetric data in a wide range of configurations. Unfortunately, many of them are only capable of acquiring dual-pol data, as is the case for the upcoming European Space Agency's Sentinel-1. In this paper, a set of full-pol single look complex (SLC) Radarsat-2 images has been used to test the behavior of polarimetric PSI approaches with a complete set of configurations as provided by full polarimetry, including all dual-pol combinations and the synthesized compact or hybrid-pol [11] mode, which will be made available by the Radarsat Constellation Mission. The main objectives of this paper are, therefore: 1) to determine the best performing polarimetric PSI approach in terms of coverage and quality of the final results; 2) to assess the benefits of using full-pol data over dual-pol and single-pol data; and (3) to find the best dual-pol acquisition mode (if any) to be used when quad-pol data are not available.

A summary of the general formulation and the new proposed approaches are presented in Section II. Section III describes the available dataset, and Section IV presents the obtained results in form of selection tables and deformation velocity maps.

II. Formulation

A. Polarimetric SAR Interferometry

A general formulation for polarimetric SAR interferometry (also called vector interferometry) was introduced in [12]. For each resolution element, a scattering vector (or *target vector*) $\mathbf{k}$ is obtained as a vectorization of its scattering matrix $\mathbf{S}$ as

$$\mathbf{k} = \frac{1}{\sqrt{2}} \begin{bmatrix} \mathrm{HH} + \mathrm{VV} \\ \mathrm{HH} - \mathrm{VV} \\ 2\mathrm{HV} \end{bmatrix} \tag{1}$$

where HH and VV stand for the horizontal and vertical copolar channels, respectively, HV is the crosspolar channel, and the Pauli basis has been used for vectorization. Notice that we assume HV = VH because of reciprocity.

In order to generate an interferogram, each target vector $\mathbf{k}$ can be projected onto a unitary complex column vector $\boldsymbol{\omega}$, resulting in a scattering coefficient μ defined as $\mu = \boldsymbol{\omega}^\dagger \mathbf{k}$ [12], where † stands for the Hermitian or conjugated transpose. The scattering coefficient μ is a scalar complex value, obtained as a linear combination of the elements of $\mathbf{k}$. As a complex value, it is analogous to what we could get from a single-channel SAR system for a resolution element. Thus, we can make use of all interferometry techniques developed for single-pol data, including PSI, by applying them to μ.

B. Exhaustive Search Polarimetric Optimization (ESPO)

In [6] and [7], we proposed a general framework for PSI polarimetric optimization. The objective is to maximize the number of pixels selected as reliable *a priori*. This first approach, hereafter named as exhaustive search polarimetric optimization (ESPO), consists in finding, for each pixel, the projection vector $\boldsymbol{\omega}$ that optimizes the parameter considered as quality criterion. For fully polarimetric data, $\boldsymbol{\omega}$ can be parameterized as follows:

$$\boldsymbol{\omega} = \begin{bmatrix} \cos(\alpha) \\ \sin(\alpha)\cos(\beta)e^{j\delta} \\ \sin(\alpha)\sin(\beta)e^{j\psi} \end{bmatrix}, \quad \begin{cases} 0 \leqslant \alpha \leqslant \pi/2 \\ 0 \leqslant \beta \leqslant \pi/2 \\ -\pi \leqslant \delta < \pi \\ -\pi \leqslant \psi < \pi \end{cases} \tag{2}$$

so the problem is reduced to finding four real parameters α, β, δ, and ψ whose ranges are finite and known, and whose values are related to the geometric and electromagnetic features of the target [13]. In order to avoid introducing a variable phase term that might be misinterpreted as line-of-sight displacement of the scatterers, we constrain the optimum $\boldsymbol{\omega}$ obtained for each pixel to be the same along all the stack of images. This constraint is usually referred to as equal scattering mechanisms (ESMs) [14], and it can be interpreted as selecting the most stable scattering mechanism over time, according to the chosen criterion of selection. The ESPO method can be thought of as an extension to the Union algorithm proposed in [15], which consists in selecting, for each pixel, the best choice from a limited set of conventional channels, e.g., HH and VV, instead of searching the whole available polarimetric space. Evidently, the Union algorithm leads to a suboptimal solution, but at a much lower computational cost.

The ESPO approach has been formulated and tested for two of the most commonly used criteria of selection: minimization of the amplitude dispersion index D_A, computed over single-look complex data [1]; and maximization of the average magnitude of the interferometric coherences $\overline{|\gamma|}$, estimated using a multilook scheme [3], [4]. In the context of polarimetric interferometry, $\overline{|\gamma|}$ can be expressed as follows:

$$\overline{|\gamma|} = \frac{1}{K}\sum_{k=1}^{K} |\gamma_k|, \text{ with } \gamma_k(\boldsymbol{\omega}) = \frac{\boldsymbol{\omega}^\dagger \boldsymbol{\Omega}_{ij} \boldsymbol{\omega}}{\sqrt{\boldsymbol{\omega}^\dagger \mathbf{T}_{ii} \boldsymbol{\omega}}\sqrt{\boldsymbol{\omega}^\dagger \mathbf{T}_{jj} \boldsymbol{\omega}}} \tag{3}$$

where the subscript k denotes the kth interferogram obtained by combining images i and j. Polarimetric coherency matrices $\mathbf{T}_{ii}$, $\mathbf{T}_{jj}$ and polarimetric interferometric cross-correlation matrix $\boldsymbol{\Omega}_{ij}$ are defined as in [12]

$$\mathbf{T}_{ii} = E[\mathbf{k}_i \mathbf{k}_i^\dagger], \quad \mathbf{T}_{jj} = E[\mathbf{k}_j \mathbf{k}_j^\dagger], \quad \boldsymbol{\Omega}_{ij} = E[\mathbf{k}_i \mathbf{k}_j^\dagger] \tag{4}$$

where $E[\cdot]$ is the expectation operator. Notice that such expectations cannot be computed in practice, so they will be replaced by their maximum likelihood estimates that are given, under the usual Gaussian distribution assumption, by the empirical mean evaluated using L independent realizations (or looks) of the target vectors.

Points with $\overline{|\gamma|}$ greater than a given threshold will be considered coherent pixel candidates (CPCs).

As for D_A, it can be expressed as [6], [7]

$$D_A = \frac{\sigma_a}{\bar{a}} = \frac{1}{\overline{|\boldsymbol{\omega}^\dagger \mathbf{k}|}\sqrt{N-1}} \sqrt{\sum_{i=1}^{N} \left(|\boldsymbol{\omega}^\dagger \mathbf{k}_i| - \overline{|\boldsymbol{\omega}^\dagger \mathbf{k}|} \right)^2} \tag{5}$$

where N is the total number of images, and the overline indicates empirical mean value. Points with D_A under an established threshold will be selected as PSCs.

Concerning the actual implementation of the search, in the case of dual-pol data, where only two search parameters (α, ψ) are considered, a conventional fine grid search (step $\leqslant 5°$) is feasible from the computational viewpoint. Instead, when dealing with fully polarimetric data, the search space is significantly increased, and computational cost rises accordingly. To overcome this drawback, a coarse grid approach ($5° <$ step $\leqslant 15°$) to avoid falling in local minima plus a conjugated gradient descent scheme is adopted in the implementation of ESPO. In order to avoid the inherent complexity of this numerical search, two new approaches are proposed in the next sections.

C. Joint Diagonalization-Based Polarimetric Optimization (JDPO)

An efficient alternative approach for interferometric coherence optimization that takes into account the ESM constraint was proposed in [8]. Polarimetric information of each image is first whitened by applying the following transformation to the target vector associated with each pixel: $\tilde{\mathbf{k}}_i = \mathbf{T}_{ii}^{-\frac{1}{2}}\mathbf{k}_i$. Then, the whitened interferometric coherence is given by

$$\tilde{\gamma}_k(\tilde{\boldsymbol{\omega}}) = \tilde{\boldsymbol{\omega}}^{\dagger}\tilde{\boldsymbol{\Omega}}_{ij}\tilde{\boldsymbol{\omega}} \quad \text{with} \quad \tilde{\boldsymbol{\Omega}}_{ij} = \mathbf{T}_{ii}^{-\frac{1}{2}}\boldsymbol{\Omega}_{ij}\mathbf{T}_{jj}^{-\frac{1}{2}}. \tag{6}$$

The whitened correlation matrix $\tilde{\boldsymbol{\Omega}}_{ij}$ can be written using special unitary (SU) operators as

$$\tilde{\boldsymbol{\Omega}}_{ij} = \mathbf{U}\mathbf{D}\mathbf{U}^{\dagger} \text{ with } \mathbf{U}\mathbf{U}^{\dagger} \text{ and } |\mathbf{U}| = +1 \tag{7}$$

where $\mathbf{D}$ is, in general, not diagonal, and $\mathbf{U}$ can be expressed, for the full-pol case, as a function of three orthogonal unitary vectors $\mathbf{U} = [\mathbf{u}_1, \mathbf{u}_2, \mathbf{u}_3]$. From (6) and (7), it follows that the whitened interferometric coherence values for $\tilde{\boldsymbol{\omega}}_n = \mathbf{u_n}$ correspond to the diagonal elements of $\mathbf{D}$, i.e., $\tilde{\gamma}_k(\tilde{\boldsymbol{\omega}}_n) = d_{nn}$, $n = 1 \ldots q$, with q equal to the dimensionality of $\mathbf{k}$ ($q = 2$ for dual-pol data, $q = 3$ for full-pol data). Therefore, the proposed approach consists in finding the SU operator $\mathbf{U}_{\text{opt}} = [\mathbf{u}_{\text{opt1}}, \mathbf{u}_{\text{opt2}}, \mathbf{u}_{\text{opt3}}]$ that simultaneously diagonalizes (i.e., maximizes $\sum_{n=1}^{3} |d_{\text{nn}}|^2$ while keeping $\sum_{i,j=1}^{3} |d_{ij}|^2$ constant) the set of $\tilde{\boldsymbol{\Omega}}_k$ matrices, obtaining $\mathbf{D}_k$. The operator $\mathbf{U}_{\text{opt}}$ can be computed iteratively in a very efficient way by using the extended Jacobi technique for simultaneous diagonalization described in [16], which constructs $\mathbf{U}_{\text{opt}}$ as a product of plane rotations globally applied to every $\tilde{\boldsymbol{\Omega}}_k$. However, some considerations on this solution have to be taken into account for our application.

First of all, notice that we do not have a unique optimum projection vector, but a basis of three orthogonal vectors, each one with an associated coherence value. In an ideal case, that is to say, polarimetrically stationary data with a single dominant scattering mechanism along the whole stack of interferograms, one of the obtained projection vectors will give us the maximum average coherence value. However, when dealing with non-purely-stationary data, we observe that each of the projection vectors $\tilde{\boldsymbol{\omega}}_n = \mathbf{u}_{\text{optn}}$ can lead to the highest coherence values for different subsets of interferograms. Consequently, selecting only one of these mechanisms for the whole set, in order to satisfy the ESM constraint, will lead us to a suboptimal solution. To solve this issue, the adopted approach consists in selecting the projection vector $\tilde{\boldsymbol{\omega}}_{\text{opt}}$ whose associated $|\tilde{\gamma}_k|$ is highest for the majority of interferograms. We observed that the average coherence of the pixel is closely related to the proportion of interferograms sharing the same dominant scattering mechanism, so, generally, points with a nonstationary behavior will be discarded by coherence thresholding.

The second issue to consider has to do with the unwhitening transformation needed to return to the original basis. To this end, we arrived at a different expression to the one proposed in [8]. As demonstrated in Appendix I, $\gamma_k(\boldsymbol{\omega}_i, \boldsymbol{\omega}_j) = \tilde{\gamma}_k(\tilde{\boldsymbol{\omega}}_i, \tilde{\boldsymbol{\omega}}_j)$ when the projection vectors satisfy

$$\tilde{\boldsymbol{\omega}}_i = \frac{\mathbf{T}_{ii}^{\frac{1}{2}}\boldsymbol{\omega}_i}{\sqrt{\boldsymbol{\omega}_i^{\dagger}\mathbf{T}_{ii}\boldsymbol{\omega}_i}} \quad \tilde{\boldsymbol{\omega}}_j = \frac{\mathbf{T}_{jj}^{\frac{1}{2}}\boldsymbol{\omega}_j}{\sqrt{\boldsymbol{\omega}_j^{\dagger}\mathbf{T}_{jj}\boldsymbol{\omega}_j}} \tag{8}$$

$$\boldsymbol{\omega}_i = \frac{\mathbf{T}_{ii}^{-\frac{1}{2}}\tilde{\boldsymbol{\omega}}_i}{\sqrt{\tilde{\boldsymbol{\omega}}_i^{\dagger}\mathbf{T}_{ii}^{-1}\tilde{\boldsymbol{\omega}}_i}} \quad \boldsymbol{\omega}_j = \frac{\mathbf{T}_{jj}^{-\frac{1}{2}}\tilde{\boldsymbol{\omega}}_j}{\sqrt{\tilde{\boldsymbol{\omega}}_j^{\dagger}\mathbf{T}_{jj}^{-1}\tilde{\boldsymbol{\omega}}_j}}. \tag{9}$$

From these equations, we can extract

$$\text{When } \mathbf{T}_{ii} \neq \mathbf{T}_{jj} \begin{cases} \boldsymbol{\omega}_i = \boldsymbol{\omega}_j \Rightarrow \tilde{\boldsymbol{\omega}}_i \neq \tilde{\boldsymbol{\omega}}_j \\ \tilde{\boldsymbol{\omega}}_i = \tilde{\boldsymbol{\omega}}_j \Rightarrow \boldsymbol{\omega}_i \neq \boldsymbol{\omega}_j. \end{cases} \tag{10}$$

Consequently, an ESM scheme in the whitened basis will correspond to a multiple scattering mechanism (MSM) scheme in the original basis. However, from the analysis of both real and simulated data we can conclude that, as long as the matrices $\mathbf{T}_{ii}$, $\mathbf{T}_{jj}$ are relatively similar, the following approximation holds

$$\gamma_k(\boldsymbol{\omega}_{\text{opt}}, \boldsymbol{\omega}_{\text{opt}}) \approx \tilde{\gamma}_k(\tilde{\boldsymbol{\omega}}_{\text{opt}}, \tilde{\boldsymbol{\omega}}_{\text{opt}}) \approx \gamma_k(\tilde{\boldsymbol{\omega}}_{\text{opt}}, \tilde{\boldsymbol{\omega}}_{\text{opt}}) \tag{11}$$

which implies that no transformation is needed for the optimum projection vector. It is important to point out that pixels whose associated $\mathbf{T}$ matrices differ significantly along the set of images (i.e., along time) will generally exhibit an average interferometric coherence magnitude below the quality threshold, and therefore they are likely to be discarded. Actually, being able to detect pixels with such an erratic polarimetric behavior is basic for the proper functioning of PSI algorithms. Consequently, (11) will hold for most of the points prone to be selected as CPC, i.e., pixels that actually present a stationary polarimetric behavior.

D. Mean Intensity Polarimetric Optimization (MIPO)

As already demonstrated in [6] and [7], the ESPO approach is an effective algorithm to minimize D_A. Generally, we assume that low values of D_A are associated with stable reflectivity values of point-like scatterers (persistent scatterers, PS). As point-like scatterers, they are not affected by spatial decorrelation, and D_A becomes a good estimator of phase standard deviation [1]. However, ESPO minimizes D_A of PS as well as D_A of clutter (i.e., pixels without any point-like scatterer), so more non-point-like scatterers are prone to pass the selection stage. Consequently, many of the selected PSCs will be discarded in subsequent steps because of their high spatial decorrelation. In this paper, we propose an alternative

method based on finding the projection vector $\boldsymbol{\omega}$ that optimizes the mean intensity (or average power) for each pixel along the stack of images. This way, we make sure that our projection vector is associated with the dominant or more powerful scatterer mechanism in the resolution cell. Afterward, we still can make use of a stability criteria, such as D_A thresholding, over the intensity-optimized data. In the following, we will refer to this method as MIPO.

The intensity of projected signal μ can be expressed as $I = |\mu|^2 = \mu \cdot \mu^*$, where * stands for conjugation. Under the assumption that, along the stack of N images, $\mathbf{k}$ follows a zero-mean circular complex multivariate Gaussian distribution with $q \times q$ coherency matrix $\mathbf{T}$, denoted as $\mathbf{k} \sim \mathcal{N}_q^{\mathbb{C}}(0, \mathbf{T})$, and the maximum likelihood estimate of the mean intensity $\overline{I}$ for a given pixel can be obtained as

$$\overline{I} = E\left[\mu \cdot \mu^*\right] = \boldsymbol{\omega}^{\dagger}\widehat{\mathbf{T}}\boldsymbol{\omega}, \quad \text{with} \quad \widehat{\mathbf{T}} = \frac{1}{N}\sum_{i=1}^{N}\mathbf{k}_i \cdot \mathbf{k}_i^{\dagger} \tag{12}$$

where $E[\cdot]$ is the expectation operator, and $\widehat{\mathbf{T}}$ is the maximum likelihood estimate of $\mathbf{T}$. This equation is in quadratic form, where $\widehat{\mathbf{T}}$ is Hermitian semidefinite positive, and $\boldsymbol{\omega}$ is unitary. Therefore, maximization of $\overline{I}$ for a given pixel can be posed as an eigenproblem, where the maximum possible value is the maximum eigenvalue of $\widehat{\mathbf{T}}$, and the optimum scattering mechanism is given by its corresponding eigenvector.

E. Summary of Approaches

In the following, we provide a comprehensive summary of the presented methods.

1) ESPO [6], [7] consists of a search over the available polarimetric space in order to find the channel that optimizes the quality criterion. This method is suitable for both PSC selection (full resolution) and for CPC selection (degraded resolution, because spatial averaging is required for the estimation of interferometric coherence).
2) Union [15] can be considered a simplified version of ESPO. For each pixel, we select the best choice from a reduced set of available channels. Hence, no reprojection of data is performed. It is suitable for both PSC and CPC selection.
3) JDPO algorithm is an adaptation of the one presented in [8]. It finds the optimum projection vector by obtaining the SU operator that best diagonalizes the whole set of whitened interferometric coherency matrices associated with the pixel. This method is not suitable for PSC selection, since it requires spatial averaging for the estimation of interferometric coherency matrices.
4) MIPO finds the polarimetric channel that optimizes mean intensity of the pixel over time. It is suitable for full-resolution criteria such as PSC selection, since it does not require spatial averaging.

III. DATASET

A set of 31 full-pol SLC images acquired by Radarsat-2 from January 2010 to February 2012 over the urban area of Barcelona, Spain, has been used to test the proposed algorithms. Images have been acquired at a revisit time of 24 days using Radarsat-2 beam mode FQ9: nominal incidence angle of 28° (near range) to 29.8° (far range). Nominal azimuth and slant-range resolutions are 7.6 and 5.2 m, respectively, whereas nominal pixel dimensions are 5.1 and 4.7 m, respectively. Therefore, the resulting oversampling factors are 1.49 and 1.11 in azimuth and range.

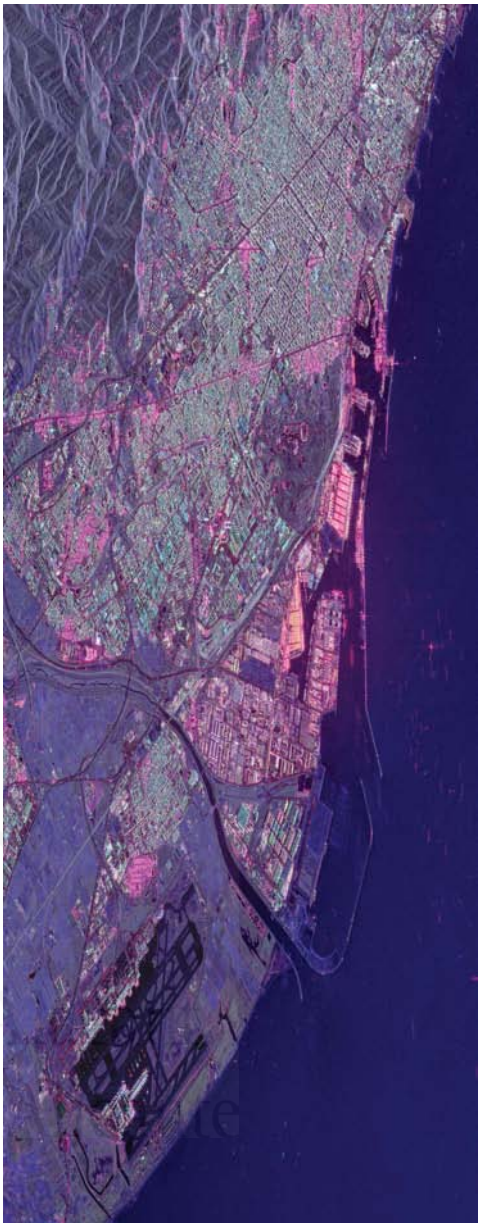

Fig. 1. Composite RGB image of the area under study in Barcelona, Spain, formed by the average intensities. Channels: $R = \mathrm{HH} - \mathrm{VV}$, $G = 2\mathrm{HV}$, $B = \mathrm{HH} + \mathrm{VV}$

The processing has been applied over a section of the image of 1400×3600 pixels, where nonurban areas (mainly sea and mountains) have been masked out. A color composite formed by the Pauli average intensities of the whole area is shown in Fig. 1. The different colors in the composite image provide an insight into the information content of polarimetry. The city is mostly located in the center of the image, showing

TABLE I
CPC SELECTED FOR DIFFERENT CHANNELS, CONSIDERING A $\overline{|\gamma|}$ THRESHOLD OF 0.7

HH	15.09%	RH	15.41%
VV	14.01%	RV	14.53%
HV	14.69%	HH+VV	13.85%
VH	14.58%	HH−VV	16.23%

different dominant channels at different parts. Buildings tend to behave as oriented dihedrals (due to double reflections facade–ground), whose polarimetric response depends highly on the orientation angle (OA) [17]. Dihedrals with an OA of 45° have a dominant cross-polar response, whereas 22.5° rotated dihedrals reflect equally all four polarimetric channels.

From the full-pol Radarsat-2 data, we can generate different dual-pol sets in order to evaluate performance of the proposed methods when full-pol data are not available. Of special interest are the following combinations: [HH, VV] (TerraSAR-X dual-pol mode), [HH, HV] and [VV, VH] (future ESA Sentinel-1 polarimetric modes) and hybrid or compact-pol (available for future Radarsat Constellation Mission, RCM), in which circular polarization is transmitted and linear H and V are received: [RH, RV], where R stands for right-circular. Transformation operations between full-pol and hybrid pol are described in [13].

IV. RESULTS

A. Selection Based on Average Coherence

In this section, we compare performance of ESPO and JDPO methods for average coherence optimization, in terms of CPC density, as well as the best combination of channels if full-pol data are not available. As selection criterion, only those points with $|\overline{\gamma}| \geq 0.7$ will be selected as CPC. In order to estimate coherence, a 7×7 multilook is applied (maximum likelihood estimator), which corresponds to an equivalent number of looks (ENL) of approximately 30 (see oversampling factors in Section III). This ENL is expected to provide coherence estimates with standard deviation below 0.06 for coherence values above 0.7 according to the expressions derived in [18]. In order to both minimize spatial and temporal decorrelation effects and to keep a tractable stack size, a 150-m limit for the perpendicular baseline and a 365-day limit for the temporal baseline have been established, resulting in the generation of 137 interferograms from the 31 available images.

As a starting reference, Table I shows CPC selection percentages obtained for each linear, Pauli, and hybrid channel synthesized from the available full-pol data, when no optimization is applied. We can freely combine these channels to define different dual-pol schemes, which correspond to different target vector structures. Table II summarizes CPC selection results obtained by applying the aforementioned optimization methods to some of the most frequent polarimetric schemes. The column labeled as Union corresponds to the algorithm proposed in [15] (also mentioned in Section II-A), applied to each set of available channels (components of $\mathbf{k}$). For the ESPO implementation, an initial coarse search grid with a step of 15° has been employed, followed by a conjugated gradient method.

TABLE II
CPC SELECTED FOR OPTIMIZED DATA CONSIDERING A $\overline{|\gamma|}$ THRESHOLD OF 0.7, FOR DIFFERENT POLARIMETRIC SCHEMES

$\mathbf{k}$	Union	ESPO	JDPO
$[\mathrm{HH}, \mathrm{VV}]^T$	20.08%	26.29%	25.06%
$[\mathrm{HH}, \mathrm{HV}]^T$	21.98%	25.82%	23.20%
$[\mathrm{VV}, \mathrm{VH}]^T$	20.65%	25.22%	22.80%
$[\mathrm{RH}, \mathrm{RV}]^T$	20.43%	26.13%	25.04%
$\frac{1}{\sqrt{2}}[\mathrm{HH}+\mathrm{VV}, \mathrm{HH}-\mathrm{VV}]^T$	22.10%	26.29%	25.01%
$[\mathrm{HH}, \sqrt{2}\mathrm{HV}, \mathrm{VV}]^T$	24.68%	34.65%	31.95%
$\frac{1}{\sqrt{2}}[\mathrm{HH}+\mathrm{VV}, \mathrm{HH}-\mathrm{VV}, 2\mathrm{HV}]^T$	26.41%	34.65%	31.95%

We observe in Table II a significant increase in the number of CPCs selected for the three algorithms considered with respect to Table I. The Union algorithm performs better when Pauli channels are considered. For a dual-pol configuration ($\mathrm{HH}+\mathrm{VV} \cup \mathrm{HH}-\mathrm{VV}$), it gets an increase of about 46% more CPCs in comparison with HH, which is the best single-pol channel. When cross-polar information is added ($\mathrm{HH}+\mathrm{VV} \cup \mathrm{HH}-\mathrm{VV} \cup \mathrm{HV}$), the improvement is about 75% more CPCs selected. In the ESPO case, all the different dual-pol schemes considered lead to similar results, with an important increase of about 75% more CPCs than in single-pol. As for the full-pol configurations, we obtain a dramatic improvement of about 130% with respect to single-pol. For the JDPO approach, dual-pol [HH, HV] and [VV, VH] (Sentinel-1 polarimetric modes) perform slightly worse than the rest of dual-pol configurations tested, but even so the improvement respect to single HH is significant (about 53% increase). Other dual-pol schemes considered lead to an improvement of about 66%, whilst both lexicographic and Pauli full-pol setups get near a 90% increase of density when this algorithm is used.

As expected, the Union algorithm provides a modest improvement in comparison with ESPO and JDPO. ESPO is the one that best maximizes coherence, at the highest computational cost, whilst JDPO appears to be a good tradeoff between processing time and increase of average coherence. We can also observe that the results improve significantly when full-pol data are available, especially for the ESPO algorithm.

At this stage, selected coherent pixel candidates still have to be confirmed as coherent pixels (CPs), i.e., suitable for obtaining valid deformation results. In Section IV-C, we present deformation results for those CPs that survive all the steps of the PSI processing chain.

B. Selection Based on Amplitude Dispersion

In the following, we compare ESPO and MIPO techniques for PSC selection optimization. Table III shows the selection percentages for conventional channels, and Table IV shows the results for the different optimization approaches. In all cases, a threshold of 0.3 has been employed for the amplitude

TABLE III
PSC SELECTED FOR DIFFERENT CHANNELS, CONSIDERING A D_A THRESHOLD OF 0.3

HH	3.99%	RH	4.07%
VV	3.90%	RV	3.97%
HV	3.80%	HH+VV	3.80%
VH	3.80%	HH−VV	4.13%

TABLE IV
PSCs SELECTED FOR OPTIMIZED DATA CONSIDERING A D_A THRESHOLD OF 0.3, FOR DIFFERENT POLARIMETRIC SCHEMES

k	Union	ESPO	MIPO
$[\mathrm{HH}, \mathrm{VV}]^T$	6.48%	12.83%	7.46%
$[\mathrm{HH}, \mathrm{HV}]^T$	6.64%	12.40%	5.87%
$[\mathrm{VV}, \mathrm{VH}]^T$	6.59%	12.71%	6.20%
$[\mathrm{RH}, \mathrm{RV}]^T$	6.62%	13.05%	7.74%
$\frac{1}{\sqrt{2}}[\mathrm{HH}+\mathrm{VV}, \mathrm{HH}-\mathrm{VV}]^T$	6.79%	12.83%	7.46%
$[\mathrm{HH}, \sqrt{2}\mathrm{HV}, \mathrm{VV}]^T$	8.58%	30.75%	10.10%
$\frac{1}{\sqrt{2}}[\mathrm{HH}+\mathrm{VV}, \mathrm{HH}-\mathrm{VV}, 2\mathrm{HV}]^T$	8.88%	30.73%	10.10%

TABLE V
COMPARISON OF CP BEFORE AND AFTER DISCARDING ISOLATED CPC, CONSIDERING A Γ THRESHOLD OF 0.8

k	CP candidates	Final CP
HH	15.09%	13.82%
HV	14.69%	13.45%
JDPO (dual-pol Pauli)	25.01%	22.90%
ESPO (dual-pol Pauli)	26.29%	24.12%
JDPO (full-pol Pauli)	31.95%	29.65%
ESPO (full-pol Pauli)	34.65%	32.12%

TABLE VI
COMPARISON OF PS BEFORE AND AFTER DISCARDING ISOLATED PSC, CONSIDERING A Γ THRESHOLD OF 0.8

k	PS Candidates	Final PS
HH	3.99%	3.64%
HV	3.80%	3.50%
MIPO (dual-pol Pauli)	7.46%	6.98%
ESPO (dual-pol Pauli)	12.83%	9.85%
MIPO (full-pol Pauli)	10.10%	9.69%
ESPO (full-pol Pauli)	30.73%	15.05%

dispersion index. The increase of PSCs in comparison with nonoptimized data is even more spectacular than in previous cases, since single-look data are more sensitive to geometrical features that affect polarimetric response, such as orientation and shape of point-like scatterers.

Looking at the tables, we observe that ESPO clearly outperforms the Union and MIPO algorithms in terms of PSC density. For dual-pol sets, the Union algorithm reaches a significant increase, of about 70%, compared to HH channel, being the set of Pauli channels the most appropriate choice, as in the CPC case shown in Section IV-A. The MIPO algorithm performs slightly better than Union, getting a general increase of about 90% but for the co-polar cross-polar sets [HH, HV] and [VV, VH], which only exhibit around 50% increment. Comparatively, ESPO achieves a much more important density improvement, of about 225% (around 3 times more PSCs). For full-pol sets, performance is significantly higher for all methods, though differences between different approaches become more evident. The Union algorithm shows an improvement of about 120%, and MIPO gets over 150% increment of PSC compared to HH. As for the ESPO approach, we observe a dramatic increase of 670% (almost eight times more PSCs) for both lexicographic and Pauli channel sets. However, as already mentioned in Section II-D, ESPO is characterized by optimizing D_A of both actual PS and clutter, so it can be expected that some of the selected points do not correspond to real dominant point-like scatterers. Consequently, they are likely to be discarded in subsequent steps of the process because of high decorrelation rates. On the other hand, it can still help us in improving the quality of real PS and revealing hidden or masked ones. Consequently, after the presented PSC filtering stage, the total number of valid PS will be significantly higher than for nonoptimized data.

C. Deformation Results

Deformation velocity maps have been generated by following the procedure described in [4], [19]: a network of PSCs (for D_A criterion, full resolution) or CPCs (for $|\overline{\gamma}|$ criterion, degraded resolution) is constructed (usually by Delaunay triangulation), and a phase model is fitted to each link between points by maximizing its model coherence Γ, given by

$$\Gamma = \frac{1}{K}\sum_{k}^{K}\left|e^{j\left(\Delta\phi^k_{\mathrm{dif}}-\Delta\phi^k_{\mathrm{model}}\right)}\right| \tag{13}$$

where $\Delta\phi^k_{\mathrm{dif}}$ stands for the measured interferometric phase difference between connected points, for each interferogram k, and $\Delta\phi^k_{\mathrm{model}}$ is the interferometric phase difference predicted by the model. In our case, we have used a simple phase model that considers linear deformation velocity v_{lin} and digital elevation model error ϵ_{DEM} (both constant for all interferograms).

$$\phi^k_{\mathrm{model}} = \frac{4\pi\, B^k_{\perp}}{\lambda R \sin(\alpha)}\left(\epsilon^i_{\mathrm{DEM}}-\epsilon^j_{\mathrm{DEM}}\right)+\frac{4\pi}{\lambda}T^k\left(v^i_{\mathrm{lin}}-v^j_{\mathrm{lin}}\right) \tag{14}$$

where $B^k_{\perp}$ and T^k are the perpendicular and temporal baselines of interferogram k, respectively, α is the observation angle, R is the sensor–target distance, and λ is the central wavelength of the SAR pulses. Particular details on how to solve this model adjustment problem can be found in [4], [19].

The processing of the PSCs/CPCs follows a multilayer scheme [19] that allows higher quality points to be processed first and then used to improve the estimates of subsequent layers of lower quality pixels. For PSCs, three selection layers are considered, with D_A thresholds of 0.1, 0.2, and 0.3, respectively. For CPCs, we considered just two layers, with thresholds of 0.8 and 0.7. In addition, a threshold for Γ can be introduced so that links whose behavior differs significantly

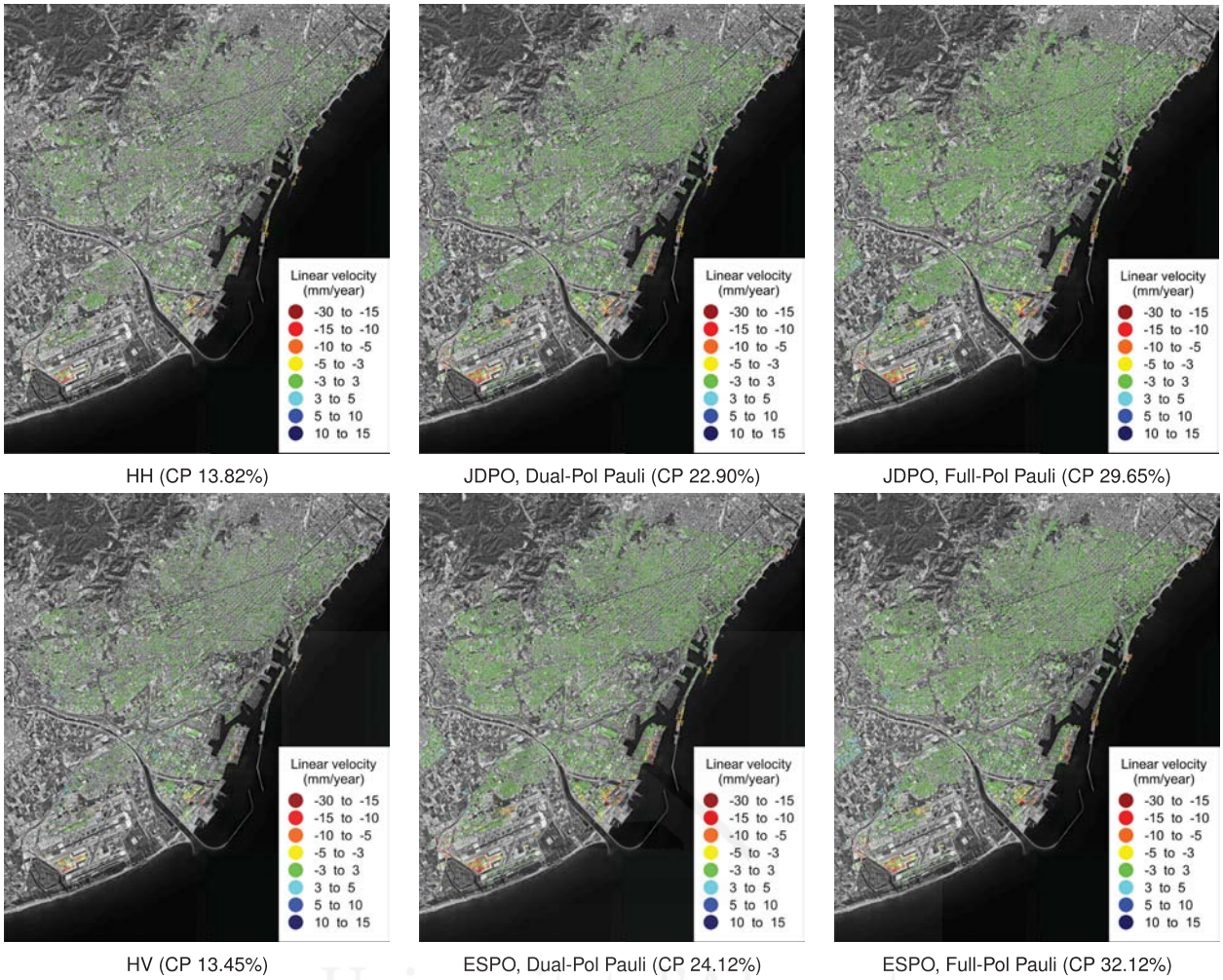

Fig. 2. Deformation velocity maps obtained for different polarimetric channels from coherent points (degraded resolution, multilook 7 × 7).

from the model are removed. In this paper, links below a Γ value of 0.8 are discarded. PSCs and CPCs that become isolated (i.e., not connected to other PSCs or CPCs via quality links) will not be considered suitable for processing, whilst the rest of pixel candidates will be confirmed as valid PS or CP. Tables V and VI show a comparison of selection percentages before and after removing isolated pixel candidates, for some channels. Notice that we could avoid discarding some of the candidates by adding redundancy to the pixels network, e.g., by considering all the possible links between points inside a given radius instead of using Delaunay triangulation, but with higher computational cost and memory requirements.

Figs. 2 and 3 show deformation velocity maps obtained for CP-based and PS-based approaches, respectively. For reasons of brevity, only some representative channels are shown: HH (best performing copolar channel), HV (crosspolar channel), MIPO, ESPO, and JDPO optimum channels, obtained from both dual-pol and full-pol Pauli channel sets. Percentage of valid CP and PS is shown for comparison with preliminary selection results of CPC and PSC. The increase of the area with deformation information provided by PSI is evident for both criteria considered when more than one channel is used.

Most of the previously selected pixels are confirmed as CP for the coherence criterion, for both JDPO and ESPO (around 90% of previously selected CPC). It is also important to point out that, for single-pol data, the ratio between CPCs and surviving CPs is similar to that of optimized data. As for the amplitude dispersion criterion, we observe that a large number of points selected for ESPO-optimized data are discarded by the posterior processing stages: 77% of PSC are confirmed as PS for dual-pol, and only 49% in the case of full-pol data. However, the density of remaining PS still surpasses that obtained by the other techniques, getting an effective increase of about 2.7 times more PS than conventional channels for dual-pol input data, and 4.1 times more density when full-pol data are made available. At a much lower computational cost, MIPO achieves an effective increase of more than twice the number of PS for dual-pol data, and about 2.7 times increment in the case of full-pol, with around 95% of PSCs confirmed as PS.

Deformation maps describe similar features to those shown in [9] presentation slides, obtained from the first 15 images (Jan.–Dec. 2010) of the same Radarsat-2 dataset used in this paper. Figs. 4 and 5 show an augmented view of the

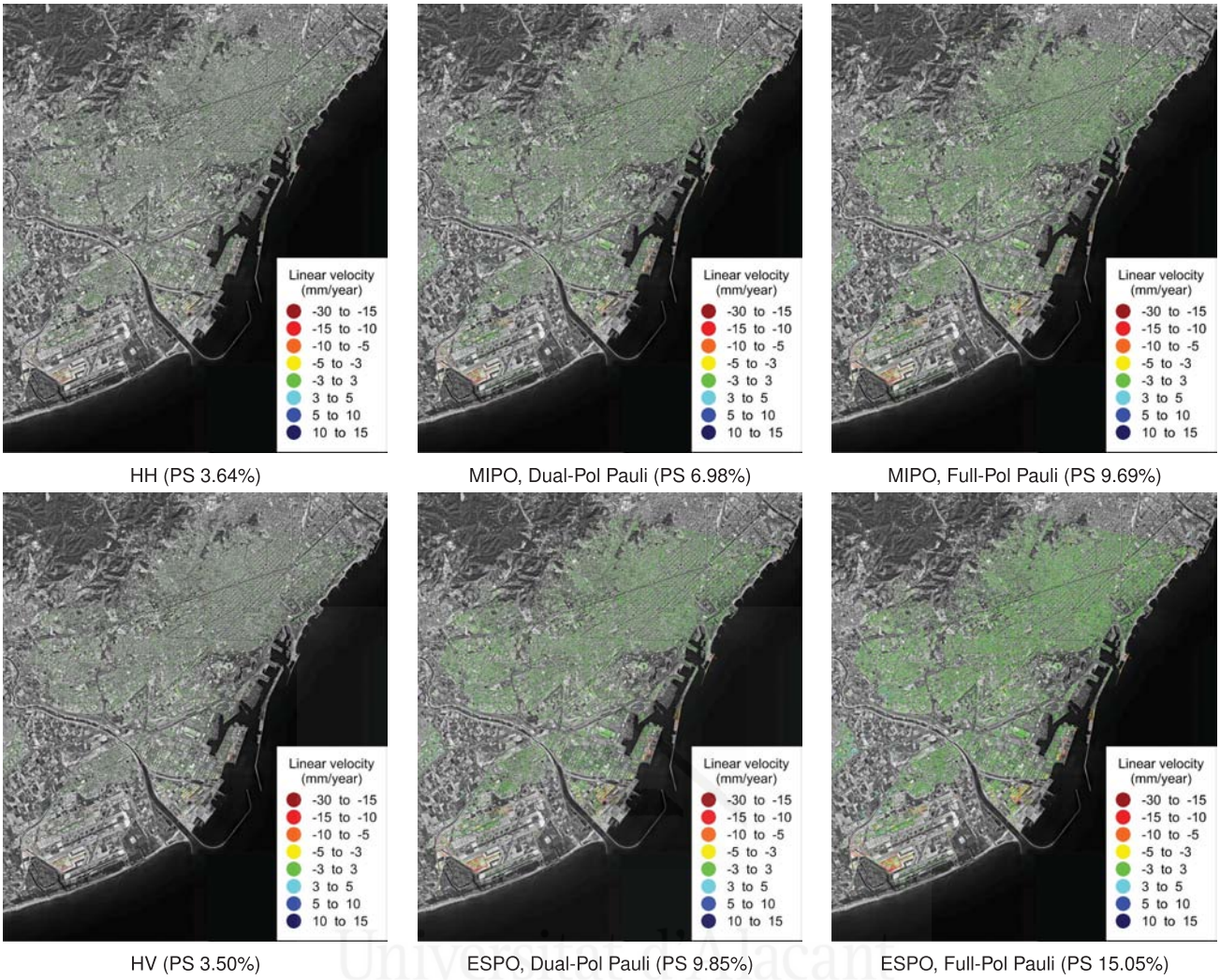

Fig. 3. Deformation velocity maps obtained for different polarimetric channels from persistent scatterers (full resolution).

deformation velocity maps centered in the area of "El Prat" airport, for both CP and PS approaches. We can observe how optimization reveals new details, such as the southern runway, which are not present in the HH or HV maps but shown as stable in the optimized CP maps. Buildings deformation is also described in a much precise way, especially for D_A optimized data. We can compare the results obtained for this location with those presented in [20] for TerraSAR-X single-pol data. A great degree of correspondence is observed, though the exact period of study in that reference is not specified.

The total increase in the number of pixels provided by polarimetry in this application presents two advantages. First, the spatial coverage of the deformation maps is larger, covering wider areas and revealing details that were not present in results obtained with single-pol data. Second, the networks formed by pixels candidates are denser, thereby making more robust the computation of the model fitting and the rest of signal processing and, consequently, improving the accuracy of the final deformation estimates.

It is also important to note that the cross-polar channel, HV, usually related to random volume scattering over natural surfaces, is also providing reliable deformation maps in this urban area, with a density of CP comparable to HH and superior in the case of PS. As a matter of fact, in the composite RGB image (Fig. 1), a significant cross-polar response (green channel) from urbanized areas is observed. As already mentioned in Section III, this can be explained by the strong cross-polar response from tilted dihedrals (oriented buildings). Therefore, availability of this information is an important factor for the completeness of the area description.

V. Conclusion

In this paper, new polarimetric PSI optimization approaches have been presented and evaluated for different dual-pol and full-pol sets synthesized from Radarsat-2 fully polarimetric data. All presented approaches succeeded in increasing the density of selected stable pixels, and hence the density of pixels with valid deformation results with respect to single-pol data.

For techniques based on selection by average coherence (coherent pixels, degraded resolution), the ESPO approach is the one that provides the largest improvement, with an increase of CP density of around 75% for dual-pol data, and approximately 130% for full-pol data, after discarding

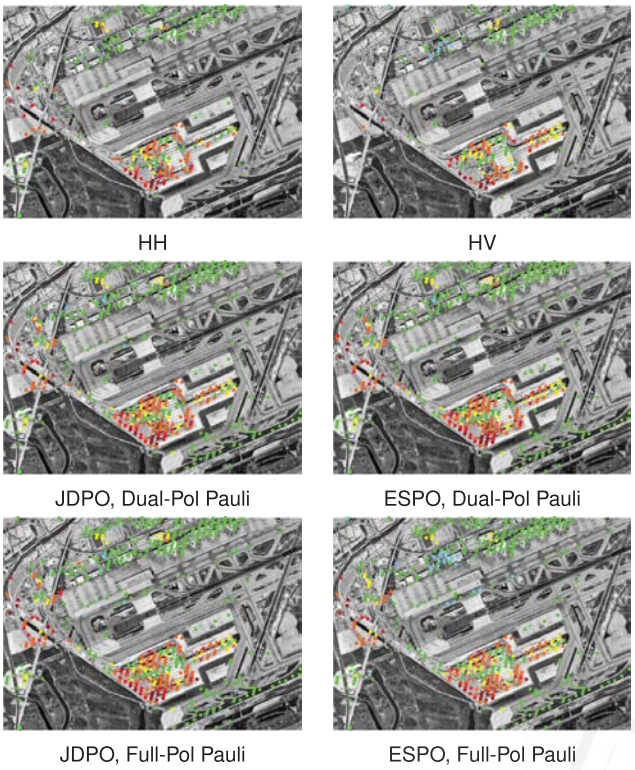

Fig. 4. Detail of deformation velocity maps (Barcelona—"El Prat" airport) obtained from coherent points. The same color scale as in Fig. 2 is used.

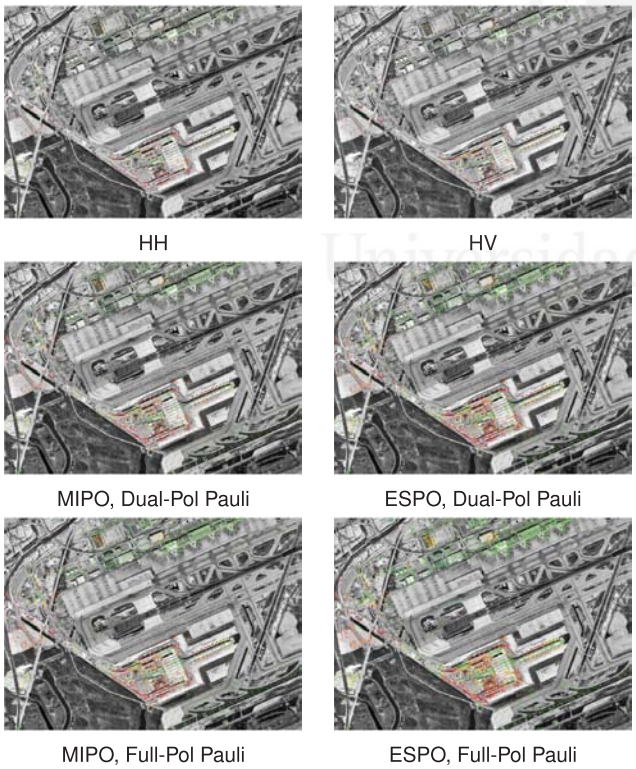

Fig. 5. Detail of deformation velocity maps (Barcelona—"El Prat" airport) obtained from persistent scatterers. The same color scale as in Fig. 3 is used.

nonvalid CPC. The Union algorithm and JDPO also provide a significant improvement at a lower computational cost. As for methods based in amplitude dispersion criterion (persistent scatterers, full-resolution), the ESPO approach is also the best performing method, with increases of PS density of around 170% (almost 3 times more PS) for dual-pol sets, and around 310% (over 4 times more PS) with respect to single-pol, after nonvalid PSC are discarded.

From the non-full-pol sets considered, dual-pol Pauli and hybrid-pol data are the best choices for all of the studied approaches, both CP-based and PS-based. However, notice that, in order to generate Pauli channels, we need a dual-pol SAR system capable of providing coherent measures of HH and VV. Unlike dual-pol and compact-pol systems, sensors gathering [HH, VV] bear the same requirements as full-pol in terms of PRF and reduced swath, since they require multiplexed transmission of horizontal and vertical polarizations. Consequently, hybrid-pol would be the preferred option when full-pol data are not available.

As a future research line, detection and interpretation of multiple stable scattering mechanisms within the same resolution cell will be addressed.

Appendix I
Whitening and Unwhitening Transformations

Relationship between projection vectors in the original and whitened basis is given by (8) and (9). Equation (8) can be easily demonstrated by substitution into (6)

$$\begin{aligned}\tilde{\gamma}_k(\tilde{\boldsymbol{\omega}}_i,\tilde{\boldsymbol{\omega}}_j) &= \tilde{\boldsymbol{\omega}}_i^{\dagger}\tilde{\boldsymbol{\Omega}}_{ij}\tilde{\boldsymbol{\omega}}_j \\ &= \tilde{\boldsymbol{\omega}}_i^{\dagger}\mathbf{T}_{ii}^{-\frac{1}{2}}\boldsymbol{\Omega}_{ij}\mathbf{T}_{jj}^{-\frac{1}{2}}\tilde{\boldsymbol{\omega}}_j \\ &= \left(\frac{\mathbf{T}_{ii}^{\frac{1}{2}}\boldsymbol{\omega}_i}{\sqrt{\boldsymbol{\omega}_i^{\dagger}\mathbf{T}_{ii}\boldsymbol{\omega}_i}}\right)^{\dagger}\mathbf{T}_{ii}^{-\frac{1}{2}}\boldsymbol{\Omega}_{ij}\mathbf{T}_{jj}^{-\frac{1}{2}}\frac{\mathbf{T}_{jj}^{\frac{1}{2}}\boldsymbol{\omega}_j}{\sqrt{\boldsymbol{\omega}_j^{\dagger}\mathbf{T}_{jj}\boldsymbol{\omega}_j}} \\ &= \frac{\boldsymbol{\omega}_i^{\dagger}\mathbf{T}_{ii}^{\frac{1}{2}}\mathbf{T}_{ii}^{-\frac{1}{2}}\boldsymbol{\Omega}_{ij}\mathbf{T}_{jj}^{-\frac{1}{2}}\mathbf{T}_{jj}^{\frac{1}{2}}\boldsymbol{\omega}_j}{\sqrt{\boldsymbol{\omega}_i^{\dagger}\mathbf{T}_{ii}\boldsymbol{\omega}_i}\sqrt{\boldsymbol{\omega}_j^{\dagger}\mathbf{T}_{jj}\boldsymbol{\omega}_j}} \\ &= \frac{\boldsymbol{\omega}_i^{\dagger}\boldsymbol{\Omega}_{ij}\boldsymbol{\omega}_j}{\sqrt{\boldsymbol{\omega}_i^{\dagger}\mathbf{T}_{ii}\boldsymbol{\omega}_i}\sqrt{\boldsymbol{\omega}_j^{\dagger}\mathbf{T}_{jj}\boldsymbol{\omega}_j}} = \gamma_k(\boldsymbol{\omega}_i,\boldsymbol{\omega}_j) \end{aligned} \tag{15}$$

and similarly, by substitution of (9) into (3) we obtain

$$\begin{aligned}\gamma_k(\boldsymbol{\omega}_i,\boldsymbol{\omega}_j) &= \frac{\boldsymbol{\omega}_i^{\dagger}\boldsymbol{\Omega}_{ij}\boldsymbol{\omega}_j}{\sqrt{\boldsymbol{\omega}_i^{\dagger}\mathbf{T}_{ii}\boldsymbol{\omega}_i}\sqrt{\boldsymbol{\omega}_j^{\dagger}\mathbf{T}_{jj}\boldsymbol{\omega}_j}} \\ &= \frac{\left(\frac{\mathbf{T}_{ii}^{-\frac{1}{2}}\tilde{\boldsymbol{\omega}}_i}{a}\right)^{\dagger}\boldsymbol{\Omega}_{ij}\frac{\mathbf{T}_{jj}^{-\frac{1}{2}}\tilde{\boldsymbol{\omega}}_j}{b}}{\sqrt{\frac{\mathbf{T}_{ii}^{-\frac{1}{2}}\tilde{\boldsymbol{\omega}}_i}{a}^{\dagger}\mathbf{T}_{ii}\frac{\mathbf{T}_{ii}^{-\frac{1}{2}}\tilde{\boldsymbol{\omega}}_i}{a}}\sqrt{\frac{\mathbf{T}_{jj}^{-\frac{1}{2}}\tilde{\boldsymbol{\omega}}_j}{b}^{\dagger}\mathbf{T}_{jj}\frac{\mathbf{T}_{jj}^{-\frac{1}{2}}\tilde{\boldsymbol{\omega}}_j}{b}}} \\ &= \frac{(ab)^{-1}\tilde{\boldsymbol{\omega}}_i^{\dagger}\mathbf{T}_{ii}^{-\frac{1}{2}}\boldsymbol{\Omega}_{ij}\mathbf{T}_{jj}^{-\frac{1}{2}}\tilde{\boldsymbol{\omega}}_j}{(ab)^{-1}\sqrt{\tilde{\boldsymbol{\omega}}_i^{\dagger}\mathbf{T}_{ii}^{-\frac{1}{2}}\mathbf{T}_{ii}\mathbf{T}_{ii}^{-\frac{1}{2}}\tilde{\boldsymbol{\omega}}_i}\sqrt{\tilde{\boldsymbol{\omega}}_j^{\dagger}\mathbf{T}_{jj}^{-\frac{1}{2}}\mathbf{T}_{jj}\mathbf{T}_{jj}^{-\frac{1}{2}}\tilde{\boldsymbol{\omega}}_j}} \\ &= \tilde{\boldsymbol{\omega}}_i^{\dagger}\mathbf{T}_{ii}^{-\frac{1}{2}}\boldsymbol{\Omega}_{ij}\mathbf{T}_{jj}^{-\frac{1}{2}}\tilde{\boldsymbol{\omega}}_j = \tilde{\boldsymbol{\omega}}_i^{\dagger}\tilde{\boldsymbol{\Omega}}_{ij}\tilde{\boldsymbol{\omega}}_j = \tilde{\gamma}_k(\tilde{\boldsymbol{\omega}}_i,\tilde{\boldsymbol{\omega}}_j) \end{aligned} \tag{16}$$

with $a = \sqrt{\tilde{\boldsymbol{\omega}}_i^{\dagger} \mathbf{T}_{ii}^{-1} \tilde{\boldsymbol{\omega}}_i}$ and $b = \sqrt{\tilde{\boldsymbol{\omega}}_j^{\dagger} \mathbf{T}_{jj}^{-1} \tilde{\boldsymbol{\omega}}_j}$. In order to ensure the generality of this equation, no ESM constraint has been considered.

ACKNOWLEDGMENT

The authors would like to thank Prof. J. Mallorquí Universitat Politècnica de Catalunya for providing access to the Radarsat-2 data. Ortophotos were provided by the Spanish Ministerio de Agricultura, Alimentación y Medio Ambiente (MAAMA). All Radarsat-2 images have been provided by MDA and CSA in the framework of project SOAR-EU 6779.

REFERENCES

[1] A. Ferretti, C. Prati, and F. Rocca, "Nonlinear subsidence rate estimation using permanent scatterers in differential SAR interferometry," *IEEE Trans. Geosci. Remote Sens.*, vol. 38, no. 5, pp. 2202–2212, Sep. 2000.

[2] A. Ferretti, C. Prati, and F. Rocca, "Permanent scatterers in SAR interferometry," *IEEE Trans. Geosci. Remote Sens.*, vol. 39, no. 1, pp. 8–20, Jan. 2001.

[3] P. Berardino, G. Fornaro, R. Lanari, and E. Sansosti, "A new algorithm for surface deformation monitoring based on small baseline differential SAR interferograms," *IEEE Trans. Geosci. Remote Sens.*, vol. 40, no. 11, pp. 2375–2383, Nov. 2002.

[4] O. Mora, J. J. Mallorquí, and A. Broquetas, "Linear and nonlinear terrain deformation maps from a reduced subset of interferometric SAR images," *IEEE Trans. Geosci. Remote Sens.*, vol. 41, no. 10, pp. 2243–2253, Nov. 2003.

[5] A. Ferretti, A. Fumagali, F. Novali, C. Prati, F. Rocca, and A. Rucci, "A new algorithm for processing interferometric data-stacks: SqueeSAR," *IEEE Trans. Geosci. Remote Sens.*, vol. 49, no. 9, pp. 3460–3470, Sep. 2011.

[6] V. D. Navarro-Sanchez, J. M. Lopez-Sanchez, and F. Vicente-Guijalba, "A contribution of polarimetry to satellite differential SAR interferometry: Increasing the number of pixel candidates," *IEEE Geosci. Remote Sens. Lett.*, vol. 7, no. 2, pp. 276–280, Apr. 2010.

[7] V. D. Navarro-Sanchez and J. M. Lopez-Sanchez, "Improvement of persistent-scatterer interferometry performance by means of a polarimetric optimization," *IEEE Geosci. Remote Sens. Lett.*, vol. 9, no. 4, pp. 609–613, Jul. 2012.

[8] L. Ferro-Famil, M. Neumann, and Y. Huang, "Multi-baseline POL-InSAR statistical techniques for the characterization of distributed media," in *Proc. IEEE Int. Geosci. Remote Sens. Symp.*, Jul. 2009, pp. 971–974.

[9] D. Monells, J. Mallorqui, G. Centolanza, and C. Lopez-Martinez, "Application of polarimetric techniques in DInSAR processing for space borne monitoring," in *Proc. PolinSAR*, Jan. 2011, pp. 1–19.

[10] P. Dheenathayalan and R. Hanssen, "Target characterization and interpretation of deformation using persistent scatterer interferometry and polarimetry," in *Proc. PolinSAR*, Jan. 2011, pp. 1–3.

[11] K. Raney, "Hybrid-polarity SAR architecture," *IEEE Trans. Geosci. Remote Sens.*, vol. 45, no. 11, pp. 3397–3404, Nov. 2007.

[12] S. R. Cloude and K. P. Papathanassiou, "Polarimetric SAR interferometry," *IEEE Trans. Geosci. Remote Sens.*, vol. 36, no. 5, pp. 1551–1565, Sep. 1998.

[13] S. R. Cloude, *Polarisation: Applications in Remote Sensing*. Oxford, U.K.: Oxford University Press, 2010.

[14] M. Neumann, L. Ferro-Famil, and A. Reigber, "Multibaseline polarimetric sar interferometry coherence optimization," *IEEE Geosci. Remote Sens. Lett.*, vol. 1, no. 5, pp. 93–97, Jan. 2008.

[15] L. Pipia, X. Fabregas, A. Aguasca, C. López-Martínez, S. Duque, J. J. Mallorquí, and J. Marturià, "Polarimetric differential SAR interferometry: First results with ground-based measurements," *IEEE Geosci. Remote Sens. Lett.*, vol. 6, no. 1, pp. 167–171, Jan. 2009.

[16] J. F. Cardoso and A. Souloumiac, "Jacobi angles for simultaneous diagonalization," *SIAM J. Math. Anal. Appl.*, vol. 17, no. 1, pp. 161–164, Jan. 1996.

[17] Z. Shan, H. Zhang, C. Wang, W. An, T. Wu, and X. Chen, "Four-component model-based decomposition of polarimetric SAR data for special ground objects," *IEEE Geosci. Remote Sens. Lett.*, vol. 9, no. 5, pp. 989–993, Sep. 2012.

[18] R. Touzi, A. Lopes, J. Bruniquel, and W. P. Vachon, "Coherence estimation for SAR imagery," *IEEE Trans. Geosci. Remote Sens.*, vol. 37, no. 1, pp. 135–148, Jan. 1999.

[19] P. Blanco-Sanchez, J. J. Mallorqui, S. Duque, and D. Monells, "The coherent pixels technique (CPT): An advanced DInSAR technique for nonlinear deformation monitoring," *Pure Appl. Geophys.*, vol. 165, no. 6, pp. 1167–1193, Jun. 2008.

[20] O. Monserrat, M. Crossetto, M. Cuevas, and B. Crippa, "The thermal expansion component of persistent scatterer interferometry observations," *IEEE Geosci. Remote Sens. Lett.*, vol. 8, no. 5, pp. 864–868, Sep. 2011.

Victor D. Navarro-Sanchez (S'09) was born in Caravaca de la Cruz, Murcia, Spain, in 1982. He received the Ingeniero Técnico degree in telecommunication engineering from the University of Alicante, Alicante, Spain, in 2004, the Ingeniero degree in telecommunication engineering from the University Miguel Hernández, Elche, Spain, in 2009, and the Official's Master degree in computer technologies from the University of Alicante, Alicante, in 2010.

He has been a Pre-Doctoral Fellow with the Signals, Systems and Telecommunication Group, University of Alicante, since 2009. His current research interests include polarimetric and interferometric SAR methods for urban and natural environments monitoring and classification.

Juan M. Lopez-Sanchez (S'94–M'00–SM'05) was born in Alicante, Spain, in 1972. He received the Ingeniero and Doctor Ingeniero degrees in telecommunication engineering from the Technical University of Valencia, Valencia, Spain, in 1996 and 2000, respectively.

He was a Pre-Doctoral Fellow with the Space Applications Institute, Joint Research Centre of the European Commission, Ispra, Italy, from 1998 to 1999. Since 2000, he has led the Signals, Systems and Telecommunication Group, University of Alicante, Alicante, Spain, where he has been a Professor since November 2011. He has co-authored more than 40 papers in refereed journals and more than 80 papers and presentations in international conferences and symposia. His current research interests include microwave remote sensing for inversion of biophysical parameters, polarimetric and interferometric techniques, SAR imaging algorithms, and analytical and numerical models for multiple scattering problems.

Dr. Lopez-Sanchez was the recipient of the INDRA Award for the best Ph.D. thesis on radar in Spain in 2001. From 2006 to 2012, he was the Chair of the Spanish Chapter of the IEEE Geoscience and Remote Sensing Society.

Laurent Ferro-Famil (S'99–A'00–M'04) received the Laurea degree in electronics systems and computer engineering, and the M.S. degree and Ph.D. degrees from the University of Nantes, Nantes, France, in 1996, 1996, and 2000, respectively, both in electronics.

He was an Associate Professor in 2001 and he has been a full Professor with the University of Rennes 1, Rennes, France, since 2011, where he is currently the Head of the Remote Sensing Department, Institute of Electronics and Telecommunications of Rennes. His current activities in education are concerned with analog electronics, digital communications, microwave theory, signal processing, and polarimetric SAR remote sensing. His current research interests include polarimetric SAR signal statistical processing, radar polarimetry theory, and natural media remote sensing using multibaseline PolInSAR data, with application to classification, electromagnetic scattering modeling and physical parameter retrieval, time-frequency analysis, and 3-D reconstruction of environments using tomography.

3.4 Spatial Adaptive Speckle Filtering Driven by Temporal Polarimetric Statistics and Its Application to PSI

Spatial Adaptive Speckle Filtering Driven by Temporal Polarimetric Statistics and Its Application to PSI

Victor D. Navarro-Sanchez, *Student Member, IEEE*, and Juan M. Lopez-Sanchez, *Senior Member, IEEE*

***Abstract*—Persistent scatterer (PS) interferometry (PSI) techniques are designed to measure ground deformations using satellite synthetic aperture radar (SAR) data. They rely on the identification of pixels not severely affected by spatial or temporal decorrelation, which, in general, correspond to pointlike PSs commonly found in urban areas. However, in urban areas, we can find not only PSs but also distributed scatterers (DSs) whose phase information may be exploited for PSI applications. Estimation of DS parameters requires speckle filtering to be applied to the complex SAR data, but conventional speckle filtering approaches tend to mask PS information due to spatial averaging. In the context of single-polarization PSI, adaptive speckle filtering strategies based on the exploitation of amplitude temporal statistics have been proposed, which seek to avoid spatial filtering on nonhomogeneous areas. Given the growing interest on polarimetric PSI techniques, i.e., those using polarimetric diversity to increase performance over conventional single-polarization PSI, in this paper, we propose an adaptive spatial filter driven by polarimetric temporal statistics, rather than single-polarization amplitudes. The proposed approach is able to filter DS while preserving PS information. In addition, a new methodology for the joint processing of PS and DS in the context of PSI is introduced. The technique has been tested for two different urban data sets: 41 dual-polarization TerraSAR-X images of Murcia (Spain) and 31 full-polarization Radarsat-2 images of Barcelona (Spain). Results show an important improvement in terms of number of pixels with valid deformation information, hence denser area coverage.**

***Index Terms*—Persistent scatterers (PSs), polarimetry, speckle, subsidence, synthetic aperture radar (SAR) interferometry.**

I. Introduction

ONE of the major sources of error inherent to any synthetic aperture radar (SAR) system is speckle, produced by the mutual interference of coherent electromagnetic waves when reflected by different elements contained in the resolution cell. Speckle behaves as a granular random noise and is generally reduced by using spatial filtering. However, spatial filtering comes at the cost of resolution loss. In addition, the conventional fixed-size sliding-window filters may not be suitable for heterogeneous areas, such as urban environments, where preserving the maximum level of detail is desirable.

Persistent scatterer (PS) interferometry (PSI) techniques are extensively used for subsidence monitoring of urban areas. They are based on the analysis of the interferometric phase of pixels that satisfy some stability requirements during the observation period. Most PSI techniques aim to identify stable pointlike scatterers, usually referred to as PSs, which are generally associated with reflections from man-made structures. However, urban areas are complex environments where we can also find distributed scatterers (DSs), i.e., groups of neighboring pixels sharing similar reflectivity properties that may be considered as part of the same target. Therefore, a methodology which allows the joint processing of PS and DS would be advantageous. We must take into account that, while speckle filtering can contribute to a better characterization of DS, too aggressive filtering strategies may lead to the loss of information on pointlike PS. Consequently, an adaptive filtering approach is the option of choice for PSI.

So far, a number of speckle filtering approaches have been proposed in the literature [1]–[4] that use spatial statistics to adapt the shape and size of the sliding window, so that only homogeneous connected areas are averaged. The estimation of spatial statistics for a given coordinate generally implies to evaluate a significant number of neighboring samples. Small vicinity windows can lead to biased estimates, while larger windows incur the risk of mixing statistically nonhomogeneous areas, so a tradeoff is required. In either case, response from PS will be masked or corrupted by the rest of the samples in the set.

In order to avoid resolution loss, adaptive speckle filtering approaches based on the analysis of temporal statistics, such as DespecKS [5], have been introduced in the framework of single-polarization PSI. The DespecKS algorithm makes use of the two-sample Kolmogorov–Smirnov (KS) test to evaluate whether two neighboring pixels have amplitude data drawn from the same probability density function (pdf), and thus, they can be considered statistically homogeneous pixels (SHPs). The amplitude pdf of a pixel is estimated from the amplitude values at all acquisition times, so no spatial averaging is required. Note that other statistical tests can be applied [6]. However, the extension of DespecKS to multichannel (polarimetric) data can be problematic, since it requires the estimation of a multivariate pdf, which, in general, is not straightforward and requires a significantly larger number of samples. In addition, the KS test

Manuscript received February 13, 2013; revised July 17, 2013; accepted September 14, 2013. This work was supported in part by the Spanish Ministerio de Economía y Competitividad and in part by the European Union FEDER funds under Project TEC2011-28201-C02-02.

The authors are with the Signals, Systems and Telecommunication Group, Escuela Politécnica Superior, University of Alicante, 03080 Alicante, Spain (e-mail: victor.navarro@ieee.org; juanma-lopez@ieee.org).

Color versions of one or more of the figures in this paper are available online at http://ieeexplore.ieee.org.

Digital Object Identifier 10.1109/TGRS.2013.2282406

is suited to real data (such as the amplitude), which implies making some assumptions when dealing with complex data (e.g., amplitude stability indicates phase stability).

In this paper, a polarimetric adaptive filter driven by temporal statistics is proposed. The filter relies on a likelihood ratio test for equality of complex Wishart matrices [7] to determine if two temporal sample coherency matrices (as defined in Section II) are drawn from the same distribution. In addition, a methodology for the joint processing of PS and DS is proposed.

The filter has been tested on an urban area for dual-polarization TerraSAR-X data (Murcia, Spain), as well as for full-polarization Radarsat-2 data (Barcelona, Spain). Deformation velocity maps have been obtained, showing an important improvement in terms of density of pixels with valid deformation information, in comparison with not filtered data, thus confirming the suitability of the approach for its use on PSI.

II. Formulation

A. Polarimetric Homogeneity Test

In [8], a likelihood ratio test was used to assess polarimetric stationarity of an area over time. Now, we use a similar approach to check if two polarimetric coherency matrices associated with neighboring pixels follow the same distribution, and therefore, they can be considered polarimetrically homogeneous pixels (PHPs).

Let $\mathbf{k}$ be the q-dimensional target vector obtained by projecting scattering matrix $\mathbf{S}$ of a pixel onto the Pauli basis, as defined in [9]. For full-polarization data $(q = 3)$, it is given by

$$\mathbf{k} = \frac{1}{\sqrt{2}} \begin{bmatrix} HH + VV \\ HH - VV \\ 2HV \end{bmatrix} \tag{1}$$

where HH and VV stand for the horizontal and vertical co-polar channels, respectively, and HV is the cross-polar channel. Notice that we assume that $HV = VH$ due to reciprocity. In the case of dual-polarization data $(q = 2)$ with no cross-polarization information, the target vector is reduced to

$$\mathbf{k} = \frac{1}{\sqrt{2}} \begin{bmatrix} HH + VV \\ HH - VV \end{bmatrix}. \tag{2}$$

Let us consider a set of N samples of $\mathbf{k}$ obtained for the same pixel coordinates at different dates, i.e., from different SAR images. We can define their $q \times q$ sample temporal coherency matrix $\mathbf{T}$ as

$$\mathbf{T} = \frac{1}{N} \sum_{n=1}^{N} \mathbf{k}_n \cdot \mathbf{k}_n^{\dagger} \tag{3}$$

where † stands for the Hermitian or conjugate transpose. Under the assumption that, along the stack of N images, $\mathbf{k}$ follows a zero-mean circular complex multivariate Gaussian distribution, denoted as $\mathbf{k} \sim \mathcal{N}_q^{\mathbb{C}}(0, \mathbf{\Sigma})$, the corresponding sample coherency matrix $\mathbf{T}$ follows a complex Wishart distribution with N degrees of freedom $\mathbf{T} \sim \mathcal{W}_q^{\mathbb{C}}(N, \mathbf{\Sigma})$. Notice that no spatial averaging is required at this point to compute $\mathbf{T}$, since samples are obtained from the temporal dimension.

Two pixels i and j will be considered PHPs if their associated sample coherence matrices $\mathbf{T}_i$ and $\mathbf{T}_j$ follow the same distribution, i.e., they verify the hypothesis $\mathbf{\Sigma}_i = \mathbf{\Sigma}_j$. This hypothesis can be verified, as proposed in [7] and [10], by means of a likelihood ratio test. Likelihood ratio can be obtained from the determinants of the sample coherence matrices as follows:

$$\Lambda = \frac{|\mathbf{T}_i|^{N_i} |\mathbf{T}_j|^{N_j}}{\left| \frac{N_i \mathbf{T}_i + N_j \mathbf{T}_j}{N_i + N_j} \right|^{N_i + N_j}} \tag{4}$$

where Λ is the likelihood ratio and N_i and N_j indicate the number of target vector samples used to compute $\mathbf{T}_i$ and $\mathbf{T}_j$, respectively (generally, $N_i = N_j = N$). Two pixels are considered PHPs, with an arbitrarily chosen probability of false alarm P_{fa} if

$$\Lambda > c_\beta \qquad P_{\mathrm{fa}}(c_\beta) = P(\Lambda \leq c_\beta) = \beta. \tag{5}$$

Expression (5) requires the formulation of $P_{\mathrm{fa}}(c_\beta)$, which cannot be obtained analytically in an easy way. However, an approximated expression for $P_{\mathrm{fa}}(c_\beta)$ has been derived in [7] and [10]. For a two-pixel test with $N_i = N_j = N$, the probability may be expressed as

$$\begin{aligned} P_{\mathrm{fa}}(c_\beta) = 1 &- \gamma_{\mathrm{inc}}\left(q^2/2, -\rho \log(c_\beta)\right) \\ &- \omega_2 \left[\gamma_{\mathrm{inc}}\left(q^2/2 + 2, -\rho \log(c_\beta)\right)\right. \\ &\left. - \gamma_{\mathrm{inc}}\left(q^2/2, -\rho \log(c_\beta)\right)\right] \end{aligned} \tag{6}$$

with

$$\rho = 1 - \frac{2q^2 - 1}{4qN} \tag{7}$$

$$\omega_2 = \frac{q^2}{4\rho^2} \left(\frac{q^2 - 1}{6} \left(\frac{2}{N^2} - \frac{1}{(2N)^2} \right) - (1 - \rho)^2 \right) \tag{8}$$

where $\gamma_{\mathrm{inc}}(a, b)$ represents the incomplete gamma function of b at order a.

Similar to the DespecKS algorithm described in [5] for single-polarization data, the proposed polarimetric homogeneity test will be performed for each pixel on all the surrounding pixels inside a previously defined range or window. The pixel under analysis and all its PHP neighbors define the pixel's parameter estimation window (PEW). Pixels that pass the test but are not connected to the pixel under analysis either directly or through other PHPs will be discarded to reduce the probability of mixing responses from different radar targets. In this work, a 15×15 test window centered on the pixel has been considered.

To determine whether a pixel should be treated as part of a DS or as an isolated pixel, we apply a criterion based on the size of the pixel's PEW L (number of spatial looks). Pixels with L smaller than a certain number of samples R will be considered isolated pixels for processing, hence suitable for PS analysis. On the other hand, pixels with a sufficiently large PEW $(L \geq R)$ will be considered suitable for DS parameter estimation. Fig. 1 shows an example of the number of PHPs (L) identified for each pixel over the area of Barcelona, obtained with the set of 31 Radarsat-2 images described in Section III.

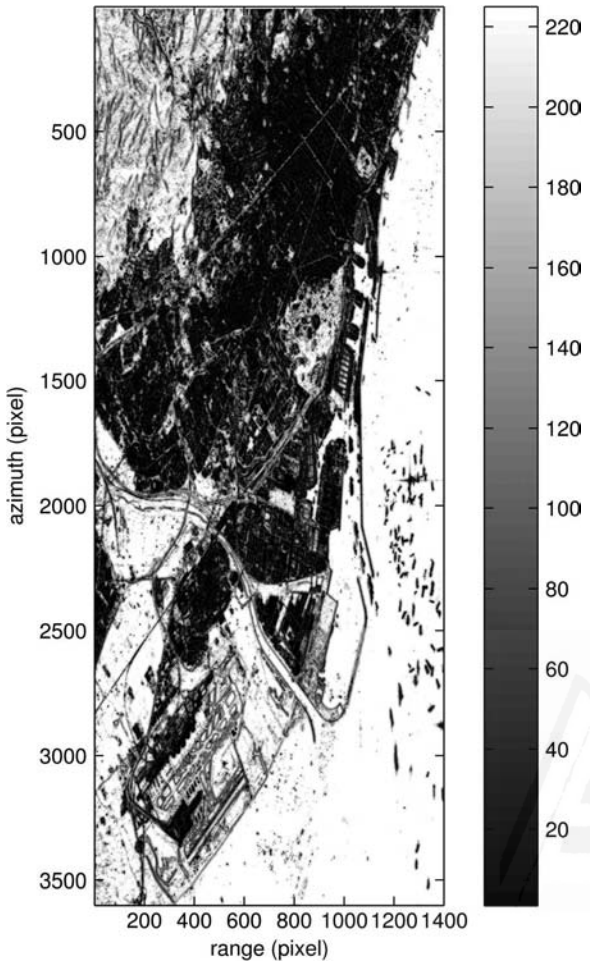

Fig. 1. Number of identified PHPs in Barcelona (Spain), for a $\log \Lambda$ threshold of -20 and a test window of 15×15.

Brighter areas correspond to polarimetrically homogeneous regions according to the test. The original test has been replaced by an equivalent one given by $\log \Lambda > \log c_\beta$, and an arbitrary threshold of $\log \Lambda > -20$ has been set, which ensures $P_{\text{fa}} < 1\%$. An interesting feature of the proposed test is its great sensitiveness to the presence of dominant scatterers, even if they only appear in some images (such as boats in the sea). Hence, pixels dominated by this kind of strong scatterers are generally treated as isolated targets, which is the desired behavior for our application.

The likelihood ratio test (also known as Box's test) is known to perform incorrectly in some cases. To begin with, as aforementioned, this test relies on the assumption that $\mathbf{T}$ samples follow a centered Wishart distribution, so it may fail when this hypothesis does not hold. In particular, in the case of PS, the assumption that $\mathbf{k}$ samples are zero-mean Gaussian distributed in time is generally not true. More robust versions of the test have been proposed in the literature, which account for departure from normality [11], [12]. The test is also known to be biased when the number of samples (N) is small with respect to the number of dimensions (q). Alternative asymptotic approximations to the distribution of the likelihood ratio test statistic, for the estimation of P_{fa}, can be found in [13]. Nevertheless, from our experience, this simple version of the test provides significantly good results in most cases of study. Experiments

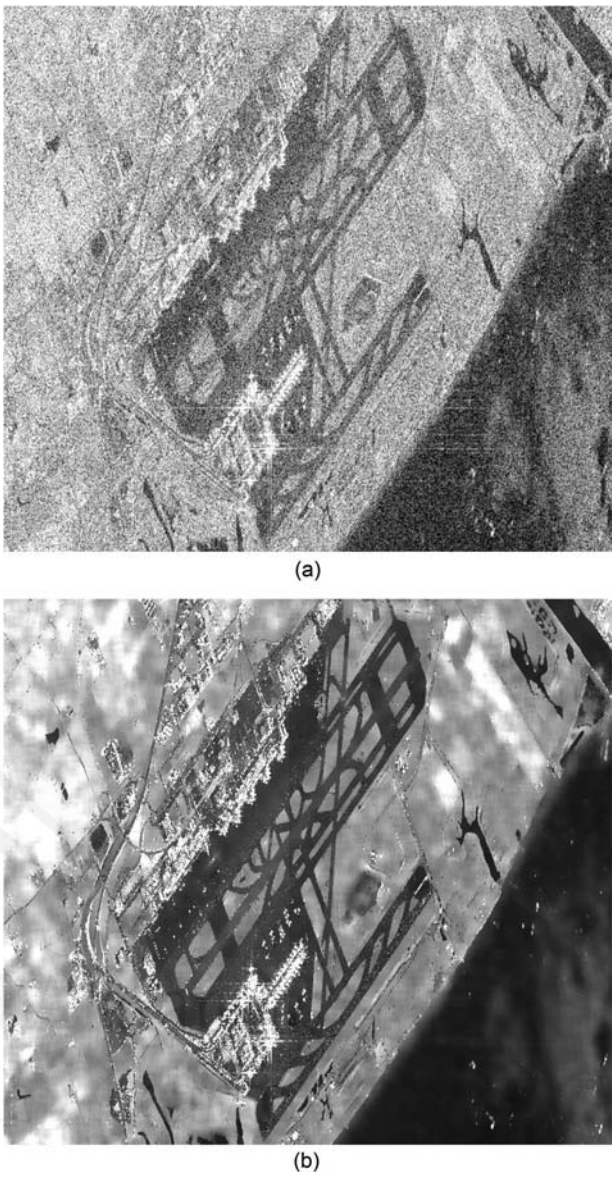

Fig. 2. Detail of an $HH + VV$ amplitude image, (a) original and (b) filtered. The filter parameters are 15×15 test window size, a $\log \Lambda$ threshold of -20, and $R = 20$.

carried out in [7] show good performance of the test for full-polarization data, with as few as 13 looks for the estimation of sample covariance matrices. Finally, another requirement for the right performance of this test is that $\mathbf{T}$ matrices have to be full rank. The rank of the $\mathbf{T}$ matrices implied in the test was evaluated for all the pixels in the available scenes by using a singular value decomposition approach, and all of them resulted to be full rank (rank 2 for dual-polarization data and rank 3 for full-polarization data), even for pixels selected as PSs.

One of the possible applications of this adaptive approach is amplitude despeckling: Once the PEWs for each pixel have been determined, we can despeckle amplitude SAR images just by averaging the amplitude values of the PHPs, ignoring those pixels with $L < R$. Fig. 2 shows a detail of a despeckled SAR amplitude image in comparison with the original amplitude image, where a value of $R = 20$ has been considered. We can observe how homogeneous areas have been filtered while

high-contrast details are preserved. Notice that filtering can also be extended in the temporal dimension, by just applying it to the time-averaged amplitude image.

Alternatively, for applications where phase information has to be preserved, such as PSI, the adaptive filter can be used to improve the estimation of the polarimetric and interferometric descriptors of DS while keeping PS unaffected.

In this work, we use the proposed filter as a preprocessing step, followed by a polarimetric optimization that will help us to select the best performing or most stable scattering mechanism along time, according to certain quality criterion. The polarimetric optimization step for both PS and DS is summarized in Section II-B.

Other studies on adaptive multitemporal speckle filtering strategies can be found in the literature. In [6], different parametric and nonparametric homogeneity tests exploiting single-polarization amplitude statistics are evaluated. One of such tests is the KS test, also used in the DespecKS filter [5]. In the context of multitemporal polarimetric data, an adaptive filter based on binary partition trees has been recently introduced in [14].

B. Polarimetric Optimization of PSI

The main objective of PSI polarimetric optimization is to maximize the quality and number of PSs and DSs selected as reliable *a priori*, by optimizing the parameters used as selection criterion. In [15]–[17], we proposed a general framework for PSI polarimetric optimization, starting from the concept of polarimetric (or vector) interferometry introduced in [9]: Let $\mathbf{k}$ be a target vector given by (1). In order to generate an interferogram, $\mathbf{k}$ can be projected onto a unitary complex column vector $\boldsymbol{\omega}$, resulting in $\mu = \boldsymbol{\omega}^\dagger \mathbf{k}$, where μ is a scalar complex scattering coefficient. As a scalar complex, μ is analogous to single-polarization data, so we can make use of any known PSI technique by applying it to μ. Hence, the proposed PSI optimization approach consists in finding, for each pixel, the projection vector $\boldsymbol{\omega}$ that optimizes the parameter considered as quality criterion when computed for μ.

To ease the search of the optimum projection vector (from now on referred to as the *optimum channel*), for fully polarimetric data, $\boldsymbol{\omega}$ can be parameterized as follows:

$$\boldsymbol{\omega} = \begin{bmatrix} \cos(\alpha) \\ \sin(\alpha)\cos(\beta)e^{j\delta} \\ \sin(\alpha)\sin(\beta)e^{j\psi} \end{bmatrix}, \qquad \begin{cases} 0 \leqslant \alpha \leqslant \pi/2 \\ 0 \leqslant \beta \leqslant \pi/2 \\ -\pi \leqslant \delta < \pi \\ -\pi \leqslant \psi < \pi \end{cases} \tag{9}$$

so the problem is reduced to finding four real parameters α, β, δ, and ψ whose range is finite and known and whose value is related to the geometric and electromagnetic features of the target [18]. In the following, we will refer to this simple optimization approach as exhaustive search polarimetric optimization (ESPO). Similarly, in the case of dual-polarization data, the two-component projection vector can be parameterized as

$$\boldsymbol{\omega} = \begin{bmatrix} \cos(\alpha) \\ \sin(\alpha)e^{j\psi} \end{bmatrix}, \qquad \begin{cases} 0 \leqslant \alpha \leqslant \pi/2 \\ -\pi \leqslant \psi < \pi \end{cases} \tag{10}$$

so the search is reduced to two real parameters α and ψ.

Since the reflectivity values for different polarimetric channels can be associated with different scattering mechanisms in the resolution cell located at different heights, hence with different phase centers, we constrain the optimum $\boldsymbol{\omega}$ obtained for each pixel to be the same along all the stack of images. In this way, we avoid introducing a varying phase term that will result in noisy deformation estimates. This constraint is usually found in the literature as equal scattering mechanisms [19], and it can be interpreted as selecting the most stable scattering mechanism over time, according to the chosen criterion of selection.

The most commonly used criterion of selection for PS is the amplitude dispersion index D_A [20]. For vector interferometry, D_A can be expressed as [15], [16]

$$D_A = \frac{\sigma_a}{\bar{a}} = \frac{1}{\overline{|\boldsymbol{\omega}^\dagger \mathbf{k}|}\sqrt{N-1}} \sqrt{\sum_{i=1}^{N} \left(|\boldsymbol{\omega}^\dagger \mathbf{k}_i| - \overline{|\boldsymbol{\omega}^\dagger \mathbf{k}|} \right)^2} \tag{11}$$

where N is the total number of images and the overline indicates an empirical mean value. Points with D_A below a given threshold will be selected as PS candidates, so in this case, our ESPO algorithm will search, for each pixel, the $\boldsymbol{\omega}$ that minimizes its D_A.

As for DSs, in order to evaluate their suitability for PSI, it is usual to rely on their average interferometric coherence magnitude $\overline{|\gamma|}$ as an indicator of the quality of the estimated interferometric phases [21], [22]. In the context of polarimetric interferometry, $\overline{|\gamma|}$ can be expressed as follows:

$$\overline{|\gamma|} = \frac{1}{K}\sum_{k=1}^{K} |\gamma_k|, \qquad \text{with } \gamma_k(\boldsymbol{\omega}) = \frac{\boldsymbol{\omega}^\dagger \boldsymbol{\Omega}_{ij} \boldsymbol{\omega}}{\sqrt{\boldsymbol{\omega}^\dagger \mathbf{T}_{ii} \boldsymbol{\omega}}\sqrt{\boldsymbol{\omega}^\dagger \mathbf{T}_{jj} \boldsymbol{\omega}}} \tag{12}$$

where the subscript k denotes the kth interferogram obtained by combining images i and j. Polarimetric coherency matrices $\mathbf{T}_{ii}$ and $\mathbf{T}_{jj}$ and polarimetric–interferometric cross-correlation matrix $\boldsymbol{\Omega}_{ij}$ are defined as in [9]

$$\mathbf{T}_{ii} = E\left[\mathbf{k}_i \mathbf{k}_i^\dagger\right] \qquad \mathbf{T}_{jj} = E\left[\mathbf{k}_j \mathbf{k}_j^\dagger\right] \qquad \boldsymbol{\Omega}_{ij} = E\left[\mathbf{k}_i \mathbf{k}_j^\dagger\right] \tag{13}$$

where $E[\cdot]$ is the expectation operator. These expectations cannot be computed in practice, so they will be replaced by their maximum-likelihood estimates, given by the empirical mean evaluated using L realizations of the target vectors. In our case, the L realizations will be given by the pixel's PEW determined by the proposed adaptive filter, as described in the previous section. In this way, we guarantee that we are averaging pixels with similar scattering properties, and consequently, the usual Gaussian assumption is more likely to hold. In this case, the ESPO algorithm will be applied on each DS to find the $\boldsymbol{\omega}$ that maximizes $\overline{|\gamma|}$. ESPO and alternative polarimetric optimization approaches are detailed in [17].

Notice that, at this point, we have different criteria of selection for PS and DS. Moreover, it is known that the estimator of γ_k has a bias depending on the number of looks [23], which, in our case, can vary for different DSs because of the adaptive filter. This is not practical if we want to process jointly PS and

DS, since both D_A and $\overline{|\gamma|}$ are not directly comparable. In the following section, we propose an alternative selection criterion that can be used for both PS and DS.

C. Joint Processing of PS and DS

In order to process jointly PS and DS, it is convenient to establish a common quality criterion for pixel selection, instead of using D_A for PS and $|\overline{\gamma}|$ for DS. The estimated phase standard deviation σ_ϕ has been chosen given its close relationship to both criteria. A pixel (either PS or DS) will be selected as stable if its expected σ_ϕ is lower than a chosen threshold, typically 15° (≈0.25 rad).

As demonstrated in [20], D_A is an estimator of σ_ϕ for high SNR values (generally, for $D_A < 0.25$), so for PS, we can directly consider $D_A \approx \sigma_\phi$ if we set the selection threshold appropriately. As for DS, σ_ϕ can be estimated from the pdf of the interferometric phase pdf(ϕ), which is related to the magnitude of the estimated interferometric coherence $|\gamma|$ and the number of independent looks used in the estimation L_e, as shown in [24]

$$\sigma_\phi = \sqrt{\int_\phi (\phi - \phi_0)^2 \text{pdf}(\phi) d\phi} \tag{14}$$

with

$$\text{pdf}(\phi) = \frac{\Gamma(L_e + 1/2)\left(1 - |\gamma|^2\right)^{L_e} \gamma \cos(\phi - \phi_0)}{2\sqrt{\pi}\Gamma(L_e)\left(1 - |\gamma|^2 \cos^2(\phi - \phi_0)\right)^{L_e + 1/2}} + \frac{\left(1 - |\gamma|^2\right)}{2\pi} F_1\left(L_e, 1; \frac{1}{2}; \gamma^2 \cos^2(\phi - \phi_0)\right)$$

where F_1 is a Gauss hypergeometric function and the expected phase ϕ_0 can be set to zero without loss of generality. Note that, when the number of independent samples is large ($L_e > 10$), σ_ϕ can be approximated as [25]

$$\sigma_\phi = \frac{1}{\sqrt{2N}} \frac{\sqrt{1 - |\gamma|^2}}{|\gamma|}. \tag{15}$$

Nevertheless, for a more accurate estimation of σ_ϕ in the case of low L_e values, we opted for precomputing a lookup table of $\sigma_\phi(|\gamma|, L_e)$ based on (14), which can be quickly queried at runtime.

For the sake of simplicity, σ_ϕ will be estimated taking into account the average interferometric coherence $|\overline{\gamma}|$, instead of the different values of $|\gamma_k|$ associated with each interferogram k.

From (14) and (15), it is extracted that, the lower the coherence magnitude or the number of looks, the higher the expected phase deviation. Notice that, in general, adjacent pixels in a SAR image will be correlated due to averaging, oversampling, or other processes, so L spatial samples will correspond, in general, to a smaller number of independent looks L_e. In order to account for this, we consider the following approximation:

$$L_e \approx \frac{L}{(\text{ovs\_range}) \cdot (\text{ovs\_azimuth})} \tag{16}$$

where ovs_range and ovs_azimuth are the oversampling factors in range and azimuth, respectively. Oversampling factors are obtained as the ratio between theoretical sensor resolution and pixel spacing of the final product. The values of these parameters for the data sets used in this work are shown in Section III.

In [5], an alternative methodology for joint processing of PS and DS is proposed, which relies on a phase triangulation algorithm (PTA) to obtain, for each DS, the N maximum-likelihood phase estimates from a set of K interferograms. In that case, the goodness of fit of the PTA is used as an extension, for DS, of the temporal coherence used in several PS-based PSI techniques.

III. Data Set

A set of 31 full-polarization single-look complex (SLC) images acquired by Radarsat-2 from January 2010 to February 2012 over the urban area of Barcelona (Spain), as well as a set of 41 dual-polarization (HH, VV) TerraSAR-X SLC images acquired over Murcia (Spain) from February 2009 to May 2010, has been used to test the proposed algorithms.

The Barcelona images have been acquired at a revisit time of 24 days using Radarsat-2 beam mode FQ9: a nominal incidence angle of 28° (near range) to 29.8° (far range). The nominal azimuth and slant-range resolutions are 7.6 and 5.2 m, whereas the nominal pixel dimensions are 5.1 and 4.7 m, respectively. Therefore, the resulting oversampling factors are 1.49 and 1.11 in azimuth and range. The processing has been applied over a section of the image of 1400×3600 pixels, where nonurban areas (mainly sea and mountains) have been masked out. A color composite formed by the Pauli average intensities is shown in Fig. 3. The different colors in the composite image provide an insight about the information content of polarimetry. The city is mostly located in the center of the image, showing different dominant channels at different parts. Buildings tend to behave as oriented dihedrals (due to facade-ground double reflections), whose polarimetric response depends highly on the orientation angle (OA) [26]. Dihedrals with an OA of 45° have a dominant cross-polarization response, whereas 22.5°-rotated dihedrals reflect equally all four polarimetric channels.

As for the Murcia images, they have been acquired at a revisit time of 11 days with a mean incidence angle of 37.8°. The azimuth and slant-range resolutions are 6.6 and 1.17 m, whereas the pixel dimensions are 2.44 and 0.91 m. The resulting oversampling factors are 2.7 and 1.28 in azimuth and range. The processing has been applied over a 2000×2000 portion of the images, centered in the urban area of Murcia. Fig. 4 shows a composite image of the selected scene.

IV. Results

In this section, we evaluate the performance of the proposed approach in terms of density of pixels selected and detail of the generated deformation velocity maps. We compare the results obtained by applying conventional PSI to an arbitrary single-polarization channel (HH), to the ESPO channel (optimized for minimum D_A), and to ESPO data preprocessed by the

Fig. 3. Composite RGB image of the area under study in Barcelona (Spain) formed by the average intensities. Channels: R $= HH - VV$, G $= 2HV$, and B $= HH + VV$.

Fig. 4. Composite RGB image of the area under study in Murcia (Spain) formed by the average intensities. Channels: R $= HH$, G $= VV$, and B $= HH - VV$.

TABLE I
MPs SELECTED FOR DIFFERENT CHANNELS, CONSIDERING A σ_ϕ THRESHOLD OF 0.25

TerraSAR-X	**PS**	**DS**	**MP (PS + DS)**	**MP/km^2**
HH	3.60%	-	3.60%	9968
DespecKS HH	3.60%	0.86%	4.45%	12321
ESPO (dual-pol)	8.63%	-	8.63%	23865
$\log\Lambda$ filter + ESPO	8.16%	5.10%	13.26%	36682
Radarsat 2	**PS**	**DS**	**MP (PS + DS)**	**MP/km^2**
HH	2.01%	-	4.07%	425
DespecKS HH	2.00%	13.88%	15.88%	3364
ESPO (full-pol)	13.83%	-	13.83%	2930
$\log\Lambda$ filter + ESPO	13.36%	5.26%	18.62%	3945

proposed adaptive filter. In this experiment, we have considered the same filter parameters for both Murcia and Barcelona scenes: a 15×15 PHP search window centered on the pixel, a $\log\Lambda$ threshold of -20, and $R = 20$ minimum number of PHP neighbors for the pixel to be treated as a DS. For comparison purposes, we have also included the results obtained by using the DespecKS filtering approach [5] on single-channel data (HH), with $R = 20$ and a KS two-sample test significance level of $\alpha = 0.01$ (1%).

In order to compare the densities of pixels selected by each approach, Table I summarizes the output of the selection stage. For the Barcelona scene, sea and mountains have been masked out. A distinction is made between pixels selected and processed as PSs and points processed as DSs, where applicable. The generic term "measure point" (MP) is given to the total sum of PS and DS, as in [5]. The selection results are given both in terms of percentage of pixels selected from the total pixels of the scene and in terms of MP/km^2. Note that, due to the different pixel spacing and incidence angle, an area of 1 km^2 corresponds to approximately $207 \times 102 = 21\,114$ pixels (azimuth $\times$ range) for the Radarsat-2 SLC images, whereas for TerraSAR-X, it corresponds to $\approx 410 \times 674 = 276\,340$ pixels, and hence, the MP/km^2 values differ in one order of magnitude between the two sensors. As appreciated in the table, the density of total selected pixels, or MPs, increases significantly with filtering.

In the case of the Murcia TerraSAR-X data, the DespecKS approach applied to only the HH channel does not render as good results as dual-polarization ESPO. DespecKS achieves an increase of MP of around $\times 1.24$ with respect to the unfiltered HH channel (4.45% versus 3.6%) due to the selection of new DSs. However, given the heterogeneity of the scene and the fine resolution of the sensor, this increase in the number of DSs is not so significant as the increase in PSs achieved by the ESPO approach, of around $\times 2.4$ with respect to HH (8.63% for ESPO compared to 3.60% for HH). Now, if we apply the proposed adaptive filter preprocessing to ESPO, the increase is even more

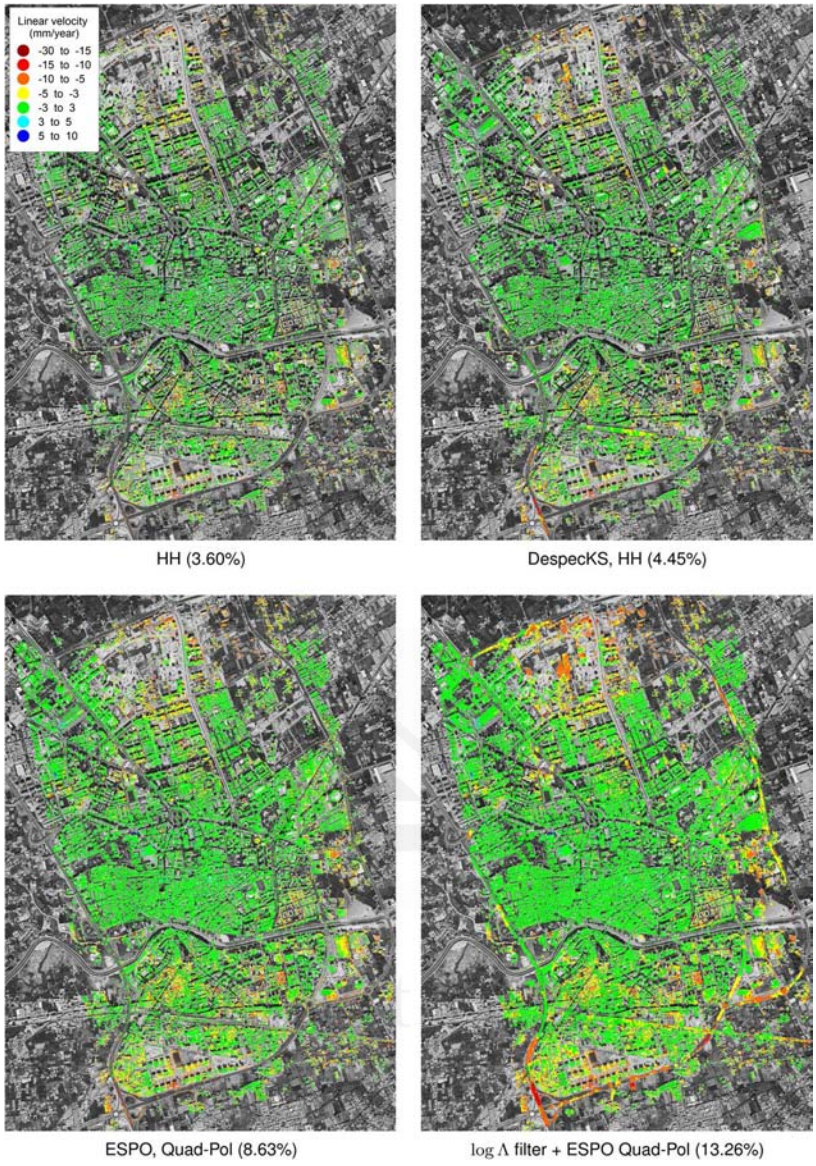

Fig. 5. Deformation velocity maps obtained for the Murcia scene using different configurations, and the percentage of selected pixels.

spectacular, obtaining 3.7 times more pixels (a total of 13.26%) than for HH.

For the Barcelona full-polarization Radarsat-2 set, the increase of pixel density of ESPO w.r.t. HH is around $\times 6.9$ (13.83% for ESPO compared to 2.01% for HH). However, in this case, the DespecKS filtering approach selects a larger percentage of pixels (15.88%), by revealing a significant number of DSs. Nevertheless, note that, in the ESPO approach, all selected pixels are treated as PSs, and hence, their resolution will not be degraded by filtering. DespecKS, on the other hand, is not contributing to the detection of new PSs, but DSs. Finally, if we apply the polarimetric filter proposed in this paper to ESPO, we obtain an increase of around $\times 9.27$ in comparison with HH (18.62% of pixels selected, from which 13.36% are to be treated as PSs). We noticed that, in this case, the proposed filtering approach is more sensitive to changes in the scene than DespecKS, for the parameters considered. Consequently, the average number of homogeneous neighbors per pixel is significantly smaller for the $\log \Lambda$ filter ($\approx$65 PHPs) than for the DespecKS approach ($\approx$102 SHPs), and thus, a larger number of pixels are treated as PSs.

Deformation velocity maps have been generated for both scenes using an implementation of the PSI technique described in [27], which has been adapted to process both PS and DS as described in this paper. Figs. 5 (Murcia) and 6 (Barcelona) show the obtained velocity maps for each channel, as well as the percentage of points selected.

We can clearly observe in both cases the significant improvement rendered by the inclusion of the proposed adaptive filter. The benefits are specially evident when we consider fully polarimetric data. We can see how man-made flat homogeneous structures, such as roads or airstrips, are now more likely to be selected in spite of their low backscattering power, since filtering allows us to reduce the deviation of phase estimates for DS. Additionally, since PS information is preserved (and enhanced by polarimetric optimization), we still achieve a good characterization of structures such as small buildings. Figs. 7 and 8 show an augmented view of representative areas

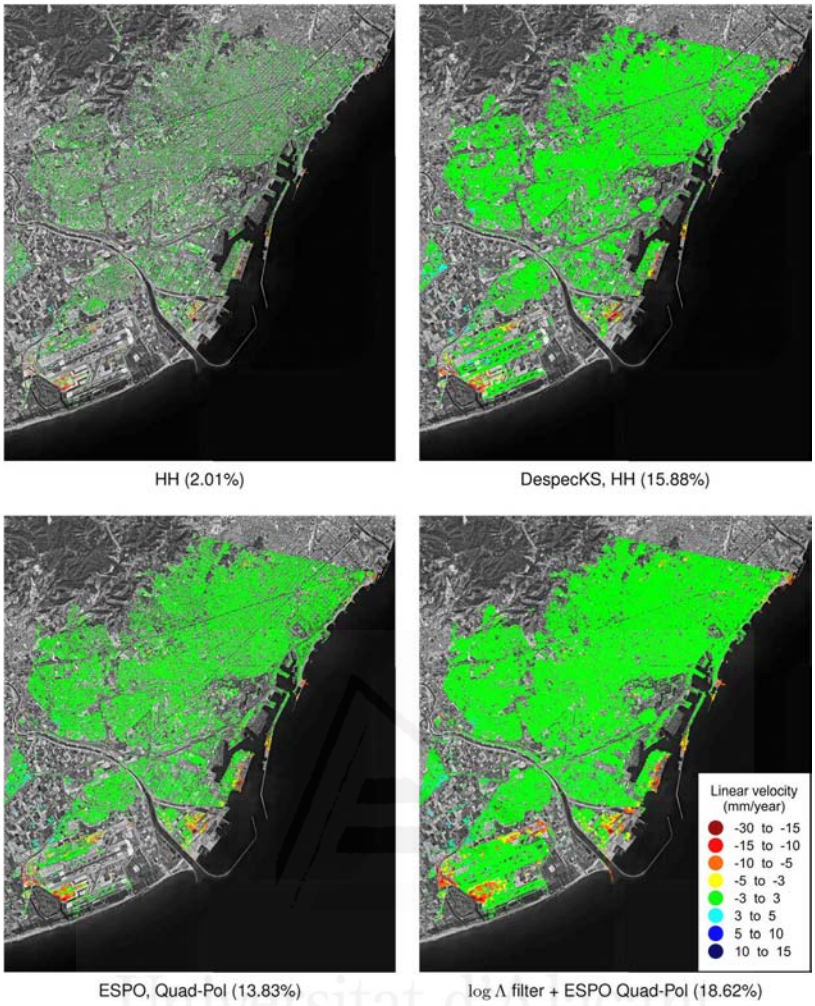

Fig. 6. Deformation velocity maps obtained for the Barcelona scene using different configurations, and the percentage of selected pixels.

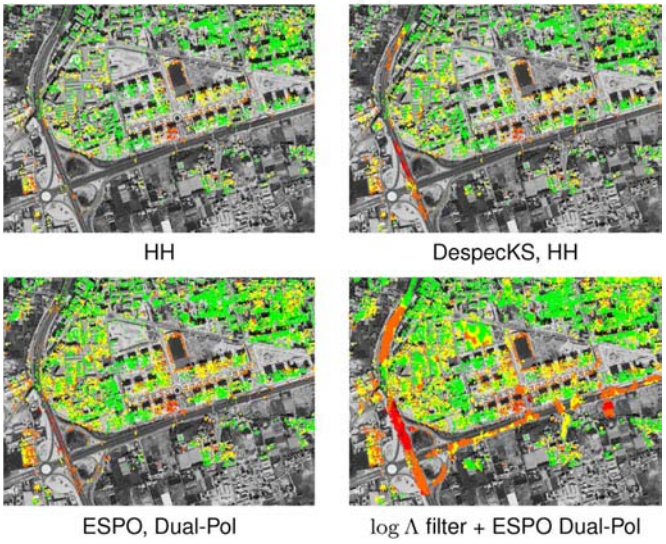

Fig. 7. Detail of deformation velocity maps; Murcia—highway bridge. The same color scale as in Fig. 5 is used.

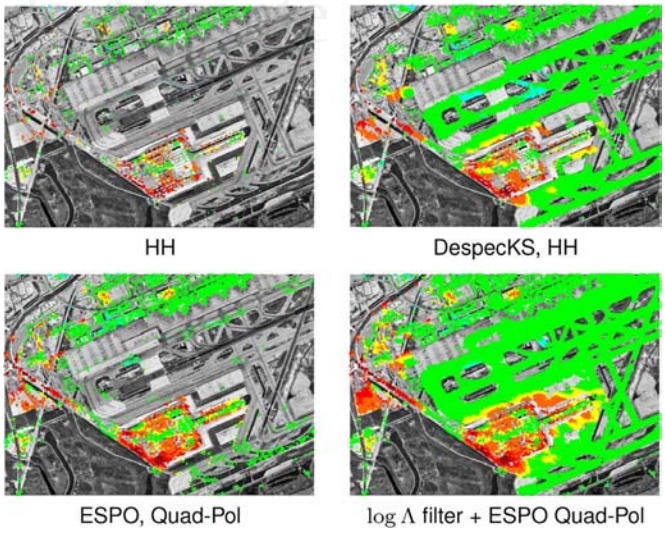

Fig. 8. Detail of deformation velocity maps; Barcelona—"El Prat" airport. The same color scale as in Fig. 6 is used.

containing the aforementioned structures, where we can appreciate the new deformation details revealed. Notice that pixel colored markers have been set to a size slightly larger than the resolution cell, in order to ease their visualization.

Validation of the obtained results is yet to be addressed, since we do not dispose of the required ground-truth data at the moment, although a qualitative comparison with other works on the Murcia area [28] and Barcelona area [29] using different

TABLE II
APPROXIMATE COMPUTATION TIMES FOR THE MAIN SPECKLE FILTERING STAGES

Murcia (TSX, dual-pol)	Homogeneity test	Polarimetric optimization	Interferogram filtering and pixels selection	Total
$\log \Lambda$ filter + ESPO	5 h	13 h	4.35 h	22.35 h
DespecKS HH	16 h	-	1.5 h	17.5 h
Barcelona (RDS2, full-pol)	Homogeneity test	Polarimetric optimization	Interferogram filtering and pixels selection	Total
$\log \Lambda$ filter + ESPO	6 h	17.2 h	6.7 h	29.9 h
DespecKS HH	17 h	-	2.5 h	19.5 h

sensors or data sets shows a good agreement with the presented results.

Obviously, the inclusion of the filtering step affects the total processing time. Computational cost mainly depends on the type of input data (higher for full polarization than for dual polarization), the number of images and generated interferograms, and the scene features. Generally, the larger the number of pixels treated as DSs, the higher the computational cost, since isolated scatterers do not require speckle filtering. D_A is calculated in a matter of seconds for the whole scene, while coherence estimation on DSs may take several hours. In addition to the increased computation time due to the filter, the additional cost related to the polarimetric optimization step has to be also accounted for. Moreover, due to the larger number of pixels selected for processing, final deformation velocity estimation stages will take longer to compute as well.

We have carried out our experiments on a Dell workstation equipped with a 12-core AMD Opteron processor (2.3 GHz) and 192 GB of RAM. The speckle filtering and polarimetric optimization approaches have been written in Interactive Data Language. The remaining of the PSI processing chain has been implemented in C language. As expected, the computational cost of the proposed approach is higher for the full-polarization Barcelona case of study, because of the higher dimensionality of data and density of DSs. Nevertheless, given the larger number of images and interferograms considered for the dual-polarization Murcia scene, the difference in total processing time is not so significant between the two cases. The approximate computation times for each stage are summarized in Table II. For comparison, we also included the computation times for our implementation of the DespecKS filtering approach. We can clearly observe that the polarimetric optimization stage is the most time-consuming step of the proposed technique. However, the likelihood ratio test is significantly more efficient (around three times faster) than the KS test used in DespecKS; hence, the total computing times are in a similar order of magnitude.

These times represent approximately 25% of the complete PSI processing time chain. Since computation time is generally not a critical factor for PSI (processing is carried out when a sufficient number of SAR images are available, which may take years depending on the satellite revisit time), the potential benefit in terms of map pixel density clearly justifies the increase of computational complexity.

V. CONCLUSION

In this paper, we have proposed a new spatial polarimetric adaptive speckle filter driven by temporal statistics, which is able to preserve PS information while filtering DS. Additionally, a simple methodology for joint processing of PS and DS has been presented, based on a common criterion of quality, the estimated phase standard deviation σ_ϕ.

The approach has been tested using dual-polarization TerraSAR-X data and full-polarization Radarsat-2 data. The PSI results show an important improvement in terms of area coverage (i.e., pixels with deformation information) compared with unfiltered data, either single-channel or polarimetrically optimized data. For filtered TerraSAR-X dual-polarization data, area coverage is increased by over $\times 1.5$ w.r.t. unfiltered ESPO data and $\times 3.7$ w.r.t. unfiltered single-polarization data. As for filtered Radarsat-2 full-polarization data, area coverage is increased by $\times 1.35$ w.r.t. unfiltered ESPO data and $\times 9.3$ w.r.t. unfiltered single-polarization data. The combination of adaptive filter and polarimetric optimization on full-polarization data is the configuration that provides the best results.

Validation of the presented results with ground-truth data is yet to be addressed. However, the increase of pixel density will generally contribute to the robustness of PSI approaches, adding redundancy and hence improving the accuracy of the phase estimates.

The performance and optimum configuration of the adaptive filter depend mainly on the features of the scene under study, as well as the sensor specifications. As a future research line, the performance of the filter on different scenarios as a function of configuration parameters will be carefully revised. Additionally, different tests for PHP discrimination will be studied and compared.

ACKNOWLEDGMENT

The TerraSAR-X images have been provided by the German Aerospace Center (DLR) in the framework of Project GEO0389 of the TerraSAR-X scientific program. Radarsat-2 Data and Products © MacDonald, Dettwiler and Associates (MDA) Ltd. (2010–2012)—All Rights Reserved. Radarsat is an official trademark of the Canadian Space Agency (CSA). The authors would like to thank Prof. J. Mallorquí (Universitat Politècnica de Catalunya) for providing access to the Radarsat-2 data, which were provided by MDA and CSA in the framework of Scientific Project SOAR-EU 6779. The orthophotographs have been provided by the Plan Nacional de Ortofotografía Aérea—©Instituto Geográfico Nacional de España.

REFERENCES

[1] J.-S. Lee, M. R. Grunes, and G. de Grandi, "Polarimetric SAR speckle filtering and its implication for classification," *IEEE Trans. Geosci. Remote Sens.*, vol. 37, no. 5, pp. 2363–2373, Sep. 1999.

[2] R. Touzi, "A review of speckle filtering in the context of estimation theory," *IEEE Trans. Geosci. Remote Sens.*, vol. 40, no. 11, pp. 2392–2404, Nov. 2002.

[3] A. Alonso-González, C. López-Martínez, and P. Salembier, "PolSAR speckle filtering and segmentation based on binary partition tree representation," presented at the Proc. POLinSAR, Frascati, Italy, Jan. 2011, Paper 695;25. [Online]. Available: http://www.polinsar2011.com
[4] G. Vasile, E. Trouvé, J.-S. Lee, and V. Buzuloui, "Intensity-driven adaptive-neighborhood technique for polarimetric and interferometric SAR parameters estimation," *IEEE Trans. Geosci. Remote Sens.*, vol. 44, no. 6, pp. 1609–1621, Jun. 2006.
[5] A. Ferretti, A. Fumagali, F. Novali, C. Prati, F. Rocca, and A. Rucci, "A new algorithm for processing interferometric data-stacks: SqueeSAR," *IEEE Trans. Geosci. Remote Sens.*, vol. 49, no. 9, pp. 3460–3470, Sep. 2011.
[6] A. Parizzi and R. Brcic, "Adaptive InSAR stack multilooking exploiting amplitude statistics: A comparison between different techniques and practical results," *IEEE Geosci. Remote Sens. Lett.*, vol. 8, no. 3, pp. 441–445, May 2011.
[7] K. Conradsen, A. Nielsen, J. Schou, and H. Skriver, "A test statistic in the complex Wishart distribution and its application to change detection in polarimetric SAR data," *IEEE Trans. Geosci. Remote Sens.*, vol. 41, no. 1, pp. 4–19, Jan. 2003.
[8] V. D. Navarro-Sanchez and J. M. Lopez-Sanchez, "Polarimetric stationarity criteria applied to the selection of pixel scatterers candidates," presented at the Proc. POLinSAR, Frascati, Italy, Jan. 2011, Paper 695;20. [Online]. Available: http://www.polinsar2011.com
[9] S. R. Cloude and K. P. Papathanassiou, "Polarimetric SAR interferometry," *IEEE Trans. Geosci. Remote Sens.*, vol. 36, no. 5, pp. 1551–1565, Sep. 1998.
[10] L. Ferro-Famil, A. Reigber, E. Pottier, and W. Boerner, "Scene characterization using subaperture polarimetric SAR data," *IEEE Trans. Geosci. Remote Sens.*, vol. 41, no. 10, pp. 2264–2276, Oct. 2003.
[11] D. E. Tyler, "Robustness and efficiency properties of scatter matrices," *Biometrika*, vol. 70, no. 2, pp. 411–420, Aug. 1983.
[12] T. W. Anderson, *An Introduction to Multivariate Statistical Analysis*. Hoboken, NJ, USA: Wiley, 2003.
[13] C. A. Coelho and F. J. Marques, "Near-exact distributions for the likelihood ratio test statistic to test equality of several variance–covariance matrices in elliptically contoured distributions," *Comput. Stat.*, vol. 27, no. 4, pp. 627–659, Dec. 2012.
[14] A. Alonso-González, C. Lopez-Martinez, and P. Salembier, "Temporal PolSAR image series exploitation with binary partition trees," in *Proc. IEEE IGARSS*, 2012, pp. 1493–1496.
[15] V. D. Navarro-Sanchez, J. M. Lopez-Sanchez, and F. Vicente-Guijalba, "A contribution of polarimetry to satellite differential SAR interferometry: Increasing the number of pixel candidates," *IEEE Geosci. Remote Sens. Lett.*, vol. 7, no. 2, pp. 276–280, Apr. 2010.
[16] V. D. Navarro-Sanchez and J. M. Lopez-Sanchez, "Improvement of persistent-scatterer interferometry performance by means of a polarimetric optimization," *IEEE Geosci. Remote Sens. Lett.*, vol. 9, no. 4, pp. 609–613, Jul. 2012.
[17] V. D. Navarro-Sanchez, J. M. Lopez-Sanchez, and L. Ferro-Famil, "Polarimetric approaches for persistent scatterers interferometry," *IEEE Trans. Geosci. Remote Sens.*, vol. 52, no. 4, Apr. 2014, to be published. [Online]. Available: http://ieeexplore.ieee.org
[18] S. R. Cloude, *Polarisation: Applications in Remote Sensing*. New York, NY, USA: Oxford Univ. Press, 2010.
[19] M. Neumann, L. Ferro-Famil, and A. Reigber, "Multibaseline polarimetric SAR interferometry coherence optimization," *IEEE Geosci. Remote Sens. Lett.*, vol. 5, no. 1, pp. 93–97, Jan. 2008.
[20] A. Ferretti, C. Prati, and F. Rocca, "Permanent scatterers in SAR interferometry," *IEEE Trans. Geosci. Remote Sens.*, vol. 39, no. 1, pp. 8–20, Jan. 2001.
[21] P. Berardino, G. Fornaro, R. Lanari, and E. Sansosti, "A new algorithm for surface deformation monitoring based on small baseline differential SAR interferograms," *IEEE Trans. Geosci. Remote Sens.*, vol. 40, no. 11, pp. 2375–2383, Nov. 2002.
[22] O. Mora, J. J. Mallorquí, and A. Broquetas, "Linear and nonlinear terrain deformation maps from a reduced set of interferometric SAR images," *IEEE Trans. Geosci. Remote Sens.*, vol. 41, no. 10, pp. 2243–2253, Oct. 2003.
[23] R. Touzi, A. Lopes, J. Bruniquel, and W. P. Vachon, "Coherence estimation for SAR imagery," *IEEE Trans. Geosci. Remote Sens.*, vol. 37, no. 1, pp. 135–149, Jan. 1999.
[24] J.-S. Lee, K. W. Hoppel, S. A. Mango, and A. R. Miller, "Intensity and phase statistics of multilook polarimetric and interferometric SAR imagery," *IEEE Trans. Geosci. Remote Sens.*, vol. 32, no. 5, pp. 1017–1028, Sep. 1994.
[25] J. O. Hagberg, L. M. H. Ulander, and J. Askne, "Repeat-pass SAR interferometry over forested terrain," *IEEE Trans. Geosci. Remote Sens.*, vol. 33, no. 2, pp. 331–340, Mar. 1995.
[26] Z. Shan, H. Zhang, C. Wang, W. An, T. Wu, and X. Chen, "Four-component model-based decomposition of polarimetric SAR data for special ground objects," *IEEE Geosci. Remote Sens. Lett.*, vol. 9, no. 5, pp. 989–993, Sep. 2012.
[27] P. Blanco-Sanchez, J. Mallorqui, S. Duque, and D. Monells, "The coherent pixels technique (CPT): An advanced DInSAR technique for nonlinear deformation monitoring," *Pure Appl. Geophys.*, vol. 165, no. 6, pp. 1167–1193, Jun. 2008.
[28] G. Herrera, R. Tomás, D. Monells, G. Centolanza, J. J. Majorquí, F. Vicente, V. D. Navarro, J. M. Lopez-Sanchez, M. Sanabria, M. Cano, and J. Mulas, "Analysis of subsidence using TerraSAR-X data: Murcia case study," *Eng. Geol.*, vol. 116, no. 3/4, pp. 284–295, Nov. 2010.
[29] O. Monserrat, M. Crossetto, M. Cuevas, and B. Crippa, "The thermal expansion component of persistent scatterer interferometry observations," *IEEE Geosci. Remote Sens. Lett.*, vol. 8, no. 5, pp. 864–868, Sep. 2011.

Victor D. Navarro-Sanchez (S'09) was born in Caravaca de la Cruz, Spain, in 1982. He received the Ingeniero Técnico degree in telecommunication engineering from the University of Alicante, Alicante, Spain, in 2004, the Ingeniero degree in telecommunication engineering from the Miguel Hernández University of Elche, Elche, Spain, in 2009, and the Official Master degree in computer technologies from the University of Alicante in 2010.

Since 2009, he has been a Predoctoral Grant Holder with the Signals, Systems and Telecommunication Group, Escuela Politécnica Superior, University of Alicante. His research interests include polarimetric and interferometric synthetic aperture radar methods for urban and natural environment monitoring and classification.

Juan M. Lopez-Sanchez (S'94–M'00–SM'05) was born in Alicante, Spain, in 1972. He received the Ingeniero and Doctor Ingeniero degrees in telecommunication engineering from the Polytechnic University of Valencia (UPV), Valencia, Spain, in 1996 and 2000, respectively.

From 1998 to 1999, he was a Predoctoral Grant Holder with the Space Applications Institute, Joint Research Centre, European Commission, Ispra, Italy. Since 2000, he has been leading the Signals, Systems and Telecommunication Group, Escuela Politécnica Superior, University of Alicante, Alicante, where he has been a Full Professor since November 2011. He has coauthored more than 40 papers in refereed journals and more than 80 papers and presentations in international conferences and symposia. His main research interests include microwave remote sensing for inversion of biophysical parameters, polarimetric and interferometric techniques, synthetic aperture radar imaging algorithms, and analytical and numerical models for multiple scattering problems.

Dr. Lopez-Sanchez was the recipient of the Indra award for the best Ph.D. thesis about radar in Spain in 2001. He was the Chair of the Spanish Chapter of the IEEE Geoscience and Remote Sensing Society from 2006 to 2012.

Complete list of contributions

Papers in Journals

V. D. Navarro-Sánchez and J. M. López-Sánchez. Polarimetric Approaches for Persistent Scatterers Interferometry. *IEEE Trans. on Geosci. and Remote Sensing*, 52(8), pp. 4548-4557, August 2014

V. D. Navarro-Sánchez, J. M. López-Sánchez and L. Ferro-Famil. Polarimetric Approaches for Persistent Scatterers Interferometry. *IEEE Trans. on Geosci. and Remote Sensing*, 52(3), pp. 1667-1676, March 2014

V. D. Navarro-Sánchez and J. M. López-Sánchez. Improvement of Persistent-Scatterer Interferometry Performance by Means of a Polarimetric Optimization. *IEEE Geosci. and Remote Sensing Lett.*, 9(4), pp. 609-613, July 2012.

G. Herrera, R Tomás, D. Monells, G. Centolanza, J. J. Mallorquí, F. Vicente, V. D. Navarro, J. M López-Sánchez, M. Cano, J. Mulas, M. Sanabria. Analysis of subsidence using TerraSAR-X data: Murcia case study. *Engineering Geology*, 116 (3-4), pp. 284-295, September 2010

V. D. Navarro-Sánchez, J. M. López-Sánchez and F. Vicente-Guijalba. A contribution of Polarimetry to Satellite Differential SAR Interferometry: Increasing the Number of Pixel Candidates. *IEEE Geosci. and Remote Sensing Lett.*, 7(2), pp. 276-280, April 2010.

Papers in Conferences

V. D. Navarro-Sánchez and J. M. López-Sánchez. Exploitation of TerraSAR-X Dual-Pol Time Series for Adaptive Speckle Filtering and its Application to Persistent Scatterers Interferometry. In *Proc. of 5th TerraSAR-X Science Team Meeting*, DLR, Oberpfaffenhofen, Germany, June 2013.

V. D. Navarro-Sánchez and J. M. López-Sánchez. Polarimetric adaptive speckle filtering driven by temporal statistics for PSI applications. In *Proc. of PolInSAR'13*, Frascati, Italy, January 2013.

V. D. Navarro-Sánchez and J. M. López-Sánchez. Subsidence Monitoring Using Polarimetric Persistent Scatterers Interferometry. In *Proc. of IGARSS'11*, Vancouver, Canada, July 2011.

V. D. Navarro-Sánchez and J. M. López-Sánchez. On the Selection Criteria for Pixel Candidates in PSI: Potentials of Polarimetry. In *Proc. of 4th TerraSAR-X Science Team Meeting*, DLR, Oberpfaffenhofen, Germany, February 2011.

V. D. Navarro-Sánchez and J. M. López-Sánchez. Polarimetric Stationarity Criteria Applied to the Selection of Persistent Scatterer Candidates. In *Proc. of PolInSAR'11*, Frascati, Italy, January 2011.

V. D. Navarro-Sánchez, J. Arnal and J. M. López-Sánchez. Paralelización de etapas de procesado de señal en interferometría diferencial SAR. In *Proc. of WoTI'10*, Alicante, Spain, September 2010.

D. Monells, G. Centolanza, J. J. Mallorquí, S. Duque, P. López-Dekker, R. Tómas, G. Herrera, J. M. López-Sánchez, F. Vicente, V. D.Navarro-Sánchez and J. Mulas. Application of Terrasar-X data to the monitoring of urban subsidence in the city of Murcia. In *Proc. of IGARSS'10*, Honolulu, USA, July 2010.

V. D. Navarro-Sánchez and J. M. López-Sánchez. Polarimetric Enhancement of Pixel Candidates Selection in Persistent Scatterers Interferometry. In *Proc. of. EUSAR'10*, Aachen, Germany, July 2010.

V. D. Navarro-Sánchez, J. M. López-Sánchez and F. Vicente-Guijalba. Improving the Selection of Pixel Candidates in Differential SAR Interferometry by a Polarimetric Optimization. In *Proc. of FRINGE'09*, Frascati, Italy, November 2009.

Bibliography

P. Berardino, G. Fornaro, R. Lanari, and E. Sansosti. A New Algorithm for Surface Deformation Monitoring Based on Small Baseline Differential SAR Interferograms. *IEEE Trans. Geosci. Remote Sensing*, 40(11):2375–2383, November 2002.

Walter G. Carrara, Ron S. Goodman, and Ronald M. Majewski. *Spotlight Synthetic Aperture Radar: Signal Processing Algorithms*. Artech House Publishers, 1995.

S. R. Cloude. *Polarisation: Applications in Remote Sensing*. Oxford University Press, 2010.

S. R. Cloude and K. P. Papathanassiou. Polarimetric SAR Interferometry. *IEEE Trans. Geosci. Remote Sensing*, 36(5):1551–1565, 1998.

P. Dheenathayalan and R. Hanssen. Target Characterization and Interpretation of Deformation Using Persistent Scatterer Interferometry and Polarimetry. In *Proc. of POLinSAR'11*, Frascati, Italy, January 2011.

A. Ferretti, C. Prati, and F. Rocca. Nonlinear Subsidence Rate Estimation Using Permanent Scatterers in Differential SAR Interferometry. *IEEE Trans. Geosci. Remote Sensing*, 38 (5):2202 – 2212, September 2000.

A. Ferretti, C. Prati, and F. Rocca. Permanent scatterers in SAR interferometry. *IEEE Trans. Geosci. Remote Sensing*, 39(1):8–20, January 2001.

Ramon F. Hansen. *Radar Interferometry. Data Interpretation and Error Analysis.* Kluwer Academic Publishers, 2001.

G. Herrera, R. Tomás, D. Monells, G. Centolanza, J. J. Majorquí, F. Vicente, V. D. Navarro, J. M. Lopez-Sanchez, M. Sanabria, M. Cano, and J. Mulas. Analysis of subsidence using TerraSAR-X data: Murcia case study. *Engineering Geology*, 116:284–295, September 2010.

Bert M. Kampes. *Radar Interferometry. Persistent Scatterer Technique*. Springer, 2006.

J.-S. Lee and E. Pottier. *Polarimetric Radar Imaging: From Basics to Applications*. CRC Press. Taylor & Francis Group, 2009.

O. Monserrat, M. Crossetto, M. Cuevas, and B. Crippa. The Thermal Expansion Component of Persistent Scatterer Interferometry Observations. *IEEE Geosci. Remote Sensing Lett.*, 8(5):864–868, September 2011.

Oscar Mora. *Advanced Differential Interferometric SAR techniques for detection of terrain and building displacements*. PhD thesis, Universitat Politècnica de Catalunya, 2004.

V. D. Navarro-Sanchez and J. M. Lopez-Sanchez. Polarimetric Stationarity Criteria Applied to the Selection of Pixel Scatterers Candidates. In *Proc. of POLinSAR'11*, Frascati, Italy, January 2011.

V. D. Navarro-Sanchez and J. M. Lopez-Sanchez. Improvement of Persistent-Scatterer Interferometry Performance by Means of a Polarimetric Optimization. *IEEE Trans. Geosci. Remote Sensing*, 9(4):609 –613, July 2012.

V. D. Navarro-Sanchez and J. M. Lopez-Sanchez. Spatial Adaptive Speckle Filtering Driven by Temporal Polarimetric Statistics and Its Application to PSI. *IEEE Geosci. Remote Sensing Lett.*, 52(8):4548–4557, August 2014.

V. D. Navarro-Sanchez, J. M. Lopez-Sanchez, and F. Vicente-Guijalba. A Contribution of Polarimetry to Satellite Differential SAR Interferometry: Increasing the Number of Pixel Candidates. *IEEE Geosci. Remote Sensing Lett.*, 7(2):276 –280, April 2010.

V. D. Navarro-Sanchez, J. M. Lopez-Sanchez, and L. Ferro-Famil. Polarimetric approaches for persistent scatterers interferometry. *IEEE Trans. Geosci. Remote Sensing*, 52(3):1667–1676, March 2014.

C. J. Oliver and S. Quegan. *Understanding Synthetic Aperture Images*. Remote Sensing Library. Artech House, Incorporated, 1998.

P. Perissin and A. Ferretti. Urban-Target Recognition by Means of Repeated Spaceborne SAR Images. *IEEE Trans. Geosci. Remote Sensing*, 45(12):4043–4058, December 2009.

L. Pipia, X. Fabregas, A. Aguasca, C. López-Martínez, S. Duque, J. J. Mallorquí, and J. Marturià. Polarimetric Differential SAR Interferometry: First Results With Ground-Based Measurements. *IEEE Geosci. Remote Sensing Lett.*, 6(1):167–171, January 2009a.

L. Pipia, X. Fabregas, A. Aguasca, C. López-Martínez, and J. J. Mallorquí. Polarimetric Coherence Optimization for Interferometric Differential Applications. In *Proceedings of IGARSS'09*, Cape Town, South Africa, July 2009b.